UNIVERSITÀ DEGLI STUDI DI PADOVA

DIPARTIMENTO DI SCIENZE CHIMICHE

CORSO DI LAUREA MAGISTRALE IN CHIMICA

TESI DI LAUREA MAGISTRALE

The Mechanism of Electrochemically-Mediated Photoredox Catalysis with Organic Superoxidants

Relatore: Prof. Marco Fantin

Controrelatore: Prof.ssa Carla Marega

Laureando: Edoardo Bigolin

Matricola: 2090999

ANNO ACCADEMICO: 2023/2024

Table of contents

1. Introduction

1.1 Electro photocatalysis

1.1.1 Electrocatalysis

Electrocatalysis has a long history as a powerful tool in organic synthesis, allowing for efficient and selective transformations. The first applications in the early 1800s[1] marked the beginning of recognizing electrocatalysis as a promising strategy for radical-based reactions, paving the way for electrochemical organic synthesis. A basic electrocatalysis setup consists of a power source connected to two electrodes immersed in a solution, creating a closed loop for electron flow. Oxidation occurs at the anode, while reduction takes place at the cathode. For charge conservation, the rate of interfacial electron transfer (ET) at both the anode and the cathode must be equal. Since many solvents have low conductivity, a supporting electrolyte is typically added to reduce the solution's resistance, facilitating current flow between the electrodes. In many organic electrochemical transformations, only one of the two electrodes—the working electrode (WE)—produces a useful product. Meanwhile, a nonproductive reaction occurs at the counter electrode (CE), often involving hydrogen evolution or the oxidation of a sacrificial amine or the anode itself[2].

Mechanistically, electrocatalysis drives electron transfer at the electrodes or through the electrolyte, triggering oxidation or reduction reactions. These reactions can be categorized into direct and indirect electrolysis (Scheme 1). In direct electrolysis, the substrate gains or loses electrons directly at the electrode, creating reactive intermediates that undergo further reactions. Conversely, indirect electrolysis involves a redox mediator (electrocatalyst EC). This species is more readily oxidized or reduced than the substrate and serves as an electron-transfer shuttle, bridging the heterogeneous electrode surface and the dissolved substrates in solution. This approach often enhances reaction efficiency and chemoselectivity by preventing undesirable side reactions[3].

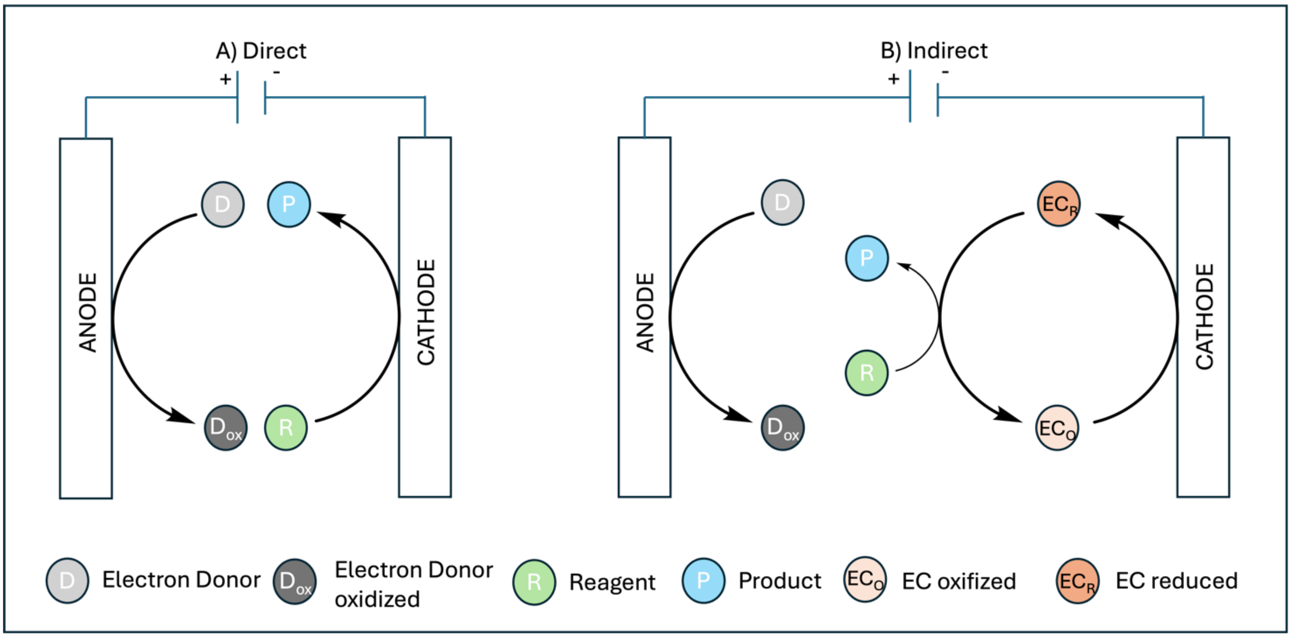

Scheme 1. Schematic representation of a direct (A) and indirect (B) reduction process.

Electrocatalytic methods offer a range of appealing advantages over traditional organic synthesis. By using electrical energy to drive chemical reductions, they enable reactions to occur under milder conditions, conserve energy, minimize environmental impact, and align with the principles of green chemistry[4]. Controlling the electrode potential allows precise management of reaction progress, enhancing selectivity and preserving functional groups. Moreover, the use of electrochemical techniques in the reaction medium, such as cyclic voltammetry (CV), represents an excellent analytical tool for gaining insight into the reaction mechanism and its reversibility[5].

However, electrosynthetic methods face some challenges. For example, this technique is limited by the electrochemical stability window imposed by the solvent and the electrolyte[6–8]. In direct electrolysis, the heterogeneous nature of the reaction and the high concentration of reactive species at the electrode can cause reactive radicals to undergo side reactions before diffusing away from the electrode surface, potentially lowering yields. Additionally, the electrode surface can become contaminated by intermediates from starting material decomposition, leading to passivation. Furthermore, contaminants from decomposing reactants can accumulate on the electrode, further contributing to passivation. In indirect electrolysis, the reactions proceed away from the electrode surface. However, the thermodynamic energy of mediators is limited by their redox potential. In complex reactions, high potentials may be needed to generate intermediates, but extreme potentials can compromise reaction control and decrease selectivity[9].

1.1.2 Photocatalysis

The process of utilizing a photoexcited photocatalyst (PC) to initiate redox reactivity is termed photocatalysis. Photocatalytic redox reactions first captured chemists' interest in the 1970s, although progress in the field was initially slow and received limited attention for many years[10]. In the early 2000s, however, a series of studies reignited interest among organic synthetic chemists[11–13], leading to significant and growing focus on photocatalysis[13–17]. Photocatalysis often employs catalytic amounts of photoredox catalysts instead of stoichiometric quantities of chemical oxidants or reductants, enhancing resource efficiency. Moreover, these reactions typically proceed under milder conditions, require simple equipment, and are straightforward to conduct[9]. An additional benefit is the ability to selectively photoexcite the catalyst, when it is appropriately selected, without interfering with other species, thus minimizing unwanted reactivity or instability.

With the increasing focus on photocatalytic reactions, considerable effort has been directed toward understanding the mechanisms underlying photocatalysis. Many organic compounds exhibit limited ability to directly absorb visible light and therefore rely on photocatalysts to capture light energy. This enables the photocatalyst to reach high oxidation or reduction potentials, thereby facilitating the conversion of light energy into chemical energy. In photoredox-catalyzed reactions, the photocatalyst functions as either an oxidant or a reductant within the chemical process.

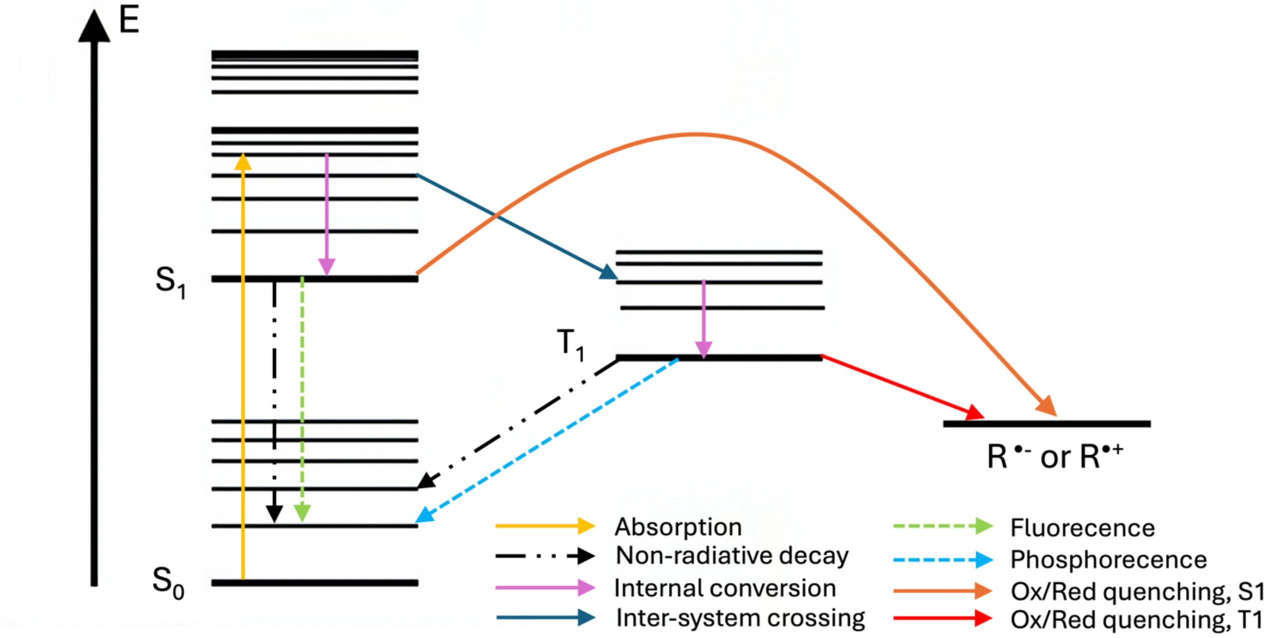

Scheme 2. Jablonski diagram of the photophysical processes after absorption of a photon by a generic molecule. (S_0) singlet ground state, (S_1) singlet excited state, (T_1) triplet ground state, ($R^{\bullet-}/R^{\bullet+}$) radical anion/cation state

Upon absorbing visible light, the photocatalyst is promoted from its ground state to an excited state, enhancing its oxidative and reductive capabilities[18]. The energy gained greatly depends on the accessed electronic state and the stability of the molecules in such state (Scheme 2).

In photoredox catalysis, a photocatalyst (PC) absorbs a photon of the appropriate wavelength, reaching an excited state (PC*), as depicted in Scheme 2. From this excited state, PC* can proceed through various pathways, including those involved in photoinduced electron transfer (PET). During PET, the excited state undergoes quenching via oxidative or reductive processes from either the singlet (S1) or triplet (T1) states. In these quenching pathways, PC* engages in single electron transfer (SET) with an electron acceptor (A) or donor (D), resulting in a highly reactive intermediate, often a radical species (indicated by the red and orange arrows in Scheme 2). Throughout PET, the excited photocatalyst can return to its ground state via oxidative or reductive quenching mechanisms (Scheme 3).

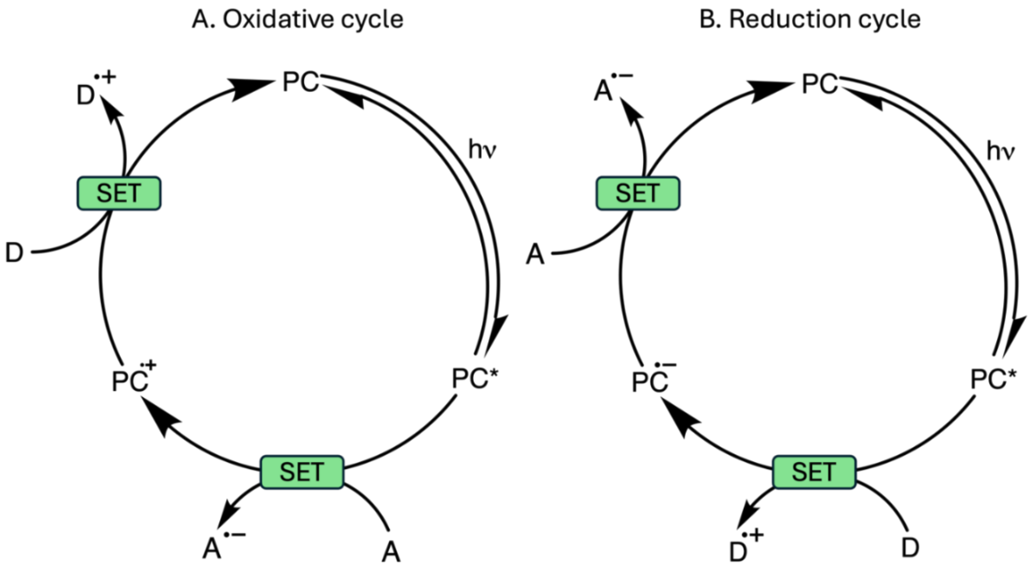

Scheme 3. Photocatalytic cycle for oxidation (A) and reduction (B) processes.

In addition to the SET pathway, the excited photocatalyst can engage in energy transfer (EnT) with the substrate, directly activating it into a reactive intermediate; however, this will not be discussed further as it does not involve an SET mechanism. As a synthetic strategy that has advanced significantly over the past decade, photocatalysis enables efficient and selective formation of various bonds, including C–C, C–N, C–O, and C–P bonds, due to its unique mechanistic pathways.

Nonetheless, the scope of photoredox catalysis is limited by both the redox potential of the substrate and the excitation potential of the photocatalyst. Additional constraints arise from the fact that the thermodynamic driving force of a photocatalyst (PC) is restricted by the energy of visible photons (1.8-3.1 eV; 400-700 nm), which may not be sufficient to overcome the oxidation potential of certain substrates. There is also an energy loss of the initial photon energy due to the dissipation of excitation energy from the PC* before its energy is transferred to the substrate. This is due to combined losses from internal conversion (IC) and intersystem crossing (ISC). Moreover, oxidation or reduction of the photocatalyst itself can present challenges. Increasing photon energy is often unfeasible, as many organic substrates absorb UV light directly, which can induce photodamage, undesired side reactions, and photobleaching of the photocatalyst. To drive an overall oxidation or reduction reaction, a terminal oxidant or reductant is generally required as a sacrificial agent to complete the catalytic cycle. These sacrificial agents, however, may interact with catalysts, substrates, reagents, or active intermediates, potentially generating undesirable byproducts. Such side reactions can diminish the efficiency of the primary reaction, hinder its progression, complicate the reaction system, and the use of sacrificial reagents can become economically unfavourable[7,8].

1.1.3 Combination of Electrochemistry and Photochemistry

Electrochemistry and photochemistry have been combined with unique advantages via three different strategies that are here briefly discussed. The combination of the two techniques is often defined with the generic term *photoelectrochemistry*.

- *iPEC*

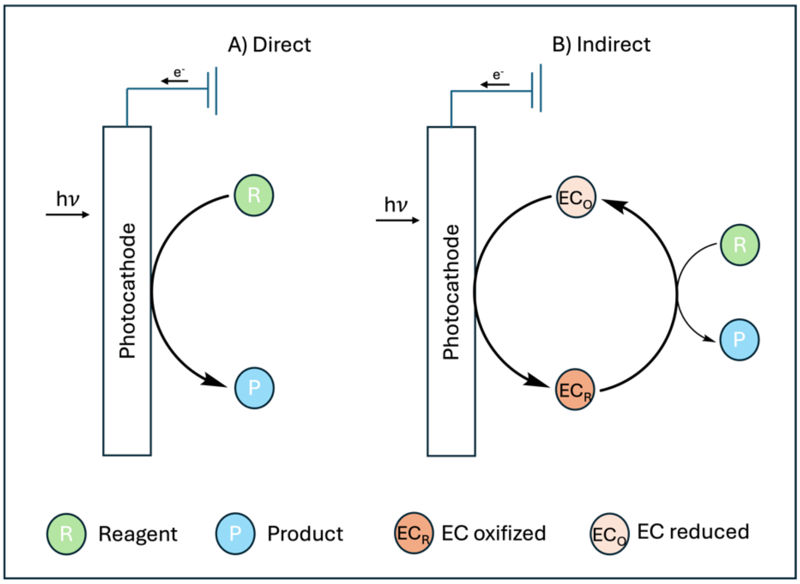

Scheme 4. Schematic representation of (A) direct and (B) indirect reduction iPEC,

Interfacial photoelectrochemistry (iPEC), is the most widely practiced form of photo-electrochemistry. In iPEC (Scheme 4), a semiconductor-based photoelectrode (photoanode or photocathode) is utilized to catalyze a heterogeneous reaction on its surface, assisted by a potential bias. This potential enhances electron-hole (e^-/h^+) separation, crucial for efficient charge transfer (that is manifested as minimal recombination) to the surface where oxidation or reduction of a substrate can occur. This charge separation is generally achieved by a photoresponsive semiconductor, often deposited on a photoactive material, whose band gap aligns with the energy of incoming photons[7,19]. In photoanodes, the applied bias and light together promote an electron from the valence band to the conduction band, leaving behind a hole to drive oxidation reactions. To enhance efficiency, semiconductor electrodes must fulfill dual roles: absorbing light to generate separated charges and promoting reactivity with the substrate at the surface. Consequently, junctions between two semiconductors are frequently employed to improve charge transfer[7,18]. iPEC processes can be classified as either direct or indirect. In direct processes, the reaction takes place on the photoelectrode’s surface, while in indirect processes, a mediator promotes the reaction and is subsequently regenerated at the photoelectrode.

The concept of coupling light with an applied potential in electrochemistry dates back to the 1970s. One of the earliest examples was demonstrated by Fujishima et al.[20], who explored water splitting using a TiO_2 photoelectrode under UV light, setting a foundation for ongoing advancements in photovoltaics and renewable energy applications.

- *e-PRC*

Electrochemically-mediated photoredox catalysis (e-PRC), which is the topic of this thesis, merges photochemical and electrochemical events within the same reaction pathway, enhancing the energy balance of the photo-redox cycle. In this approach, both an electron (or hole) and a photon contribute energy to the catalyst, creating super-oxidants or super-reductants that can perform highly demanding transformations beyond the typical redox windows of standalone photoredox catalysis or synthetic electrochemistry.

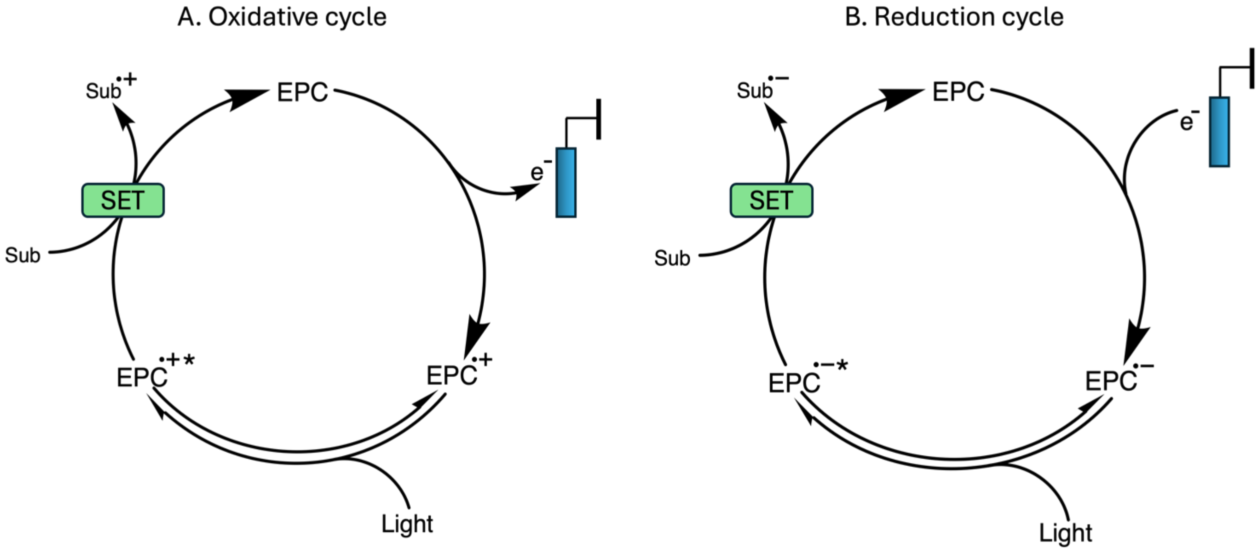

Scheme 5. General mechanism for electrophotocatalysis in the case of (A) oxidation and (B) reduction.

In a typical oxidative e-PRC cycle (Scheme 5A), the process begins with the electrochemical activation of a photocatalyst, termed EPC because of its dual nature of electro-photocatalyst. Oxidation of EPC generates an open-shell intermediate such as a radical cation (EPC$^{\cdot+}$). This radical then absorbs a photon, reaching an excited state (*EPC$^{\bullet+}$) with enhanced redox potential due to inversion of its singularly occupied molecular orbital (SOMO) and highest occupied molecular orbital (HOMO)[8,21] (Scheme 6). The same concept of e-PRC can be extended to reduction reactions (Scheme 5B). The benefits of e-PRC combine the high energy of the photoreactive intermediate with the absence of sacrificial electron donors or acceptors: electrical current is used instead to regenerate the starting state of the catalyst. A pivotal factor in e-PRC's adaptability is the range of tunable parameters, including the applied potential, irradiation wavelength, and catalyst structure, allowing fine control over reaction pathways and selectivity[6]. The development of diverse e-PRC catalysts has unlocked access to ultrahigh-energy redox processes under mild conditions, providing novel opportunities in organic synthesis and complex molecule functionalization.

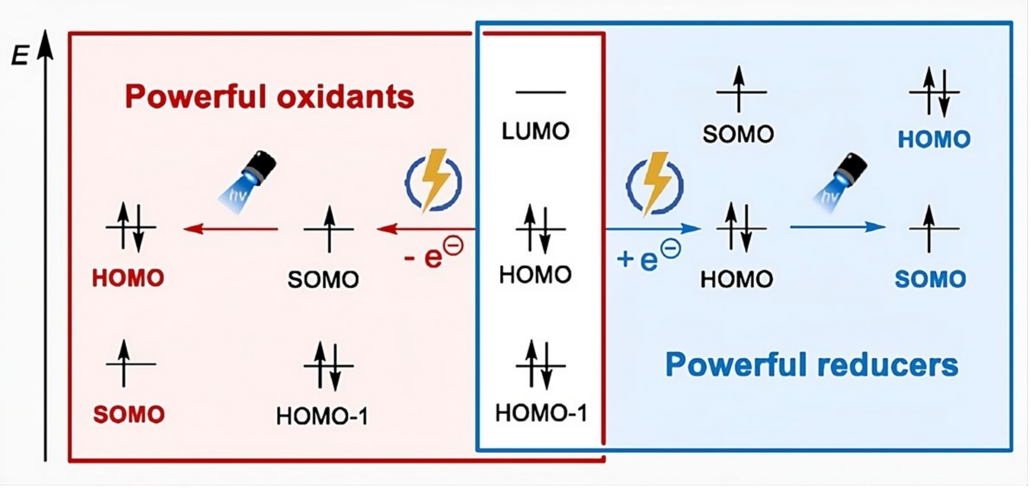

Scheme 6. Representation of the molecular orbitals of the electrophotocatalyst (EPC) taken from[8]).

These photoexcited open-shell species display exceptional redox properties, facilitating reactions like reductive carbon-halogen bond cleavage [6,7,18] or oxidative C-H amination[22–24]. This versatility has made e-PRC invaluable for reactions that require extreme potentials while maintaining mild conditions typically achievable with a modest applied potential (around +1.5 V to -1.5 V vs. SCE) and visible light[6,8,18,21].

Historically, the concept of e-PRC emerged in 1979, when Moutet and Reverdy demonstrated the oxidation of 1,1-diphenylethylene using a photoexcited phenothiazine radical cation under mercury lamp irradiation[25]. They laid the groundwork for e-PRC, showing that this approach could access redox states that are not feasible in isolated photoredox or electrochemical processes alone. Later, Lund and Carlsson pioneered reductive e-PRC by performing the dechlorination of chlorobenzene with an electrogenerated pyrene radical anion[6]. These early findings remained largely undeveloped until recent advances reignited interest in e-PRC, spurred by a demand for strong reducing and oxidizing agents in synthetic chemistry.

Today, e-PRC's synthetic applications have expanded, including challenging reductions and oxidations. A notable example is the reduction of aryl halides using *N*-arylmaleimide (NMI) catalysts, pioneered by the Wickens group, which achieved reductions more potent than those possible with lithium or sodium metals[26]. Similarly, the oxidative potential of trisaminocyclopropenium (TAC) salts enables selective oxidation of C-H bonds, reaching a reduction potential of +3.33 V vs. SCE upon photoexcitation[22–24]. Likewise, tris(para-substituted)biarylamines (TPAs) achieve coupling of arenes and azoles when photoexcited, reaching potentials up to +4.4 V vs. SCE[27].

- *Recycling e-PRC*

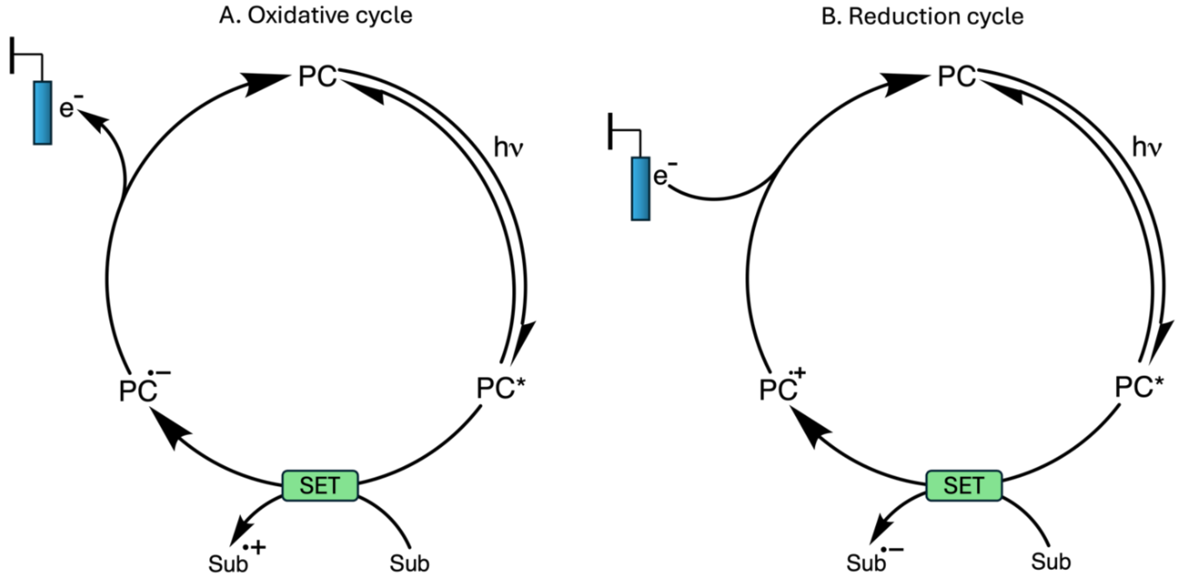

Scheme 7. General mechanism for recycling electrophotocatalysis (recycling EPC) in the case of (A) oxidation and (B) reduction.

In recycling electrochemical photoredox catalysis (*recycling* e-PRC), the role of the electrochemical component shifts from directly forming an active photocatalyst at the electrode (in the case of e-PRC) to only regenerating the catalyst to close the catalytic cycle. In this system, while electrochemical activation isn't directly needed to drive the reaction, it is essential for catalyst turnover, replacing the need for sacrificial oxidants or reductants typically used in photocatalytic cycles. This two-step mechanism begins with the traditional photoexcitation of a catalyst, which then interacts with a substrate to yield the product. The catalyst is subsequently regenerated at the electrode, allowing for continuous cycling without additional reagents. This approach, shown in Scheme 7, makes recycling e-PRC a sustainable and efficient strategy in catalysis[6,9]. This recycling approach in photoelectrochemistry provides a sustainable alternative by eliminating sacrificial reagents, expanding the utility of e-PRC in complex organic transformations.

1.1.4 Examples of reductions and oxidations via e-PRC

In general, several key requirements are essential for an effective electro-photocatalytic (e-PRC) system[7,17,18]. First, the electrophotocatalyst (EPC) must readily undergo a single-electron transfer at the electrode to form a primary radical ($EPC^{\cdot+}$) that is stable enough to be excited. This primary radical ($EPC^{\cdot+}$) should then absorb light at a wavelength different from the neutral EPC species. Finally, the excited radical state ($^{*}EPC^{\bullet+}$) must have a sufficient lifetime to interact with the substrate (Sub).

To meet these conditions, EPC catalysts are often selected from well-established photocatalysts (Figure 1), typically featuring extended aromatic structures that enhance visible-light absorption[17,28]. Additionally, large aromatic systems promote intersystem crossing, allowing the excited state to persist longer as triplet or quartet states, which further supports catalytic activity.

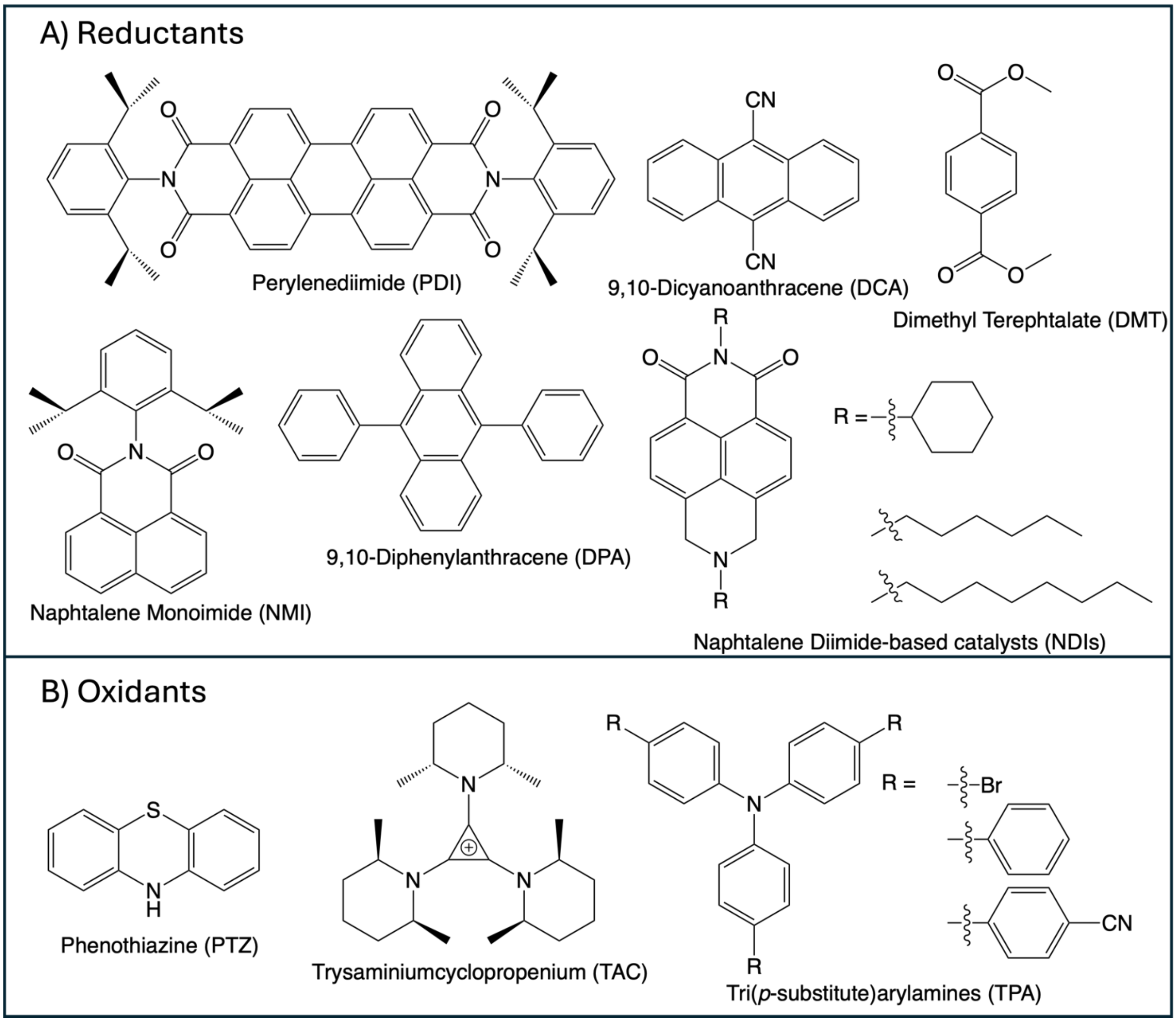

Figure 1. Structure of a typical EPC catalyst. Top (A): catalysts used for reduction. Bottom (B): catalysts used for oxidation. (PDI[29–31])(DCA[32])(DMT[33])(NMI[26,33])(DPA[33])(NDIs[34])(PTZ[27])(TAC[27])(TPA[27,35]).

Numerous other EPC catalysts have been reported in the literature[6,7,9,32], many of which share similar structural features. Despite these advancements, designing an electrophotocatalyst that combines efficiency with scalable production remains a significant challenge[3]. Figure 2 summarizes the redox properties of radical ion photocatalysts compared to conventional photocatalysts, along with example substrates. Given the substantial number of reactions developed in recent years, we will focus on the oxidation side and more specifically on formation of new C(sp²)-N bonds using TPA and its derivatives.

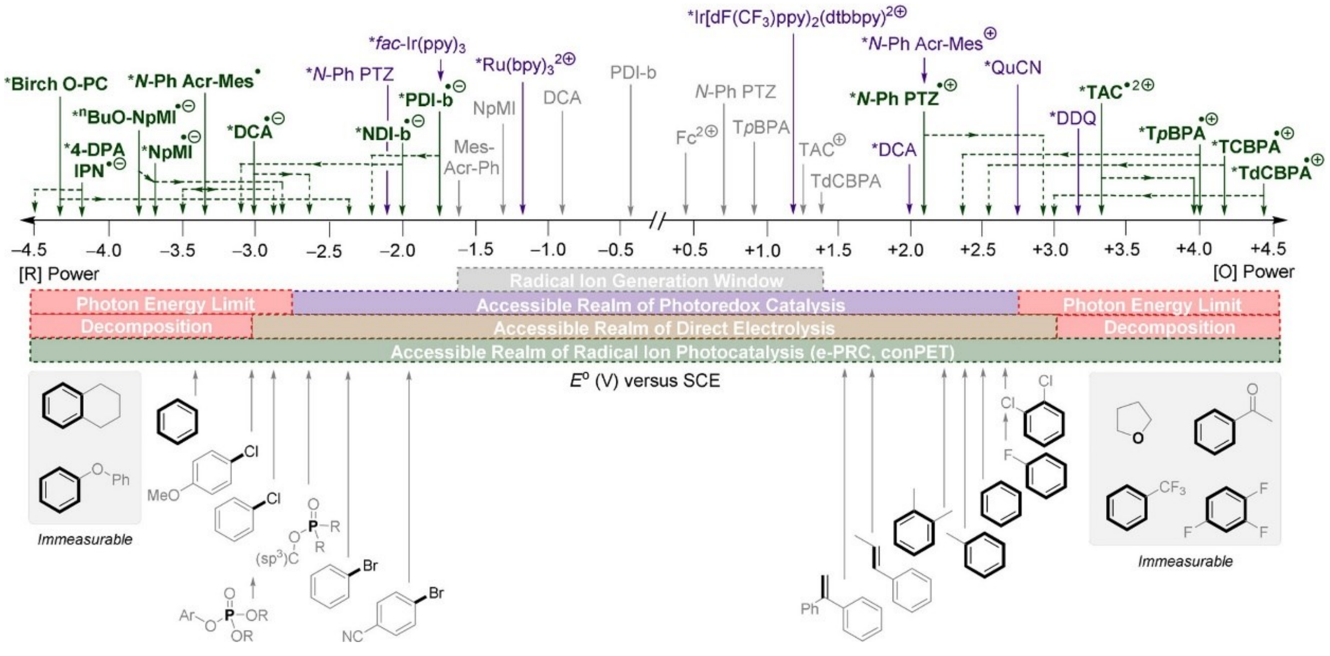

Figure 2. Redox benchmarking of modern radical ion photocatalysts against traditional photoredox catalysts and redox-demanding target substrates, taken from ref[6]

Oxidative electrophotocatalysis: State of the art

In oxidative processes, e-PRC has shown significant utility in C(sp^2)–N bond formation. The Buchwald–Hartwig coupling, a widely used reaction to create C(sp^2)–N bonds, typically requires prefunctionalization of the C(sp^2)-containing arene, such as an aryl halide or pseudohalide, to enable oxidative addition with a Pd catalyst[6]. An attractive alternative is the direct C(sp^2)–H activation of arenes through single-electron transfer (SET) oxidation to generate radical cations that can undergo nucleophilic aromatic substitution (SNAr) with nitrogen-based nucleophiles.

The Lambert[33] group further extended the limits of e-PRC by using a trisaminocyclopropenium cation (TAC^+) as an EPC with sufficient excited-state oxidation potential to target benzene, chlorobenzene, and dichlorobenzenes. Trifluorotoluene, however, showed no reaction, marking the upper limit of TAC^+'s oxidative capacity. Despite TAC^+'s broad applicability, its unusual structure limits its modification potential.[36] In the e-PRC field, structural tuning of photocatalyst cores to create variants with different photophysical and redox properties has been instrumental, especially with transition-metal and organic photocatalysts[14,17].

Tri(*para*-substituted)arylamines (*t*PAs), first introduced by Walter and colleagues[35], are well-recognized for their excellent photophysical properties, making them valuable as hole-transport materials in OLEDs and photovoltaics[37], oxidative mediators in electrolysis, and radical chain reaction oxidants[27]. This class of compounds is conveniently synthesized through single or few-step Suzuki cross-coupling reaction, allowing easy customization of redox and photophysical properties, which makes them highly suitable for e-PRC[6]. They exhibit fully reversible one-electron oxidations in cyclic voltammetry and are generally colorless in their neutral state, transitioning to intensely colored radical cations upon oxidation.

The Barham group demonstrated *t*PAs as a tunable class of EPCs capable of super-oxidations[27]. When oxidized anodically at constant potentials between +1.4 and +1.8 V vs SCE, TPAs form highly stable and bench-isolable radical cations, an essential trait for their photophysical and mechanistic characterization. By modifying the *para*-substituents, the oxidative strength of these radical cations can be tailored to target specific substrates. For example, moderate-strength *t*PA (*t*BPA, Figure 3) achieves selective C(sp^2)-H amination of alkylbenzenes, tolerating aldehyde-bearing pyrazoles and benzyl positions without further oxidation.

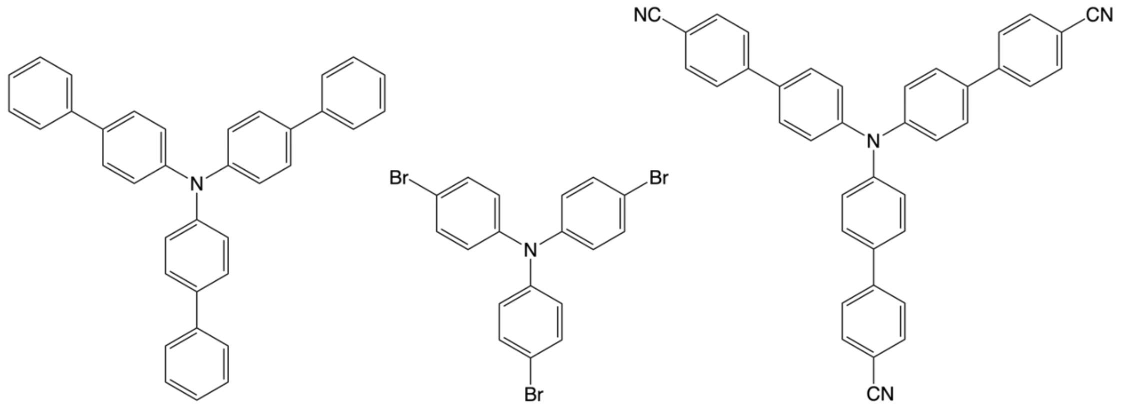

*t*PPA *t*BPA *t*CPPA

Figure 3. Structure of *t*PAs utilized in this thesis work.

More potent *t*PAs, such as *para*-cyano-substituted (*t*CPPA) and *para*-dicyano-substituted (*t*CBPA) variants, enable even more demanding transformations, including C-H aminations of benzene and chlorobenzene, as well as oxidative amination of electron-deficient dichlorobenzenes, fluorobenzenes, and acetophenone. These radical cations can activate substrates for S_NAr reactions, such as trifluorobenzene, demonstrating the versatility of *t*PAs as a customizable family of EPCs or diverse oxidative transformations[6].

In summary, photoexcited triarylaminium radical cations stand out as potent superoxidants for organic synthesis, thanks to their tunable oxidation potential, absorption spectrum, solubility, promising results, and broad applicability in challenging reactions. This thesis will focus on reactions catalyzed by the three *t*PAs catalysts shown in Figure 3, selected based on their promising reactivity as demonstrated by Wo et al[27]. Particular emphasis will be placed on using cyclic voltammetry to investigate the reaction mechanism which has been subject of debate.

1.1.5 Mechanistic debate in e-PRC reactions

A key feature of e-PRC is the ultrashort lifetimes of photoexcited radical ion catalysts, typically less than a nanosecond. This raises fundamental questions about their photochemistry, as such brief lifetimes generally preclude diffusion-controlled bimolecular reactions, limited by a diffusion rate constant of approximately $k_{\text{diff}} = 10^{10}$ $M^{-1}s^{-1}$ [18].

In recent studies, a mechanism involving precomplexation between the oxidated photocatalyst and the substrate ($[EPC^{\cdot+} \cdots RX]$) has been proposed to facilitate reactions between the short-lived excited-states catalysts and the corresponding substrates (e.g., aryl halides, RX). This precomplexation is thought to account for observed reactivity trends, such as the order of reaction yields for isomeric xylene and dichlorobenzene (reaction rate decreasing in the order 1,4- < 1,2-disubstituted arenes). The nature of precomplexes between $t\text{PAs}^{\cdot+}$ and aromatic compounds may involve π-π stacking interactions[27]. However, these precomplexes have been challenging to identify, and clear evidence of their existence is lacking.

Another challenge in studying this system is the complex and still unclear mechanism of photocatalysis involving the triarylamine radical cation. These radical cations are highly reactive unless stabilized, such as through charge delocalization. The unpaired electron in the key intermediate greatly enhances its reactivity compared to the starting compound, often triggering multi-electron processes, oxygen interactions, and chain reactions following single-electron transfer (SET) events.[38]

For *t*PAs, both the spin density and positive charge (i.e., electron hole) need to be effectively delocalized and stabilized within the π-system[39]. The stability of *t*PAs-based radical cations can be conveniently investigated using cyclic voltammetry (CV) on their neutral amine precursors, allowing observation of the reversibility of the oxidation/reduction cycle and the emergence of new signals corresponding to side products. A fully reversible CV wave indicates that the radical cation generated by anodic oxidation at the working electrode remains stable and is reduced back to the neutral amine upon cathodic reduction. In contrast, an irreversible CV signal is often a sign of decomposition and side reactions[39].

The instability of *t*PAs primarily arises from increased spin density at the ortho- and para-positions of the phenyl rings. The ortho-position is sterically hindered, making it less accessible, while the para-position is notably more reactive. Studies have reported that the *t*BPA radical cation can undergo either cyclization[38] or dimerization[39]. Unlike trityls, where α,α-dimerization is the predominant radical coupling pathway, triarylamine radical cations do not undergo α,α-dimerization, likely due to the positive charge at the nitrogen, which causes Coulombic repulsion. Instead, the main reaction pathway for triarylamine radical cations is intermolecular π–π coupling (σ-dimerization), followed by the loss of two protons, resulting in the formation of benzidine-like species such as *N*,*N*,*N*’,*N*’-tetraphenylbenzidine.

Typical methods to confirm an electro-photocatalytic mechanism involve control experiments—such as alternating light on/off, adding or removing the catalyst, or applying external potential versus no potential—to determine if the reaction remains viable. Clarifying such mechanisms demands advanced kinetic[40], spectroscopic, spectroelectrochemical[41], and computational tools[6,7,42] to fully elucidate the underlying processes.

CV as analytical tool for mechanism clarification

Recent advances in electrochemical photocatalysis (e-RPC) and conPET mechanisms highlight the utility of cyclic voltammetry (CV) for studying e-RPC systems, as proposed by Costentin et al.18. We employed CV to investigate the oxidation mechanism of triphenylamines as e-PRC catalysts, following Costentin's methodical approach, via the following steps.[18]

First, as outlined in Scheme 5 (left for oxidation), a molecular photocatalyst (EPC) diffuses to the electrode, where it is reduced to form the radical cation ($EPC^{\bullet +}$). Under steady irradiation, this reduced species absorbs light to reach an excited state ($^{*}EPC^{\bullet +}$). For effective excitation without interference, the neutral EPC should not absorb light in the same spectral region as $EPC^{\bullet +}$. The kinetics of excitation are characterized by the photon flux (I) and the molar absorption coefficient (ε). Once excited, $^{*}EPC^{\bullet +}$ can undergo nonradiative decay, engage in (SET) with a substrate (Sub). In its neutral form, EPC can undergo back electron transfer (BET) with the oxidized substrate $Sub^{\bullet +}$ (See Scheme 8) due to the favorable driving force, regenerating the initial reagents in an unproductive cycle. To investigate the magnitude and the effect of BET, we applied Marcus theory for single electron transfer, further explained in chapter 1.1.6.

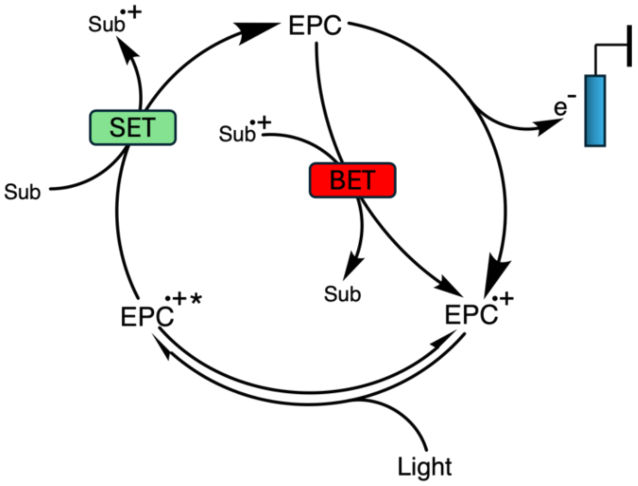

Scheme 8. General mechanism for electrophotocatalysis in the case of oxidation, with focus on back electron transfer (BET) between the neutral EPC and Sub$^{•+}$

All these factors influence the voltammetric response (see theoretical literature examples Figure 4), making it essential to identify each individual contribution to gain a clearer understanding of the system. Some challenges in voltammetric analysis of e-PRC processes persist, including (i) the heterogeneous nature of radical ion formation at the electrode surface and coupled mass transport; (ii) BET, where *EPC$^{•+}$ and Sub$^{•+}$ act as a strong reductants within the CV scan's potential range; and (iii) local heating from nonradiative decay of *EPC$^{•+}$ near the electrode, which may influence mass transport conditions. Understanding these interdependent factors—light absorption, mass transport, electron transfers—is essential and will be explored in further detail in Chapter 3.

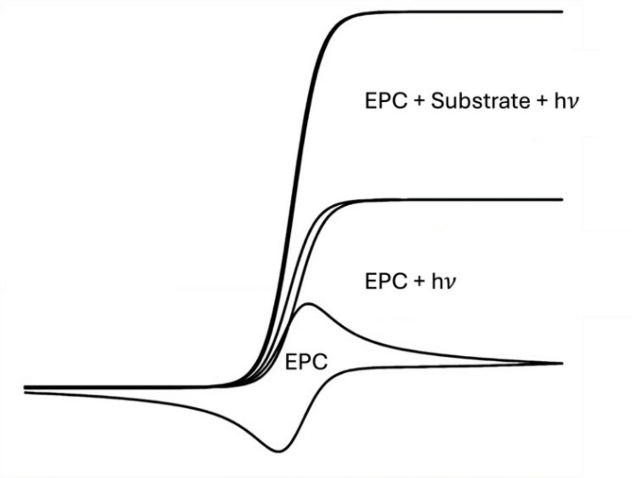

Figure 4. Representation of three simulated voltammetric curves: one with only the photocatalyst (EPC), one under light irradiation, and one with both substrate and light irradiation. Adapted from[18].

1.1.6 Marcus theory

Single electron transfer (SET) reactions can be studied with the Marcus-Hush theory, along with its later extensions. Typically, Marcus theory is applied to outer-sphere and inner-sphere ET reactions involving a donor (D) and an acceptor (A). For simplicity, we will consider D and A as neutral molecules. The theory also easily accommodates charged reactants, as electrostatic effects can be incorporated with minimal adjustments. Importantly, beyond initial energy differences in the starting states, the fundamental principles of electron transfer theory are applicable to both neutral and excited species[43].

In second-order ET reactions, the process can be broken down into three main steps. First, D and A diffuse together, forming an outer-sphere precursor complex, D|A, where they are separated by a distance comparable to r, the distance between the edges of each molecular species. The formation of this precursor complex, with rate constant k_a, generally approaches the diffusion-controlled limit. The precursor complex can either progress to the next step or dissociate back into the initial D and A species[43].

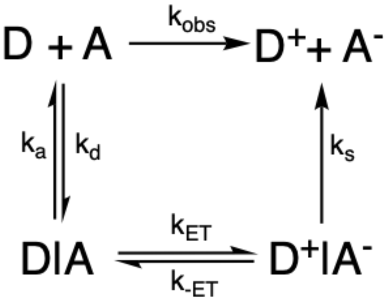

Scheme 9. Schematic representation of the three processes involved during ET reaction described by Marcus theory.

In the second step, the precursor complex D|A undergoes a reorganization, reaching a transition state in which electron transfer occurs, resulting in the successor complex $(D^+|A^-)$. Finally, in the third step, this successor complex dissociates, yielding the final products, D^+ and A^-.

In scenarios where the ET step is slow (i.e., when the diffusion rate constant, k_d, is much larger than the ET rate constant, k_{ET}), the observed rate constant (k_{obs}) follows the expression given in Equation (1), where K represents the equilibrium constant for association and dissociation, defined by the ratio of k_a and k_d.

$$k_{obs} \cong \frac{k_a}{k_d} k_{ET} = K\, k_{ET} \tag{1}$$

According to the Franck-Condon principle, the nuclei do not have time to move when the system transitions from the reactant to the product surface due to electron transfer. For electron transfer (ET) to occur, thermal fluctuations must bring the geometry of the donor-acceptor complex from the starting nuclear coordinate (A, Figure 5) to the specific nuclear coordinate (B) where the energy surfaces of the reactant and product states intersect. This is also the transition state, where the nuclear configuration of the reactant matches that of the initially formed product state. From this transition state, the ET takes place, and the product state subsequently relaxes to its equilibrium position. Thus, the reactant state must first distort from its equilibrium precursor position (A) to the transition state position (B) before ET occurs, after which the product relaxes to its equilibrium successor position (C)[44].

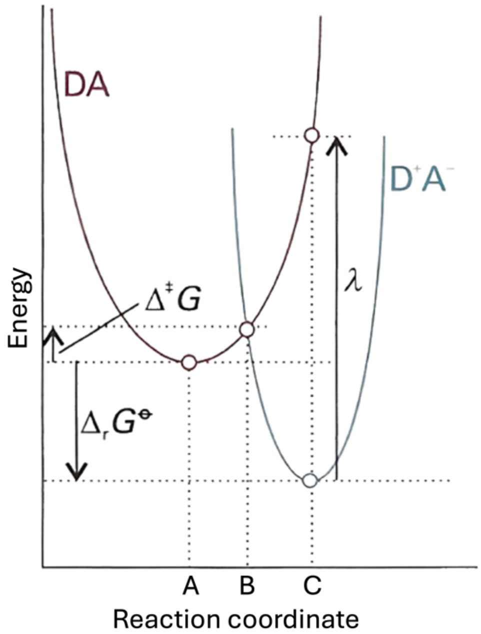

Figure 5. Diagrams illustrating the intersection of the Gibbs energy surfaces for the reactant (D|A) and the product ($D^+|A^-$), adapted from [44].

According to classical transition-state theory, the first-order rate constant k_{ET} is given by Equation (2)[43].

$$k_{\mathrm{ET}} = k_{\mathrm{el}} \upsilon_{\mathrm{a}} \exp\left[\frac{-\Delta G^{\ddagger}}{k_{\mathrm{B}} T}\right] \tag{2}$$

Here, υ_a represents the frequency of nuclear motion through the transition state $(\mathrm{D|A})^{\ddagger}$ ($\cong 10^{13}\ s^{-1}$). $\Delta G^{\ddagger}$ is the Gibbs energy of activation for the ET process, k_{el} is the electronic transmission coefficient, k_B is the Boltzmann constant, and T is the temperature.

The reorganization energy, λ, is defined as the change in Gibbs energy when the reactant state $(\mathrm{D|A})$ distorts to match the equilibrium configuration of the product state $(\mathrm{D^+|A^-})$ without actual electron transfer. This energy is typically divided into two contributions:

$$\lambda = \lambda_{\mathrm{in}} + \lambda_{\mathrm{out}} \tag{3}$$

The internal reorganization energy (λ_{in}) results from structural adjustments within the molecules involved in the electron transfer, such as bond length changes. In contrast, the outer-sphere component (λ_{out}) refers to rearrangements in the surrounding solvent or medium.

Generally, for electron transfer between organic molecules λ_{out} is larger than λ_{in} due to the extensive solvent reorganization required to stabilize the new charges post-transfer, especially in polar solvents where solvent molecules must realign around the donor and acceptor sites. The value of λ_{in} instead is generally small for large organic molecules such as most photocatalyst, which can easily accept an electron (or hole) without significant geometric rearrangements. In many applications, the inner-sphere component can be considered negligible compared to the outer-sphere reorganization, especially in systems where the reactants have relatively minor structural changes during the electron transfer process[45].

The external reorganization energy can be than calculated using the following equation:

$$\lambda_{\mathrm{out}} = \frac{(\Delta \mathrm{e})^2}{4\pi\varepsilon_0}\left[\frac{1}{2a_{\mathrm{D}}} + \frac{1}{2a_{\mathrm{A}}} - \frac{1}{r_{\mathrm{DA}}}\right]\left[\frac{1}{\varepsilon_{\mathrm{op}}} - \frac{1}{\varepsilon_{\mathrm{s}}}\right] \tag{4}$$

where Δe is the charge transferred in the reaction (almost always one electronic charge); a_{D} and a_{A} are the radii of the donor and acceptor, respectively; and r_{DA} is the center-to-center distance between the donor and acceptor; $\varepsilon_{\mathrm{op}}$ and ε_{s}, are the optical and static dielectric constants of the surrounding solvent medium and ε_0 is the permittivity of vacuum.

By inserting the reorganization energy λ into the Equation (2) and performing some mathematical manipulations, we arrive at the following expression:

$$k_{\mathrm{ET}} = k_{\mathrm{el}}\upsilon_{\mathrm{a}}\exp\left[-\frac{(\Delta G^\circ + \lambda)^2}{4\lambda k_{\mathrm{B}}T}\right] \tag{5}$$

where $\Delta G°$ is the Gibbs free energy of the reaction. As shown in Equation (5) and Figure 6, in moderately exergonic reactions, a decrease in ΔG^0 leads to an increase in k_{el}, enhancing the rate. However, as ΔG^0 becomes increasingly negative in highly exergonic reactions, the intersection point of the reactant (R) and product (P) potential energy surfaces shifts to the left of the center of the reactant surface. This noteworthy prediction suggests that k_{el} decreases as the reaction becomes highly exergonic, a phenomenon known as the *Marcus inverted region*. Physically, this implies that the product initially forms in a more distorted and higher-energy state.

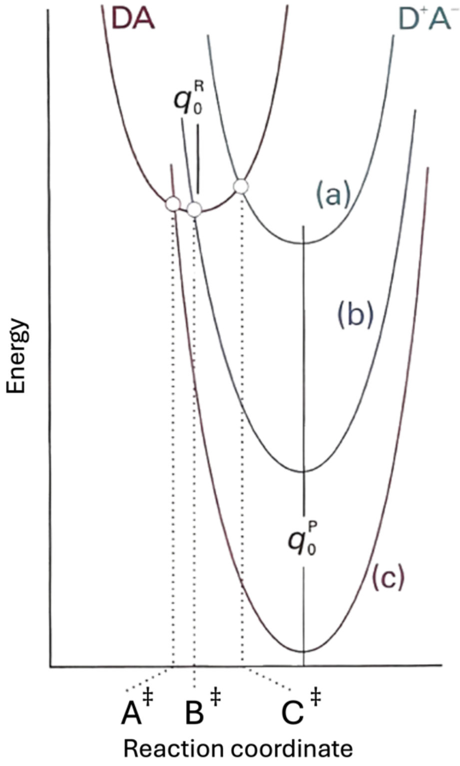

Figure 6. Diagrams illustrating the intersections of Gibbs energy surfaces for the reactant (D|A) and product ($D^+|A^-$) states across three scenarios: (a) initial moderate driving force, (b) maximum rate constant, and (c) entry into the inverted region as ΔG^0 becomes increasingly negative. Adapted from [44].

1.1.7 Aim of the thesis

This thesis presents a comprehensive investigation of electro-photochemical (e-PRC) oxidations that facilitate C−N bond formation mediated by triarylamines (*t*PAs). The study encompasses detailed electrochemical and photochemical characterization of highly reactive radical cation photocatalysts, as well as an exploration of their reactivity in promoting reactions between benzene derivatives and nitrogen-based nucleophiles.

A central focus of this work is the analysis of the e-PRC mechanism, a subject of ongoing debate, which involves multiple potential pathways, including substrate precomplexation and catalyst decomposition.

To achieve a detailed mechanistic understanding, a suite of complementary techniques has been employed, including electrolysis, UV-Vis spectroscopy, EPR spectroscopy, and especially cyclic voltammetry (CV) coupled with digital simulations. This integrated approach seeks to advance the understanding of e-PRC reactions and the underlying processes that drive them. Additionally, this thesis aims to validate CV as a reliable analytical tool for studying e-PRC mechanisms.

2. Experimental section

2.1 Chemical reagents

All reagents were used as received unless otherwise specified.

2.1.1 Solvents

Dichloromethane (DCM, 99,9%. *N*,*N*-Dimethylformamide (DMF, Carlo Erba, HPLC isocratic grade 99,9%), Chloroform-*d* ($CDCl_3$, Sigma-Aldrich, 99,8% atom % D), petroleum ether (Sigma-Aldrich, ≥ 99,9%), Toluene (Sigma-Aldrich, ≥ 99,9%), Ethanol (Carlo Erba, HPLC isocratic grade), Methanol (Carlo Erba, HPLC isocratic grade).

2.1.2 Reagents

Tris(*p*-bromophenil)ammine (Sigma Aldrich, 98%), phenylboronic acid (Sigma Aldrich, 98%). Sodium carbonate (Sigma Aldrich, 99%), tetrakis(triphenylphosphine)palladium(0) (Sigma Aldrich, 99%), 4-cyanophenylboronic acid pinacol ester (Sigma Aldrich, 99%), triazole (Sigma Aldrich, 98%), pyrazole (Sigma Aldrich, 98%).

2.1.3 Photocatalyst

Tris(4-bromo phenyl) amide (Sigma Aldrich, 98%).

2.1.4 Substrates

Bromobenzene (Sigma Aldrich, >99.5%), fluorobenzene (Sigma Aldrich, 99%), iodobenzene (Sigma Aldrich, 98 %), chlorobenzene (Sigma Aldrich, anhydrous, ZerO_2 99.8%), benzene (Sigma Aldrich, 98%), toluene (Sigma Aldrich, 98%), p-xylene (Sigma Aldrich, 98%), mesitylene (Sigma Aldrich, 98%).

2.1.5 Electrolytes

Tetraethylammonium tetrafluoroborate (*n*-Et_4NBF_4, Sigma-Aldrich, > 99%) was recrystallized in ethanol and dried under vacuum at 50 °C for 48 h. Tetrabutylammonium tetrafluoroborate (*n*-Bu_4NBF_4, Sigma-Aldrich, > 99%) was recrystallized in ethanol and dried under vacuum at 70 °C for 48 h. Tetrabutylammonium iodide (*n*-Bu_4NI, Sigma-Aldrich, >99%) was used as received.

2.2 Instrumentation

Electrodes

For the cyclic voltammetry (CV) and electrolysis experiments, three different **working electrodes (WEs)** were used:

a) A rotating disk electrode (RDE) with a glassy carbon (GC, from Tokai Carbon) tip (3 mm diameter, 0.074 mm^2 surface area, custom-made). The RDE was connected to a motor for controlled stirring. The components, except the GC tip, were purchased from Metrohm AG.
b) A reticulated vitreous carbon (RVC, from ERG Aerospace) electrode, manually cut from an RVC sheet and inserted into a graphite rod (from Staedtler).
c) A small, custom-made GC electrode.

When the electrodes were new, both the small glassy carbon (GC) electrode and the RDE tip were cleaned by polishing their surfaces. This was done sequentially with silicon carbide abrasive papers of three different grit sizes (1000, 2500, and 4000), followed by polishing with three diamond pastes —3 µm, 1 µm, and 0.25 µm— using soft polishing pads. The surface was smoothed evenly using a continuous, circular polishing motion. After each paste application, the electrode was ultrasonically rinsed in absolute ethanol for 15 minutes, then rinsed again with ethanol. Before each experiment, the GC surface was re-polished with the 0.25 µm diamond paste, ultrasonically rinsed in absolute ethanol for 15 minutes, and finally rinsed with acetone before insertion into the electrochemical cell.

For the cyclic voltammetry (CV) and electrolysis experiments, two **reference electrodes (REs)** were used based on the required dimensions, both of which were laboratory prepared. Each electrode consisted of a silver (Ag) wire coated with silver iodide (AgI), immersed in a 0.1 M solution of tetrabutylammonium iodide (*n*-Bu_4NI) in DMF. The electrodes were assembled using glass tubes with a porous (G3) frits and partially filled with agar gel to separate the reference electrode chamber from the main solution.

Due to the reference electrodes' limited stability over time and potential variability between experiments and across both electrodes, the ferrocene|ferrocenium (Fc|Fc^{+}) redox couple was used as an internal reference. At the end of each CV experiment, a small amount of ferrocene was added, followed by a CV scan within its oxidation range. This process allowed for correction of potential shifts in the reference electrode, ensuring accurate and reproducible measurements.

All measured potentials (V vs Ag/AgI) were initially converted to the Fc|Fc^{+} scale according to equation (3), where $E_{Ox/Red}$ refers to the potential of a generic redox species. The potentials were then scaled to the saturated calomel electrode (SCE) potential according to equation (4), ensuring stability across measurements.

$$E_{Ox/Red}(vs\ Fc^{+}/Fc) = E_{Ox/Red}(vs\ Ag/AgI) - E_{Fc^{+}/Fc}(vs\ Ag/AgI) \qquad (6)$$

$E_{Fc^{+}/Fc} = 0.71\ V$ vs SCE in DCM with 0.1 M n-Et_4NBF_4 [46]

Two different **counter electrodes (CE)** were used: one for cyclic voltammetry (CV) and another for electrolysis. The first electrode was a homemade assembly, consisting of a platinum wire sealed within a glass tube. The second electrode was fabricated using an aluminum wire immersed in a 0.1 M solution of tetrabutylammonium tetrafluoroborate (TBATFB) in DMF. This electrode was constructed in the laboratory with a glass tube containing a G3-grade porous frit, partially filled with a methylcellulose gel, to isolate the counter electrode chamber from the main solution.

Potentiostat

Cyclic voltammetry (CV) and electrolysis experiments were conducted using an Ivium Vertex.one potentiostat/galvanostat (Ivium Technologies), interfaced with a computer running Ivium's proprietary software.

Light source

The light sources used in electrophotochemical experiments are: Kessil P160L of 390 nm, 427nm, 440 nm and 525nm; homemade 30 W LED systems of 595nm, 730 nm, 850 nm, 950 nm (CHANZON)

UV-Vis

UV-vis measurements were registered on an Agilent Cary 60 UV-vis spectrophotometer (Xenon flash lamp, 80 Hz), connected with a computer with Cary WinUV software.

A quartz cuvette with a 1 mm path length was used. Before each measurement, the baseline was recorded and subtracted from the absorption spectra of the species.

Nuclear magnetic resonance NMR

To perform ^{1}HNMR analysis a Bruker 300, 400 and 600 Avance III HD spectrometer was used. The spectrometer is coupled with Topspin 3.5 software and equipped with a ^{1}H-^{13}C ATM-*z grad* probehead.

Electron paramagnetic resonance EPR

The spectra were recorded in capillaries (0.8 mm inner diameter) at room temperature in non-degassed solutions using a Bruker ECS106 spectrometer with a TMH cavity. Key recording parameters included a modulation amplitude of 1 Gauss (with initial spectra recorded at 0.2 Gauss), a microwave power of 2 mW (20 dB), a time constant of 20 ms, and a conversion time of 20 ms, with 10 scans performed for each sample. The receiver gain (RG) was set between $5 \cdot 10^4$ and $1 \cdot 10^5$. The spectra were processed by applying a linear baseline subtraction, and the scales were realigned to account for slight variations in operating frequencies, which ranged from 9.563 to 9.567 GHz.

CV Simulation software

CV simulations were performed with the software DigiElch8FD, and experimental rate constants were thus determined.

2.3 Methods

2.3.1 Photoelectrochemical experiment

For electro-photocatalytic experiments, a five-necked electrochemical cell was used. The cell featured side-only jacketing to allow maximum light penetration from the bottom during irradiation experiments. This setup included a three-electrode configuration: a working electrode (WE), a reference electrode (RE), and a counter electrode (CE), connected to a potentiostat controlled by a software.

Figure 7. Digital picture of the setup for CV electrophotochemistry experiments.

The central neck held a rotating disk electrode (RDE) with a glassy carbon tip (serving as the WE), used for stirring between cyclic voltammograms (CVs). The RE and CE (a platinum wire) were placed in two other necks, while the remaining necks were sealed, with one reserved for adding reagents during experiments. The cell temperature was kept constant using a Haake Q thermostat. Prior to each experiment, the cell was carefully cleaned with dichloromethane (DCM) and acetone, then dried at 60 °C in an oven.

The cell was placed inside a plexiglass box with a dark curtain to block ambient light. For irradiation, the cell was positioned over a lamp of the desired wavelength. The experiments were performed using DCM as solvent with 0.1 M electrolyte, and initial CVs of blank solutions were recorded at scan rates of 20, 40, 60, 100, 200, and 500 mVs^{-1}.

The catalyst was then introduced at a 1 mM concentration, and CVs were collected under both dark and irradiated conditions at the same scan rates. Following this, substrates and nucleophile were added to the mixture, and irradiated CVs were recorded. The concentrations of the substrates and nucleophile were subsequently adjusted as needed.

2.3.2 Electrolysis experiment

For the synthesis of the radical cation salt of the catalysts, a five-necked jacketed electrochemical cell was employed. Mixing was achieved with a Teflon-coated magnetic stirrer. The setup featured a four-electrode configuration: two working electrodes (WE, used alternately), a reference electrode (RE), and a counter electrode (CE), all connected to a potentiostat controlled by software.

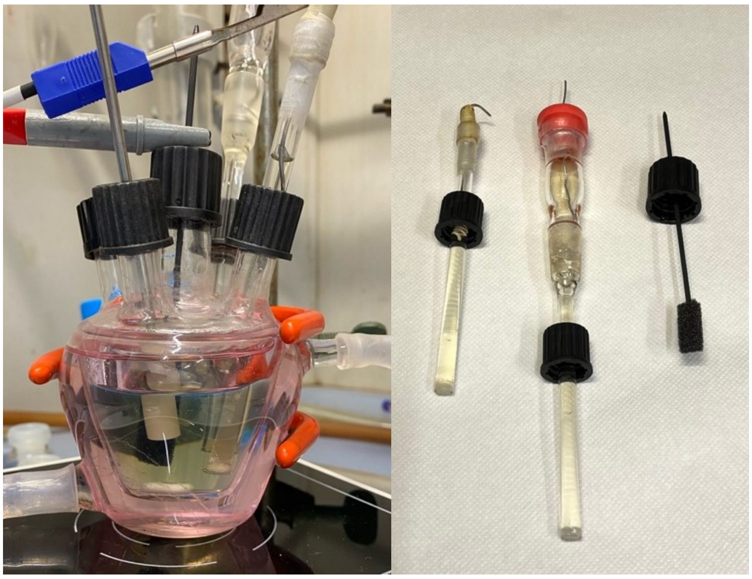

Figure 8. Left: Electrochemical setup for the synthesis of radical cation salts. Right: RE, CE, and WE electrodes used in the synthesis.

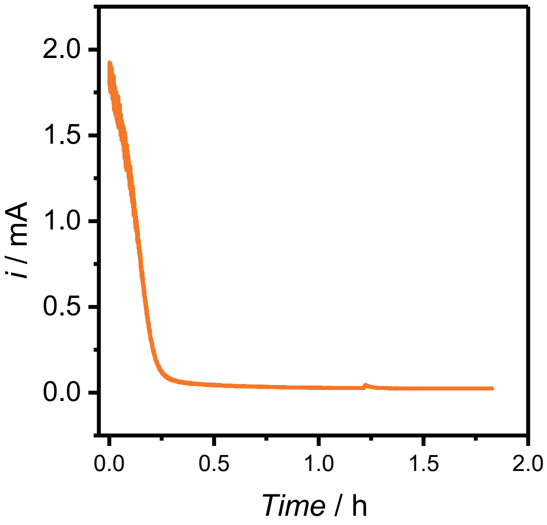

Figure 9. Electrolysis of 0.5 mM *t*BPA in DCM + 0.1 M *n*-Et_4NBF_4. Applied potential $E_{1/2}$ + 180 mV. $T = 20$ °C.

One neck housed the first WE, a small glassy carbon electrode dedicated to determining the oxidation potential. The second neck held the primary WE, a reticulated vitreous carbon (RVC) electrode used throughout the synthesis. The RE and CE occupied two other necks, while the remaining neck was sealed. Temperature was maintained using a Thermo Scientific SC100 thermostat.

Prior to each experiment, the cell was thoroughly cleaned with dichloromethane (DCM) and acetone and then dried at 60 °C in an oven. Experiments were conducted in DCM with a 0.1 M supporting electrolyte, and the catalyst was introduced at a concentration of 0.5 mM.

The prepared samples were then used as-is for subsequent analyses, including EPR and UV-Vis spectroscopy.

2.3.3 Synthesis of photocatalysts

Synthesis of tris([1,1'-biphenyl]-4-yl)amine (tPPA)

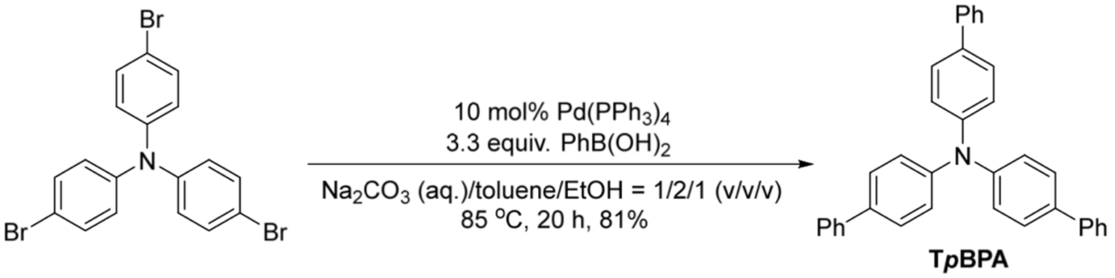

Figure 10. Schematic representation for the synthesis of tri([1,1'-biphenyl]-4-yl)amine (*t*PPA).

In a 250 mL two-neck Schlenk flask equipped with a Teflon-coated magnetic stir bar, tris(*p*-bromophenyl)amine (2.01 g, 4.24 mmol), phenylboronic acid (2.11 g, 14.3 mmol), aqueous Na_2CO_3 (2.0 M, 24 mL), toluene (58 mL), and absolute ethanol (28 mL) were added. An air condenser was attached to one neck of the flask, while the other was used for degassing and reagent addition. The reaction mixture was degassed by bubbling nitrogen through a cannula for 15 minutes. Before sealing completely, $Pd(PPh_3)_4$ (0.480 g, 0.42 mmol) was added. The mixture was then stirred at 85 °C in an oil bath, with light exclusion achieved by covering the setup with aluminum foil.

After 24 hours, as monitored by TLC, the reaction was complete. The mixture was cooled to room temperature and directly extracted with CH_2Cl_2 (3 × 50 mL). The combined organic phases were washed with brine (3 × 25 mL) and dried over anhydrous $MgSO_4$. After filtration, the solvent was evaporated, and the product was purified by column chromatography on silica gel (eluent: petroleum ether/CH_2Cl_2 = 2:8, column diameter 5 cm), yielding *t*BPA (0.55 g, 28%) as a white microcrystalline solid.

^{13}C NMR (101 MHz, CDCl3) δ 146.8, 140.6, 135.6, 128.8, 127.9, 126.7, 124.4

^{1}H NMR (400 MHz, $CDCl_3$) δ 7.61 (d, J = 4.0 Hz, 6 H, Ar-H), 7.54 (d, J = 8.0 Hz, 6 H, Ar-H), 7.44 (t, J = 8.0 Hz, 6 H, Ar-H), 7.33 (t, J = 8.0 Hz, 3 H, Ar-H), 7.25 (d, J = 4.0 Hz, 6 H, Ar-H);

Synthesis of 4',4''',4'''''-nitrilotris(([1,1'-biphenyl]-4-carbonitrile)) (tCBPA).

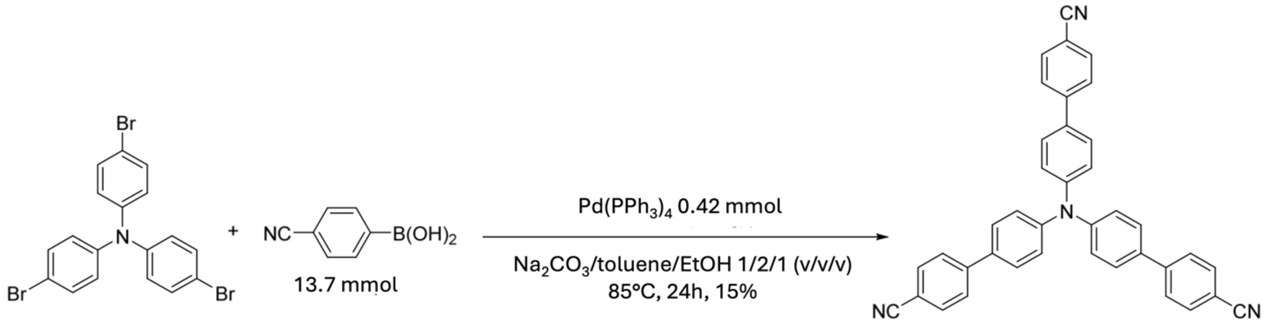

Figure 11. Schematic representation for the synthesis of 4',4''',4'''''-nitrilotris(([1,1'-biphenyl]-4-carbonitrile)) (*t*CPPA).

Into a 250 mL two-neck Schlenk flask, equipped with a Teflon-coated magnetic stirring bar, were added tris(p-bromophenyl)amine (2.06 g, 4.27 mmol), 4-cyanophenylboronic acid pinacol ester (2.11 g, 14.35 mmol), aqueous Na_2CO_3 (2.0 M, 24 mL), toluene (48 mL), and absolute EtOH (24 mL). The mixture was degassed by bubbling nitrogen via cannula for 15 minutes. An air condenser was attached to one neck, while the other was used for degassing and reagent additions. Just before sealing, $Pd(PPh_3)_4$ (0.485 g, 0.42 mmol) was added, and the reaction mixture was stirred at 85 °C in an oil bath, with complete exclusion of light by wrapping the setup in aluminum foil. After 24 hours, as determined by TLC, the reaction was completed. The mixture was cooled to room temperature and directly extracted with CH_2Cl_2 (3 × 50 mL). The combined organic layers were washed with brine (3 × 25 mL) and dried over anhydrous $MgSO_4$. Filtration, solvent evaporation, and silica gel chromatography (eluent: petroleum ether/CH_2Cl_2 = 4:6; column diameter 5 cm) yielded *t*CBPA (0.28 g, 12%) as a yellow microcrystalline solid.

^{1}H NMR (600 MHz, $CDCl_3$) δ 7.75-7.60 (m, 12 H, Ar-H), 7.58-7.57 (m, 6 H, Ar-H)

^{13}C NMR (600 MHz, CDCl3) δ147.0, 144.2, 133.5, 132.2, 127.8, 126.7, 124.2, 118.5, 110.1.

2.3.4 Synthesis of the radical cation species

In a 5-necked electrochemical cell, 20 mL of 0.1 M TEATFB in DCM was added. The cell was equipped with a small glassy carbon (GC) electrode and a reticulated vitreous carbon (RVC) electrode as working electrodes, along with a reference and counter electrode. Each electrode was carefully cleaned and inserted into the appropriate necks, with the remaining necks sealed. Three electrodes at a time were connected to the potentiostat. First, the GC electrode was connected as the working electrode (WE), and an initial scan of the solution was performed before adding the catalyst. Then, 5 mg (2 mmol) of the catalyst were introduced, and a second scan was carried out. Subsequently, the WE was switched to the RVC electrode, and the potential was held at $E_{\text{app}} = E_{1/2} + 180$ mV for 2 hours. The resulting mixture displayed an intense green color typical of the radical cations.

3. Result and discussion

3.1 Brief overview of the chapter structure

First, an electrochemical characterization of triphenylamine catalysts with various substituents is presented. This included the commercially available *t*BPA, as well as *t*PPA and *t*CPPA, which were synthesized as described in the previous section. The characterization involved determining the standard reduction potentials of the catalysts, their diffusion coefficients and heterogeneous electron transfer constant between the catalyst and the electrode. These parameters are crucial for evaluating the fundamental properties of the electrophotochemical system and providing a robust foundation for subsequent investigations.

Next, the focus shifted to a photochemical characterization. After synthesizing the radical cations of triphenylamines, UV-Vis spectra were acquired to identify the wavelengths at which these species absorb. This information was crucial for optimizing the illumination conditions when investigating the catalytic activity of the catalysts.

The following step was dedicated to examining the full e-PRC cycle. CV experiments were performed under various conditions: first to assess the effect of light on the electrochemical setup in the presence of the catalyst alone, then with the addition of the substrate, and finally with the nucleophile. These tests were conducted for all three catalysts and different substrates, providing insights into reactivity trends across the catalysts and substrate types.

A subsequent step focused on investigating the possible existence of a pre-complex, a key adduct described in the literature between the radical cation and the substrate, which is considered determinant for the observed reactivity. Techniques such as UV-Vis spectroscopy and EPR were employed for this purpose.

In the absence of conclusive evidence supporting the existence of the pre-complex, additional analyses were conducted using CV simulation software to quantify the rate coefficient of SET between excited-state *t*PPA$^{\bullet+}$ and mesitylene. These simulations enabled a quantitative evaluation of the behavior of triphenylamines as electrophotocatalysts.

Finally, CVs with different irradiation wavelengths were performed to assess the activity of different electronic excited states of tPA$^{\bullet+}$, in relation to Kasha's rule and a potential anti-Kasha behavior.

3.2 Voltammetric analysis of the catalysts in the absence of light

Cyclic voltammetry (CV), a versatile electroanalytical technique, is widely used to study electroactive species and redox reactions near the working electrode surface.[47] It offers key insights into redox behavior, electron transfer (ET) phenomena, and catalytic processes. Therefore, we chose CV as an initial tool to investigate the electrochemical properties of the catalysts and to make a preliminary assessment of the reaction mechanism.

3.2.1 Electrochemical characterization of triphenylamines (*t*PAs)

As an initial step, the electrochemical properties of *t*BPA, *t*PPA, and *t*CPPA were investigated in the absence of light or other reagents. This approach allowed for a focused understanding and quantification of their intrinsic electrochemical characteristics.

In the cyclic voltammetry (CV) performed on all three catalysts (Figure 12), each exhibited similar reversible behavior, differing only by a shift in potential. All three *t*PAs show an initial anodic peak, resulting from the oxidation occurring at the WE surface according to the following reaction:

$$\mathrm{EPC} \rightarrow \mathrm{EPC}^{\bullet +} + \mathrm{e}^{-} \tag{7}$$

If the potential is reversed after this anodic peak, a corresponding cathodic peak is observed, associated with the reaction:

$$\mathrm{EPC}^{\bullet +} + \mathrm{e}^{-} \rightarrow \mathrm{EPC} \tag{8}$$

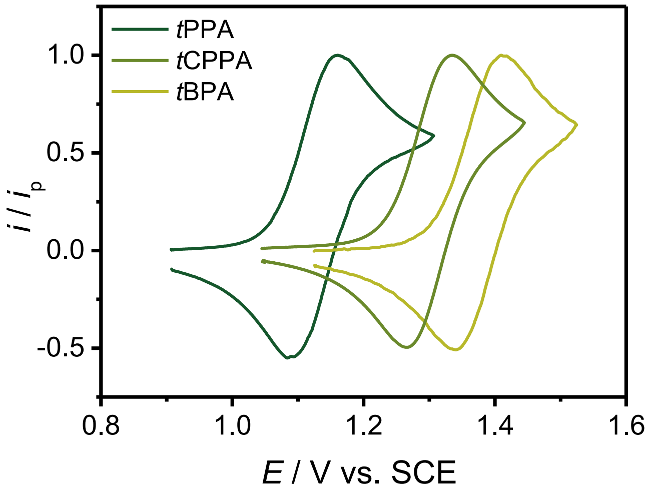

Figure 12. CV of 1 mM in DCM + 0.1 M n-Et_4NBF_4 tBPA, tPPA and tCPPA. Scan rate 20 mVs^{-1}. T = 20 °C.

When a redox couple undergoes rapid electron exchange with the WE, it is considered electrochemically reversible. In this case, the voltammogram exhibits a cathodic peak followed by a symmetric anodic peak, with equal intensity of cathodic and anodic currents (i_{pa} and i_{pa} respectively), resulting in an i_{pa}/i_{pc} ratio close to 1. For such a system, the reduction potential ($E_{1/2}$) lies midway between the peak potentials, E_{pa} and E_{pc}:[47]

$$E_{1/2} = \frac{E_{pa} + E_{pc}}{2} \tag{9}$$

Values of $E_{1/2}$ are summarized in Table 1. We can conclude that in the absence of light irradiation, the catalysts have increasing oxidating power in the order tPPA < tCPPA < tBPA.

Table 1. $E_{1/2}$, D_0 and k^0 of the catalysts studied. Values recorded in DCM + 0.1 M n-Et_4NBF_4, T = 25 °C

	$E_{1/2}$ [V vs SCE]	D [cm^2 s^{-1}]	k^0 [cm s^{-1}]
tBPA	1.38	$(1.5 \pm 0.3) \cdot 10^{-6}$	0.034
tPPA	1.13	$(9.3 \pm 0.3) \cdot 10^{-6}$	0.029
tCPPA	1.31	$(8.3 \pm 0.2) \cdot 10^{-6}$	0.015

Determination of the diffusion coefficients

Following preliminary experiments to determine the electrode's active surface area (see Appendix: Determination of the working electrode active surface area), the diffusion coefficient of the catalysts were calculated using the Randles-Ševčík equation (10).

$$i_{\mathrm{p}} = 0.4463\, nFAc \left(\frac{nF\nu D}{RT}\right)^{1/2} \tag{10}$$

In this equation, c ($\mathrm{mol \cdot cm^{-3}}$) represents the concentration of the active species, D ($\mathrm{cm^2 \cdot s^{-1}}$) is its diffusion coefficient, n denotes the number of electrons exchanged, R ($8.314\ \mathrm{J \cdot mol^{-1} \cdot K^{-1}}$) is the universal gas constant, T (K) is the absolute temperature, F ($96485\ \mathrm{C \cdot mol^{-1}}$) is the Faraday constant, A ($\mathrm{cm^2}$) represents the WE's active surface area, and ν ($\mathrm{V \cdot s^{-1}}$) is the potential scan rate[48].

By recording a series of cyclic voltammograms at different scan rates, the relationship between i_{pc} and $v^{1/2}$ was obtained (Figure 13).

The diffusion coefficient was then determined from the slope of the linear regression according to Equation (35). Table 1 summarizes the diffusion coefficients of the catalysts studied. The values of D decreased with increasing molecular weight of the catalysts, indicating that larger catalysts have slower diffusion coefficients, as expected.

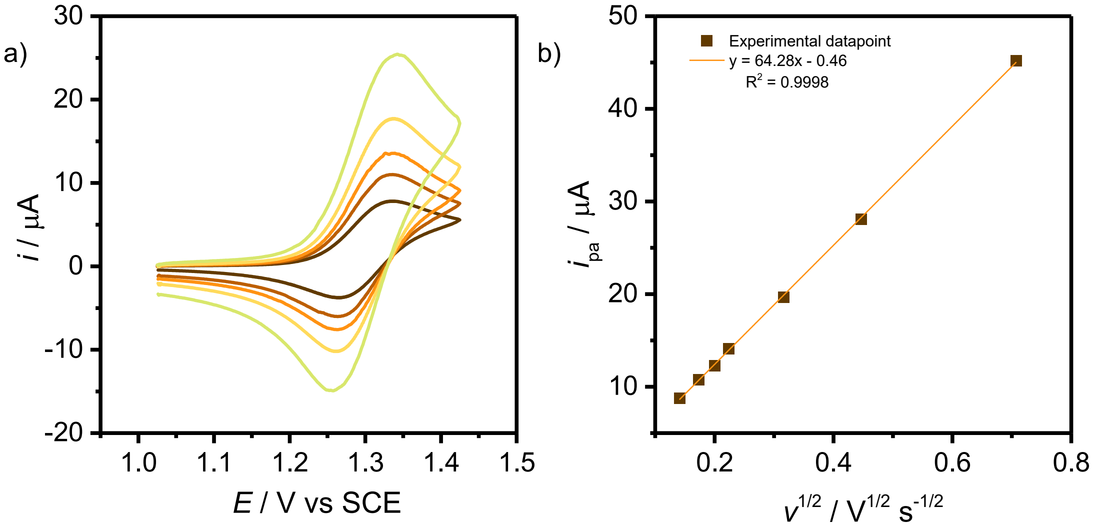

Figure 13. a) CV of *t*CPPA 1 mM in DCM + 0.1 M *n*-$\mathrm{Et_4NBF_4}$ on a GC electrode (A = 7.46 ± 0.05 $\mathrm{mm^2}$), temperature T = 20 °C. Scan rate from 0.02 $\mathrm{V\,s^{-1}}$ to 0.1 $\mathrm{V\,s^{-1}}$. b) Linear fit of i_{pa} vs $v^{1/2}$.

Determination of the standard electron transfer rate constant

In the context of a heterogeneous electron transfer (ET) process, the standard electron transfer rate constant, k^0, provides a measure of the intrinsic rate of the process. It corresponds to the ET rate constant at the standard potential of the redox pair. For a quasi-reversible redox system, k^0 can be determined using cyclic voltammetry. The shape of the peaks and their characteristic parameters, such as i_p, E_p, etc., depend on α (the transfer coefficient) and on a kinetic parameter Ψ. Specifically, the peak separation $\Delta E_\mathrm{p} = E_\mathrm{pa} - E_\mathrm{pc}$, which increases with the scan rate v, is influenced by the parameter Ψ[48].

$$\Psi = \frac{(D_0/D_\mathrm{r})^{\alpha/2}k^0}{\left[\left(\frac{nF}{RT}\right)\pi D_0 v\right]^{1/2}} \tag{11}$$

If we assume that the diffusion coefficients for the reduced and oxidized species are approximately equal ($D_0 = D_r$), equation (22) becomes:

$$\Psi = \frac{k^0}{\left[\left(\frac{nF}{RT}\right)\pi D_0 v\right]^{1/2}} \tag{12}$$

The value of k^0 can be obtained by examining the dependence of ΔE_p on logΨ. In literature, several theoretical values of ΔE_p as a function of Ψ have been reported[49]. Plotting these values produces a working curve (Figure 14 (a)), which can be used to determine k^0 by fitting experimental ΔE_p data.

The fitting process is easier and more reliable if an equation that describes the theoretical data is available. To obtain such an equation, the theoretical data were fitted to a fifth-degree polynomial, which, as shown Figure 14, closely represents the data trend. The resulting polynomial equation is as follows:

$$\begin{aligned} y &= 0.00411x^5 - 8.63143 \cdot 10^{-4}\, x^4 - 0.02649\, x^3 + 0.05387\, x^2 \\ &\quad - 0.05274\, x + 0.08391 \end{aligned} \tag{13}$$

where $y = \Delta E_\mathrm{p}$ and $x = \log\Psi$.

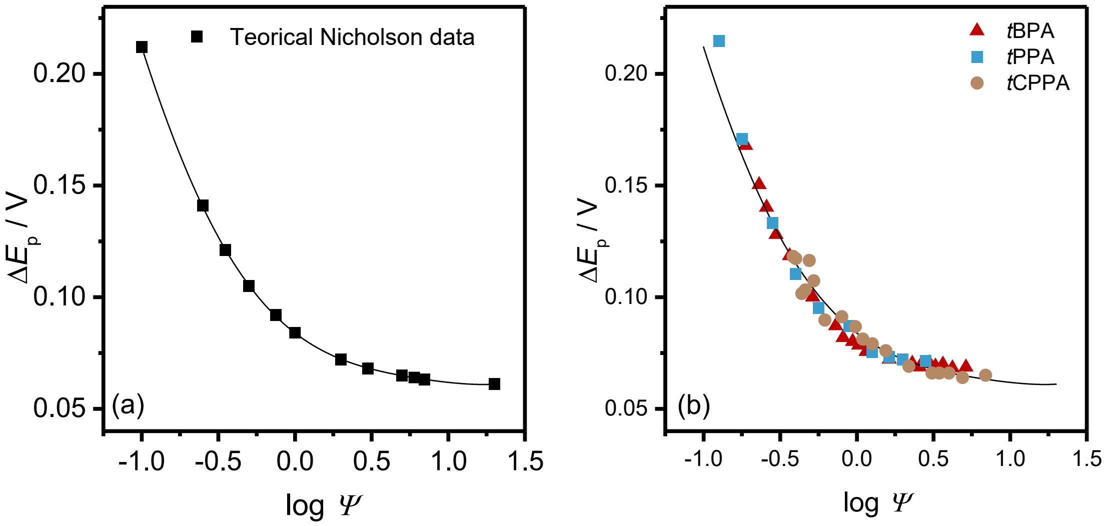

Figure 14. (a) Fitting of theoretical ΔE_p vs log Ψ data with a fifth-degree polynomial, performed to obtain a theoretical curve. (b) Fitting of the experimental data of ΔEp vs log Ψ with the theoretical curve for the oxidation of *t*BPA (red triangle), *t*PPA (brown circle) and *t*CPPA (blue square). 1 mM *t*PAs in DCM + 0.1 M *n*-Et_4NBF_4.

To determine k^0, a series of cyclic voltammograms at different scan rates were recorded for all of three catalysts (*t*BPA, *t*PPA and *t*CPPA). From these, a set of ΔE_{p} values were obtained as a function of the scan rate ν , and for each ν value, the parameter Ψ' was calculated.

$$\Psi' = \frac{\Psi}{k^0} = \left[\left(\frac{nF}{RT}\right)\pi D_0 \nu\right]^{1/2} \tag{14}$$

Which, in logarithmic form is:

$$\log \Psi' = log\Psi - log k^0 = -\frac{1}{2} log\left[\left(\frac{nF}{RT}\right)\pi D_0 \nu\right] \tag{15}$$

By performing a nonlinear regression of the experimental ΔE_{p} values against $\log \Psi'$, based on Equation (13), log k^0 was obtained. In the regression, an independent variable $x = \log \Psi' + P$ was set, and fitting was carried out by optimizing the constant $P = \log k^0$. The experimental fitting data are shown in (Figure 14), and the obtained k^0 values for the catalysts are summarized in Table 1.

The value of k^0 decreased with increasing catalyst size, likely due to the greater distance between the electrode surface and the electrochemically active center of the molecule, where the electron is removed from the triphenylamine core.

3.3 Photochemical characterization of the catalysts

The UV-Vis of the three catalysts in their neutral and radical cation form have been recorded (Figure 15). The radical cations have been prepared as described in section 2.3.4. The neutral *t*PA catalysts show a main absorption peak in the border between the UV and Vis region of the spectrum. Addition of para-phenyl and para-phenylcyano groups significantly red shifted their absorption spectra. The absorption maxima and absorption coefficients are listed below in Table 2.

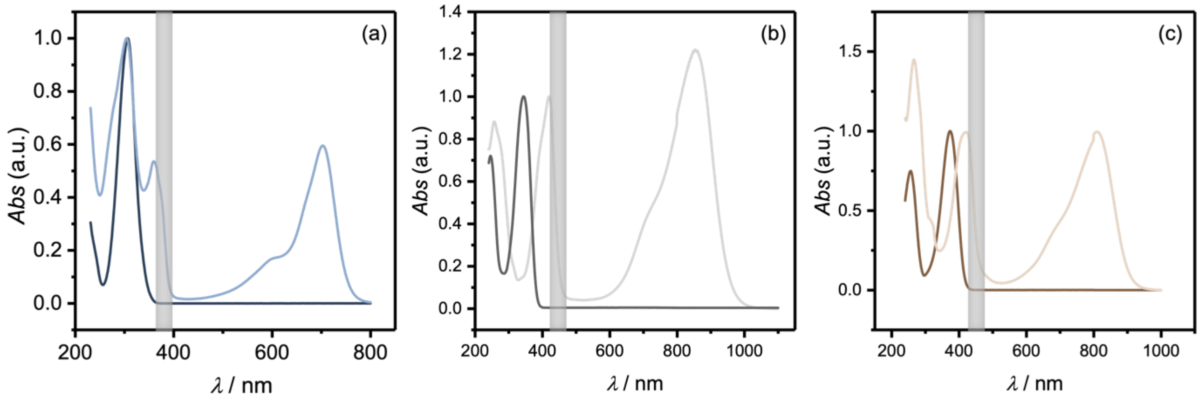

Figure 15. UV-Vis spectra of neutral species (dark line) and radical cations (shaded line) in DCM + 0.1 M *n*-Et_4NBF_4 for (a) *t*BPA, (b) *t*PPA, and (c) *t*CPPA, measured in a 0.1 cm quartz cuvette.

Table 2 Extinction molar coefficient of each peak of both the neutral EPCs and radical cations $EPC^{\bullet+}$.

Catalyst	λ peak [nm]	ε [L mol^{-1} cm^{-1}]
*t*BPA	306	10837
*t*PPA	344	12239
*t*CPPA	374	51200
*t*BPA$^{\bullet+}$	304	46100
	360	24700
	702	27450
*t*PPA$^{\bullet+}$	257	26200
	420	29800
	855	36290
*t*CPPA$^{\bullet+}$	267	45500
	421	31250
	809	31290

Two main absorption peaks are observed for the radical cations. A lower energy $D_0 \rightarrow D_1$ transition with absorbance in the Vis-Nir region, and a higher energy $D_0 \rightarrow D_2$ transition slightly red shifted compared to the absorption of the respective neutral catalyst.

This UV-Vis absorption investigation enabled to choose the appropriate wavelength to irradiate the photocatalysts. The catalyst in its neutral form should not absorb the lamp's light, while the excited species ($EPC^{\bullet+}$), which serves as the precursor to the active catalyst ($^{*}EPC^{\bullet+}$), should absorb light strongly (Figure 15).

This is crucial because if the catalyst—present at high concentration—absorbs light, it may decompose or release energy as heat during relaxation, causing strong convective currents in the solution. Such convection can interfere with the CV quality and reliability. To address this, to irradiate the radical cations without interfering with the neutral catalysts, the wavelengths listed in Table 3 were selected. Such irradiation wavelengths are also illustrated in the shaded areas in Figure 15.

Table 3. Catalyst and corresponding lamp: The wavelength corresponds to the peak of the lamp's emission spectrum.

Catalyst	*t*BPA	*t*PPA	*t*CPPA
Lamp peak λ [nm]	390	427	440

3.4 Effect of light on CV

Illuminating the electrodes while recording the CVs of the photocatalysts significantly affected the recorded currents (Figure 16). The voltammogram exhibited less reversible behavior, with the anodic current increasing in intensity and the cathodic current decreasing. This was attributed to changes in mass transfer near the electrode during the CV measurements.

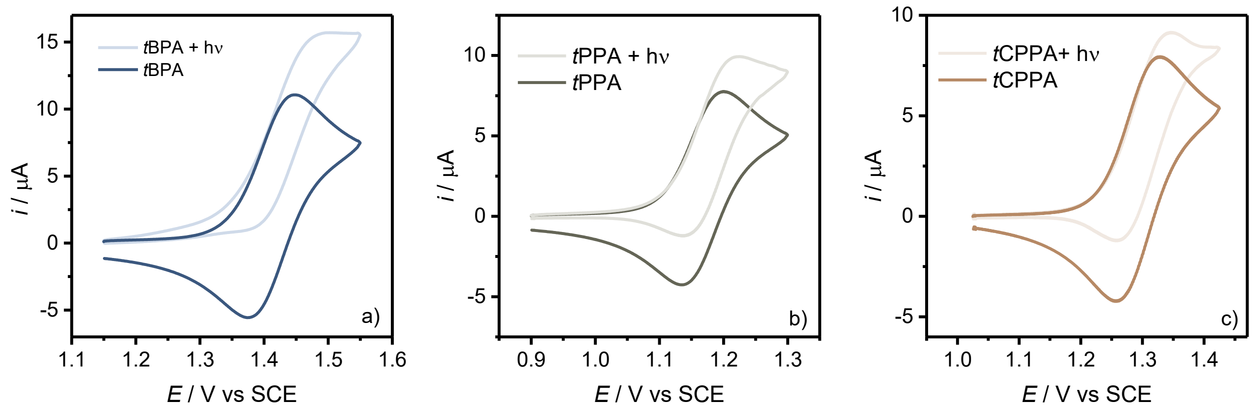

Figure 16. Comparative cyclic voltammetry (CV) of the three catalysts (a) *t*BPA, (b) *t*PPA and (c) *t*CPPA without and with light (dark and light curves). Lamps were respectively 390, 427 and 440 nm (45 watt Kessil P160L lamps). 1 mM *t*PAs in DCM + 0.1 M *n*-Et_4NBF_4.

Mass transfer typically arises from differences in chemical or electrical potential across various regions or from the physical movement of solution volumes. It can be attributed to three main mechanisms[48]:

Migration: This is the movement of charged molecules driven by electrical potential gradients.

Diffusion: Molecules move according to concentration gradients (chemical potential).

Convection: This occurs via mechanical stirring (forced convection) or as molecules move in response to density or temperature gradients (natural convection).

The mass transfer to an electrode surface is expressed by the Nernst–Planck equation, assuming one-dimensional mass transfer along the x-axis, perpendicular to the surface[48]:

$$J_{\mathrm{j}}(x) = -D_{\mathrm{j}}\frac{\partial C_{\mathrm{j}}(x)}{\partial x} - \frac{z_{\mathrm{j}}F}{RT}D_{\mathrm{j}}C_{\mathrm{j}}(x)\frac{\partial \phi(x)}{\partial x} + C_{\mathrm{j}}(x)v(x) \qquad (16)$$

where $J_{\mathrm{j}}\ (x)$ is the flux of species j (mol s^{-1} cm^{-2}) at a distance x from the surface. The terms $D_{\mathrm{j}}, z_{\mathrm{j}}$ C_{j}, and $v(x)$ represent the diffusion coefficient, charge, concentration, and velocity of the species, respectively. The three terms on the right-side account for the contributions of diffusion, migration, and convection to the flux. For an electroactive species, the flux at the electrode surface, $J_{\mathrm{j}}(x = 0)$, correlates with the current i as:

$$\frac{|i|}{nFA} = |J_{\mathrm{j}}(x = 0)| \tag{17}$$

In voltammetry, only diffusion is typically considered due to the complexities involved in including migration and convection. This is achieved by keeping the solution stationary to eliminate forced convection and by adding a supporting electrolyte at a concentration 100 times that of the electroactive species to minimize migration.

During cyclic voltammetry (CV) in dark conditions, semi-infinite linear diffusion can be assumed, as the electrochemical cell is typically large relative to the diffusion length scale. For a redox reaction $\mathrm{O} + ne^{-} \rightleftharpoons \mathrm{R}$, Fick's second law can be used to solve for concentration profiles of O and R over time and space.

$$\frac{\partial C_{\mathrm{O}}(x,t)}{\partial t} = D_{\mathrm{O}} \frac{\partial^2 C_{\mathrm{O}}(x,t)}{\partial x^2} \tag{18}$$

The excited form of the catalyst, which absorbs light similarly to the neutral form, leads to localized heating near the electrode where it is generated and illuminated. While the magnitude of this phenomenon is limited by the low concentration of the active species, this localized heating can lead to thermal convection and diffusion, influencing the mass transport near the electrode.

To model the effect of illumination on mass transfer near the electrode, we employed digital simulations of voltammograms. These simulations, which address complex phenomena involving both diffusion and convection, required selecting a suitable mass-transfer model in DigiElch 8.0. The transition from "dark" to "light" conditions was incorporated by modifying the diffusion profile, shifting from planar semi-infinite diffusion in the dark to planar finite diffusion under illumination, as described by Costentin et al.[18] Figure 17 illustrates the *t*PPA concentration profiles for both diffusion modes, with *x* representing the distance from the electrode surface. The key difference between the two modes lies in the finite diffusion regime, where a maximum diffusion layer thickness, δ, is established due to enhanced mass transport, regenerating the bulk concentration at a distance δ from the electrode.

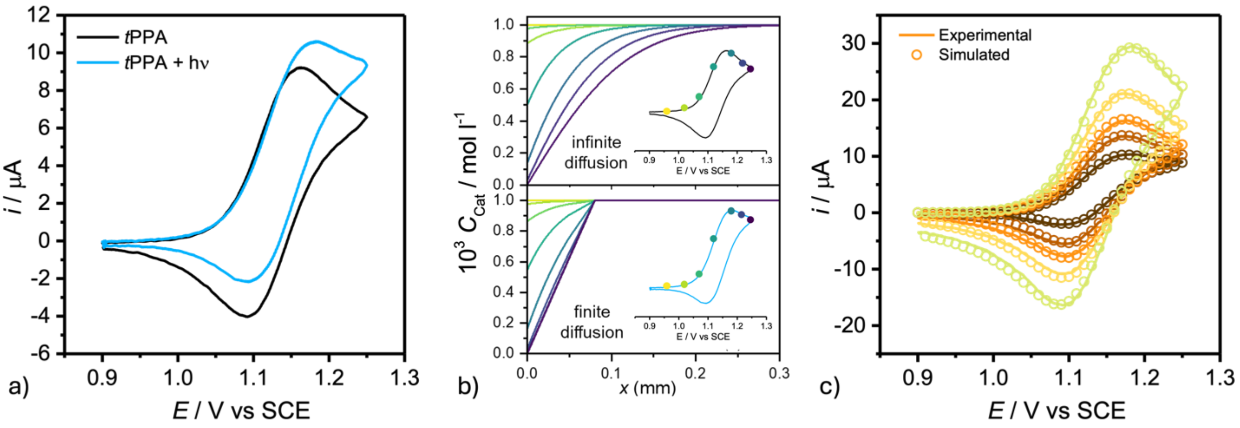

Figure 17. a) Cyclic voltammograms (CVs) of 1 mM *t*PPA in DCM + 0.1 M *n*-Et$_4$NBF$_4$ on a GC electrode (A = 7.46 mm^2) at T = 20 °C, recorded both in the absence of light and under 427 nm light irradiation. b) Simulated concentration profiles of *t*PPA during the CV of 1 mM *t*PPA under (top) semi-infinite and (bottom) finite diffusion conditions with δ = 95 µm. The dots on the CV curves indicate the potential scan points corresponding to the concentration profiles shown. c) Experimental (solid line) and simulated (dots) CVs of 1 mM *t*PPA under irradiation at scan rates ranging from 0.02 to 0.2 V s^{-1}.

Using DigiElch8FD, simulations of illuminated CVs allowed to determine the thickness δ of the diffusion layer and the diffusion coefficient D [cm^2 s^{-1}] under illumination. Simulation parameters were adjusted to achieve the best fit between experimental and simulated CVs, with a diffusion layer thickness of 0.095 mm yielding optimal results (Figure 17c). The simulated CVs exhibit excellent agreement with the experimental data, demonstrating that a single δ value adequately represents all CVs across the scan rate range. This consistency confirms that δ remains constant throughout the scans.

Figure 18 shows the trend in the standard deviation between experimental and simulated CVs at various values of δ, showing a minimum and thus best fit for δ = 0.095 mm. The simulation software also returned an increased diffusion coefficient under illumination, D = 1.01·10^{-5} cm^{2}s^{-1}.

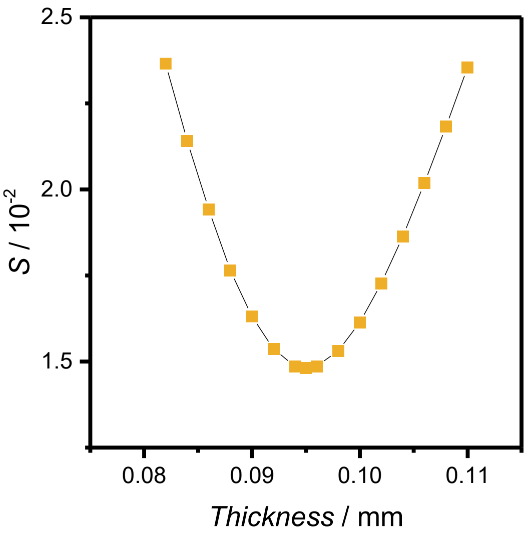

Figure 18. Thickness of the diffusion layer on the x axis vs standard deviation between the experimental points and fitted points. Optimal value is $x = 0.095$ mm. Area of the electrode 7.46 mm^2.

Estimation of the temperature increase on the electrode surface

Based on the Stokes-Einstein equation, the diffusion coefficient is directly proportional to temperature.

$$D = \frac{k_\mathrm{B}T}{6\pi\eta r} \tag{19}$$

Therefore, any change in temperature results in a proportional change in the diffusion coefficient. To assess potential heating and the temperature near the electrode surface, we conducted an experiment to determine the diffusion coefficient of the species in the dark at different temperatures. We then compared these values with those obtained from cyclic voltammograms (CVs) under illumination, obtained using simulation software. This approach enabled us to indirectly estimate the diffusion coefficient under light irradiation by correlating the changes in the diffusion coefficient with temperature variations (shown as an Arrhenius plot in Figure 19). The surface electrode temperature calculated using this approach resulted of only one degree higher than the bulk temperature, at T = 21 °C. The low viscosity of DCM likely results in significantly increased mass transfer even with minimal surface heating.

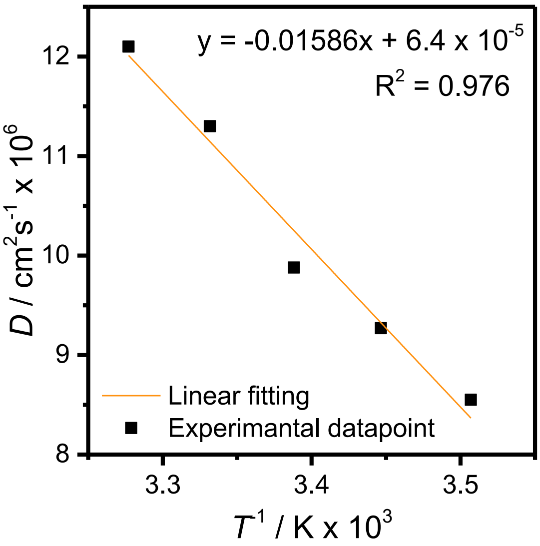

Figure 19. Coefficient diffusion of 1 mM *t*PPA in DCM + 0.1 M *n*-Et_4NBF_4 measured at 12, 15, 20, 25 and 30 °C. Temperature calculated $T = 21$ °C.

Estimation of the standard reduction potential for the excited state catalysts

Excited-state species differ markedly from their ground-state counterparts due to significant changes in both energy content and electronic structure, making them essentially distinct chemical entities with unique physical and chemical properties. Studying the properties of these excited species is essential to understanding their reactivity[50].

Estimating $E_{0,0}$ accurately is essential for understanding the redox potential in the excited state $^*EPC^{\bullet+}$. Various methods are available for estimating this value. The most common technique uses both absorption and emission spectra of the species, where the average of the peak wavelengths corresponds to the $E_{0,0}$ value. However, in this case, since the oxidized species is non-emissive, an alternative approach is necessary[51].

To estimate $E_{0,0}$ for non-emissive species, a reliable method involves analyzing the position of the long-wavelength tail in the absorption spectrum. This value is generally approximated with the onset method, as graphically shown in Figure 20 [50].

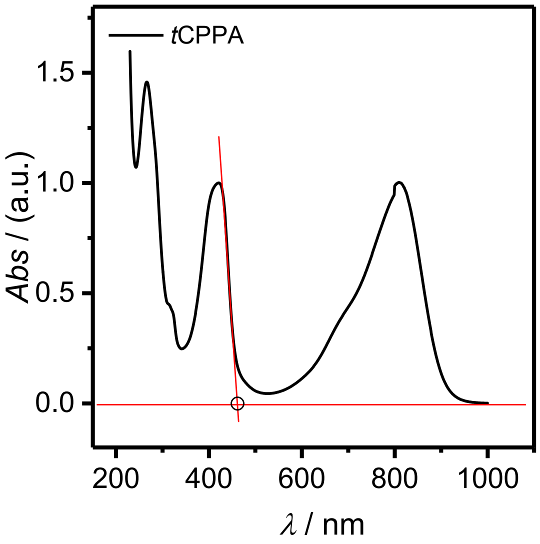

Figure 20. Example of the determination of the λ onset of the absorption spectra.

By doing so, we can approximate $E_{0,0}$ based solely on the absorption characteristics, allowing for the estimation of the excited-state redox potential. Combining this estimate with the known ground-state redox potential enables us to derive the excited-state redox potential using the relation provided in Equation (20).

$$E^* = E_{1/2} + E_{0,0} \tag{20}$$

Where $E_{0,0}$ is:

$$E_{0,0}\,[\mathrm{eV}] = \frac{\hbar c}{\lambda\, e_0} \tag{21}$$

Where $\hbar$ is the reduced Planck constant, c is the speed of light, e_0 is the elementary charge, and λ is the wavelength of the absorbed photon. This calculated redox potential is essential for assessing the catalytic power of EPC in its excited state, as it gives insight into its behavior in potential catalytic cycles (results summarized in Table 4). It appears clearly that the excited state radical cations are extreme oxidants with $E^* > 4$ V vs SCE, capable of reacting with challenging substrates.

The redox potential of the excited species was calculated exclusively for the high-energy absorption band. This approach is supported by prior studies indicating that the high-energy excited state, which absorption is located in the UV region of the spectrum, is not photoreactive due to the "anti-Kasha" behavior of these catalysts. Therefore, the potential of the excited species was determined based on the highest energy absorption band.

Table 4. Characterization of the energy of *t*PA catalysts (*t*BPA, *t*PPA, and *t*CPPA): standard oxidation potential ($E_{1/2}$ [V vs SCE]), photon absorption wavelength (λ [nm]), energy gap ($E_{0,0}$), and energy of the excited state (E^*).

	$E_{1/2}$ [V vs SCE]	λ [nm]	$E_{0,0}$ [eV]	E^* [V vs SCE]
*t*BPA	1.38	395	3.14	4.51
*t*PPA	1.13	455	2.73	3.58
*t*CPPA	1.31	462	2.68	3.99

3.5 Reactivity of the *t*PAs with benzene derivatives

We chose to use CV as our primary analytical tool to elucidate the oxidation mechanism of triphenylamines (*t*PAs) as EPC catalysts. A methodical approach to applying CV, as proposed by Costentin[18], involves first the investigation of the photocatalysts in the dark and then under illumination.

First, several benzene derivative substrates were tested with the catalysts in the absence of light to observe whether any changes in the voltammetric response—and thus catalytic activity—were

detected. As shown in Figure 21, the voltammogram remains almost completely unchanged in the presence of benzene or *p*-xylene, indicating that the "dark" catalytic cycle in Scheme 10 (A) does not occur, or at least not within a timeframe detectable by voltammetric analysis. After the oxidation of EPC at the working electrode (WE), as described by Equation (22), its reduction also occurs at the electrode, as shown in Scheme 10 (B). The substrate, therefore, shows no reactivity with *t*PPA$^{\bullet+}$.

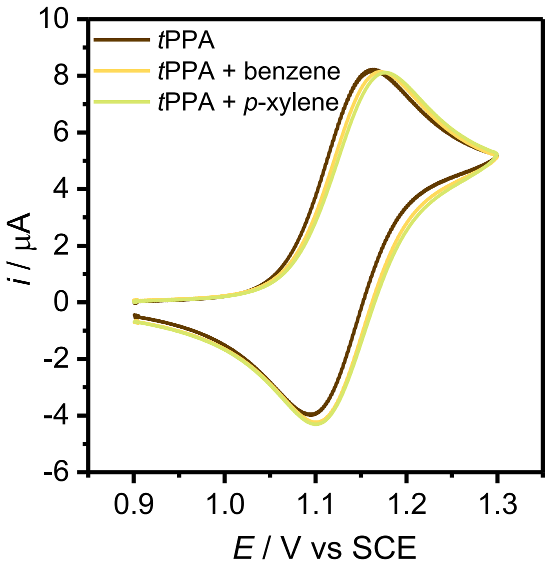

Figure 21. CV of 1mM *t*PPA in DCM + 0.1 M *n*-Et_4NBF_4 in absence of light, with and without two representative examples: benzene and *p*-xylene. Scan rate 20 mVs^{-1}, $T = 20$ °C.

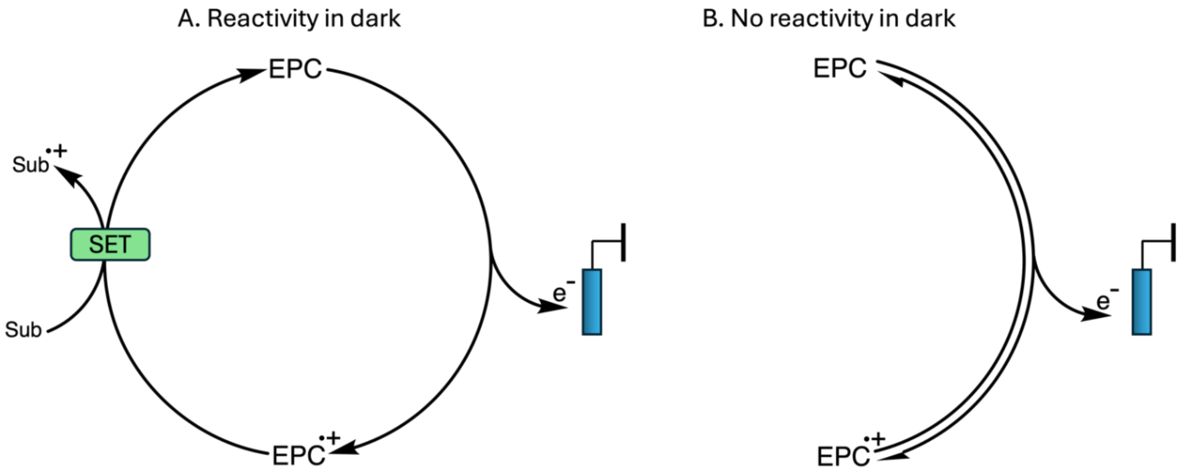

Scheme 10. Representation of the possible but not verified reactivity in dark (A), and actual mechanism in presence of the substrate in absence of light, involving only reversible electron transfer of the catalyst.

As a next step, light was introduced both in the absence and in the presence of substrates. The voltammograms in the presence of both light and substrate (Figure 22) reveal a catalytic current increase, although fairly small and much smaller than for other systems investigated in the literature[18]. In this case, the voltammogram changed for two reasons: first, due to the presence of light, as previously discussed in chapter 3.4, and second, due to the reactivity between $^{*}EPC^{•+}$ and the substrate, following the mechanism shown in Scheme 5 A, which is further explained in details below.

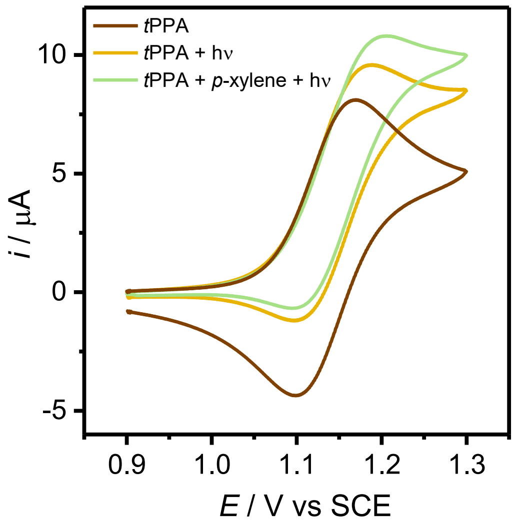

Figure 22. CV of 1mM *t*PPA in DCM + 0.1 M *n*-Et$_4$NBF$_4$ in three example cases: absence of light (brown), under 427 nm illumination (yellow) and with *p*-xylene under 427 nm illumination (green). Scan rate 20 mV s^{-1}, $T = 20$ °C.

In voltammetry, coupled reactions following the primary electrode process often lead to an increased anodic peak (or cathodic peak in the case of reductions) and the suppression of the corresponding return peak in the reverse scan.

In an electrophotocatalytic system (Scheme 11), the oxidized catalyst ($^*\mathrm{EPC}^{\bullet+}$), undergoes single-electron transfer (SET) with the substrate, regenerating EPC. This leads to repeated oxidation cycles, enhancing the anodic peak. Simultaneously, the cathodic peak diminishes, as $^*\mathrm{EPC}^{\bullet+}$ reacts with the substrate and is unavailable for reduction, causing the decrease in the cathodic peak in the return scan.

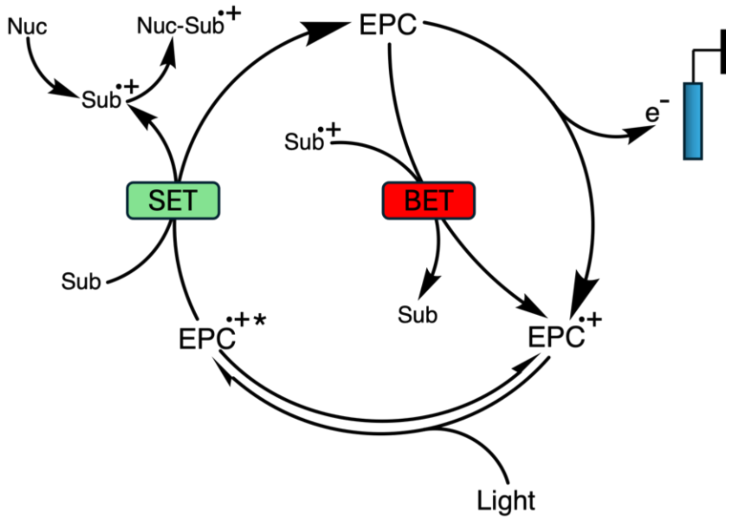

Scheme 11. Scheme of reaction of EPC catalyst in presence of substrate and nucleophile.

The complete mechanism in Scheme 11 is now thoroughly described, focusing on the processes occurring at or near the working electrode. First, the molecular photocatalyst EPC, a neutral species that diffuses in solution with diffusion coefficient D, can be oxidized at the working electrode surface, generating $EPC^{\bullet+}$ following this reaction:

$$\mathrm{EPC} \rightarrow \mathrm{EPC}^{\bullet+} + \mathrm{e}^{-} \tag{22}$$

Under steady-state irradiation by a lamp with a narrow emission band centered at the absorption maximum of $EPC^{\bullet+}$, and with a photon flux I perpendicular to the electrode surface, the radical cation $EPC^{\bullet+}$ is the only species able to absorb light (with a molar extinction coefficient ε), leading to the formation of the excited state $^{*}EPC^{\bullet+}$.

$$\mathrm{EPC}^{\bullet+} + h\nu \rightarrow {}^{*}\mathrm{EPC}^{\bullet+} \tag{23}$$

As shown in Equation (22), oxidizing the neutral EPC species produces a moderate oxidant (E1/2 = +1.13 V vs SCE, Table 4). However, to convert this already oxidized species into an extremely strong oxidant, it must absorb a photon, thereby shifting the HOMO-LUMO orbital configuration (Scheme 6). This photon absorption raises the energy of the oxidized species into an excited state, giving it significantly increased oxidative power (Table 4). The energy difference between the ground state ($EPC^{\bullet+}$) and the excited state ($^{*}EPC^{\bullet+}$) is known as the excited-state energy, typically referred to as $E_{0,0}$.

The activated photocatalyst $^{*}EPC^{\bullet+}$ has three possible pathways after formation:

i) One very probable pathway is non-radiative relaxation characterized by a rate constant $k_\mathrm{d} = \frac{1}{\tau}$, where τ is the lifetime of the excited state $^{*}EPC^{\bullet+}$.

$$^{*}\mathrm{EPC}^{\bullet+} \rightarrow \mathrm{EPC}^{\bullet+} \tag{24}$$

ii) The second possible pathway is the desired reaction with a substrate (Sub), which regenerates the photocatalyst EPC and produces the oxidized form of the substrate, $Sub^{\bullet+}$, via single electron transfer (SET).

$$^{*}\mathrm{EPC}^{\bullet+} + \mathrm{Sub} \rightarrow \mathrm{EPC} + \mathrm{Sub}^{\bullet+} \tag{25}$$

iii) The third and final pathway involves the reduction of the excited state, regenerating the neutral, ground state EPC (note: this path is not shown in Scheme 11). This step can occur through heterogeneous processes, corresponding to back electron transfer at the electrode surface. In this case, $^{*}\mathrm{EPC}^{\bullet+}$, being a strong oxidant, easily transfers an electron to the electrode within the potential range of the CV scan:

$$^{*}\mathrm{EPC}^{\bullet+} + e^{-} \rightarrow \mathrm{EPC} \tag{26}$$

This pathway, however, is extremely unlikely due to the small concentration of $^{*}\mathrm{EPC}^{\bullet+}$. An additional reduction pathway involves irreversible homogeneous reaction with the neutral catalyst, where the neutral form of the EPC is readily oxidized by the excited species due to the large oxidation potential difference.

$$^{*}\mathrm{EPC}^{\bullet+} + \mathrm{EPC} \rightarrow \mathrm{EPC} + \mathrm{EPC}^{\bullet+} \tag{27}$$

However, we note that even though this downhill bimolecular reaction likely proceeds with diffusion-limited rate constant ($k_{\mathrm{diff}} \approx 10^{10}$ M^{-1} s^{-1}), its contribution to the decay of $^{*}\mathrm{EPC}^{\bullet+}$ is negligible at a catalyst concentration of 1 mM, when compared to nonradiative deactivation given that the lifetimes of excited radical anions of photocatalysts are typically subnanosecond[52–54]. A rate comparison can be expressed by the following relations:

$$-\frac{d[^{*}\mathrm{EPC}^{\bullet+}]}{dt} = k_{\mathrm{diff}}[\mathrm{EPC}] \cong 10^{7} \ll -\frac{d[^{*}\mathrm{EPC}^{\bullet+}]}{dt} = \frac{1}{\tau} \cong 10^{10} \tag{28}$$

We will exclude these reactions of excited-state reduction from further consideration[18].

Completing the description of Scheme 11, the ground state reactants can be involved in a relevant back electron transfer (BET) reaction. Following the SET step, EPC and the oxidized substrate $\mathrm{Sub}^{\bullet+}$ are in close proximity and can react via BET (the reaction is shown in the center of Scheme 11):

$$\mathrm{EPC} + \mathrm{Sub}^{\bullet+} \rightarrow \mathrm{EPC}^{\bullet+} + \mathrm{Sub} \tag{29}$$

This reaction is highly favored due to its high driving force and can explain the observed low increase in anodic catalytic current observed in Figure 22. This BET effectively returns the system to its initial state without forming a stable product, essentially creating a short-circuit in the catalytic cycle. To validate the hypothesis that BET can strongly hamper the e-PRC cycle, Marcus theory was applied (See detailed calculation in the Appendix: Marcus theory) to calculate the electron transfer rate constant k_{BET} for reaction (29). The results, summarized in Table 5, show k_{BET} values reaching extreme values, supporting the proposed mechanism where rapid BET consumes the oxidized substrate before it evolves into products, effectively disrupting the catalytic cycle.

Table 5. Examples of calculated rate constant for the single electron transfer reaction occurring in reaction (29). Calculated using Marcus theory, see more on Appendix and Control

Catalyst	Substrate	k_{BET} [$\mathrm{L \cdot mol^{-1} \cdot s^{-1}}$]	$log(k_{\mathrm{BET}})$
*t*BPA	Mesitylene	$3.6 \cdot 10^{10}$	10.55
*t*PPA	Mesitylene	$2.6 \cdot 10^{11}$	11.42
*t*CPPA	Mesitylene	$1.5 \cdot 10^{11}$	11.16

To address the challenge posed by BET, an approach used also by Wu et al.[27] was implemented, introducing a nucleophile into the reaction system. The nucleophile aims to establish a covalent bond with the excited form of the substrate, resulting in the formation of a new molecule (Scheme 12 and equation (30)).

$$\mathrm{Sub}^{\bullet+} + \mathrm{Nuc} \rightarrow \mathrm{Sub} - \mathrm{Nuc}^{\bullet+} \qquad (30)$$

The obtained adduct then evolves to products, via a possible pathway that is illustrated in Scheme 12.

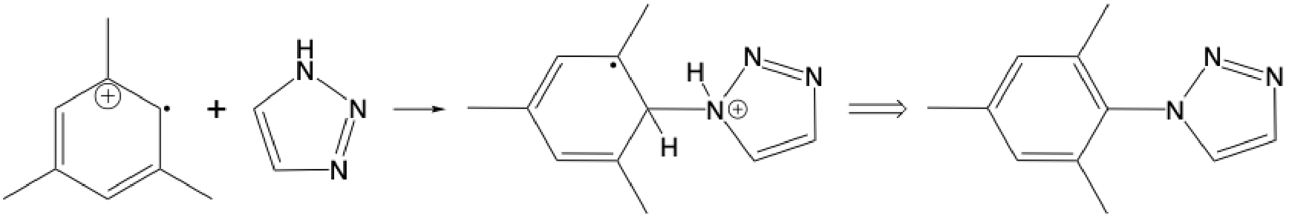

Scheme 12. Schematic Representation of the reaction between the oxidized form of the substrate ($\mathrm{Sub}^{\bullet+}$) and the nucleophile.

This molecule is incapable of re-oxidizing EPC to its neutral state, thus permitting the catalytic cycle to continue without reversion (Scheme 11). This modification enables more effective observation of an increase anodic current, due to sustained catalysis, circumventing the restrictions imposed by BET (Figure 23).

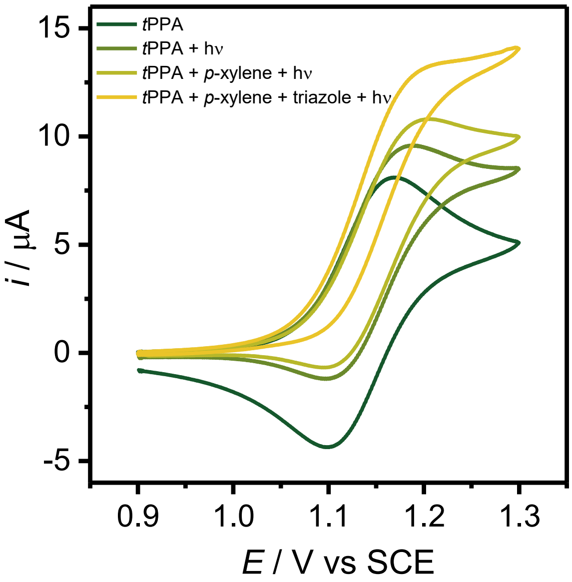

Figure 23. CV of 1 mM *t*PPA in DCM + 0.1 M *n*-Et$_4$NBF$_4$ in four cases: absence of light, under 427 nm illumination, with *p*-xylene and illumination and under illumination with *p*-xylene and triazole as nucleophile. Scan rate 20 mVs^{-1}, $T = 20$ °C.

Control experiments investigating the reactivity between the catalyst EPC and the nucleophile alone, both in the presence and absence of light, were conducted and are reported in the Appendix and Control section. These experiments revealed that EPC exhibits minimal reactivity with the nucleophile, and only under light irradiation, which is necessary to generate the catalyst's excited state (see equation (31)).

$$^{*}\mathrm{EPC}^{\bullet+} + \mathrm{Nuc} \rightarrow \mathrm{EPC} + \mathrm{Nuc}^{\bullet+} \tag{31}$$

Trends in reactivity: Catalyst effect

As the next step in characterizing the selected system, each of the three catalysts was tested with the same substrate/nucleophile pair, mesitylene/triazole, using the specific lamp corresponding to each catalyst's absorption maxima. This approach enabled a direct comparison of the reactivity of each catalyst under similar conditions, with their respective excitation wavelengths optimized for photochemical activation.

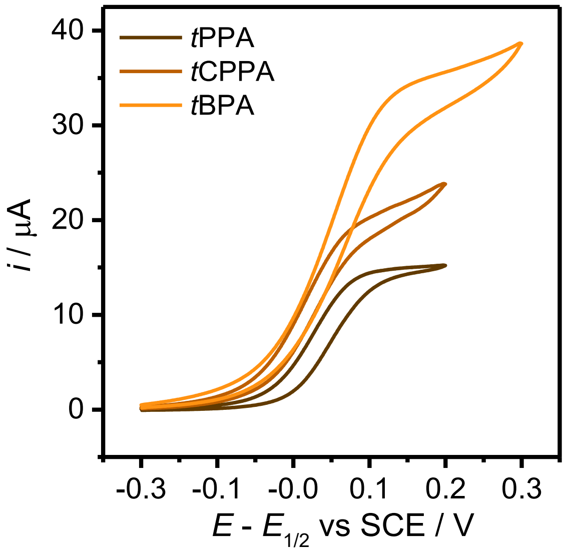

Figure 24. CV of 1 mM *t*BPA, *t*PPA and *t*CPPA in DCM + 0.1 M *n*-Et_4NBF_4 with mesitylene, triazole and under λ = 390 nm for *t*BPA, λ =427 nm for *t*PPA and λ = 440 nm for *t*CPPA. Scan rate 20 mV s^{-1}, T = 20 °C.

Figure 24 illustrates a direct correlation between the oxidation potential of the catalyst's excited state (Table 4) and the current enhancement (i.e. the degree of catalysis) observed in the voltammetric experiment. Specifically, catalysts with lower excited-state oxidation potentials show limited catalytic activity, while those with higher oxidation potentials demonstrate significantly enhanced catalysis. This trend suggests that a higher oxidation potential in the excited state is favorable for achieving more effective catalysis under the given experimental conditions.

Trends in reactivity: substrate effect

As the next step in characterizing the system, reactivity tests were conducted by varying the substrates with the three catalysts (Figure 25). Two series were investigated: the aryl halides, and the methyl-substituted benzenes.

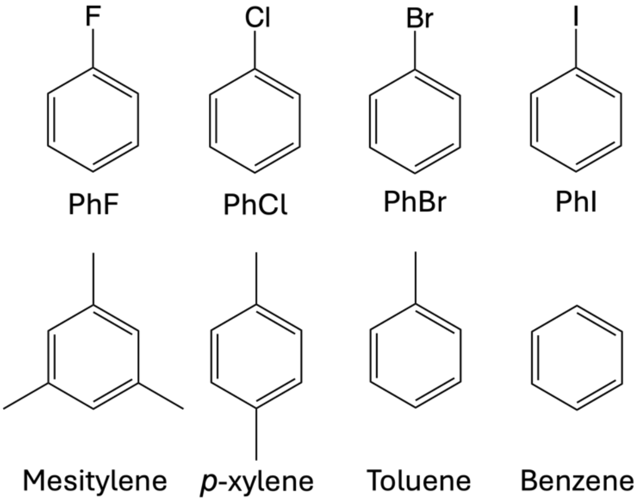

Figure 25. Substrates used to test the reactivity of the catalysts.

An example is shown in Figure 26, where the least oxidizing catalyst, *t*PPA, was tested for its electrophotocatalytic reactivity with methyl-substituted benzene derivatives, specifically benzene, toluene, *p*-xylene, and mesitylene, in the presence of triazole as nucleophile.

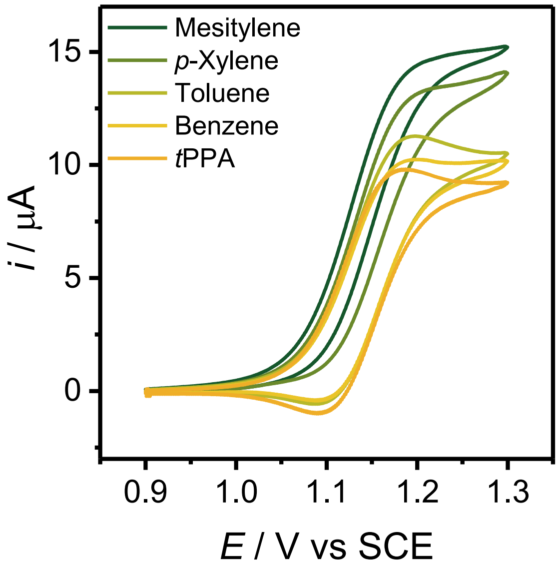

Figure 26. CV of 1mM *t*PPA in DCM + 0.1 M *n*-Et_4NBF_4 with benzene, toluene, *p*-xylene and mesitylene. Triazole as nucleophile. Under 427 nm irradiation. Scan rate 20 mV s^{-1}, $T = 20$ °C.

The figure reveals that mesitylene undergoes oxidation, evident from the catalytic peak in the voltammogram compared to the voltammogram without substrate. However, when *p*-xylene is used as the substrate, reactivity decreases slightly. This trend continues with toluene, showing even lower reactivity, and reaches a minimum with benzene. This reduction in reactivity correlates with the increasing oxidation potential of the substrates. Molecules that are easier to oxidize, such as mesitylene, exhibit higher current increase, while those that are more challenging to oxidize, like benzene, display significantly lower reactivity. The inverse relationship between standard reduction potential of the substrates and observed anodic current is visually highlighted in Figure 27. This trend was also partially observed in synthetic applications: mesitylene, *p*-xylene, and toluene could be oxidized and converted to products with good to modest yields, while benzene remained unreactive[27].

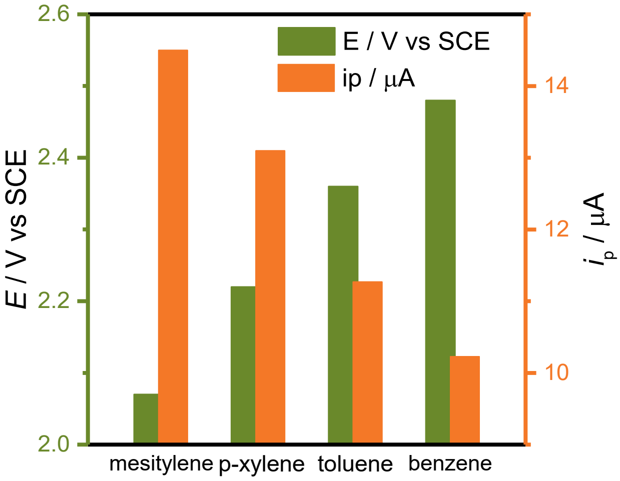

Figure 27. Figure describing the relationship between the oxidation potential of the substrate and the catalysis observed. On the left axis is reported the oxidation potential of the methyl derivates of benzene. On the right axis is reported the current of the anodic peak during the CV of 1 mM *t*PPA in DCM + 0.1 M *n*-Et_4NBF_4 with benzene, toluene, *p*-xylene and mesitylene. Triazole as nucleophile, light 427 nm, scan rate 20 mV s^{-1}, $T = 20$ °C.

As the next trend studied to determine the system's reactivity, *t*CPPA was selected as the catalyst for oxidizing benzene halide derivatives, shown in Figure 28.

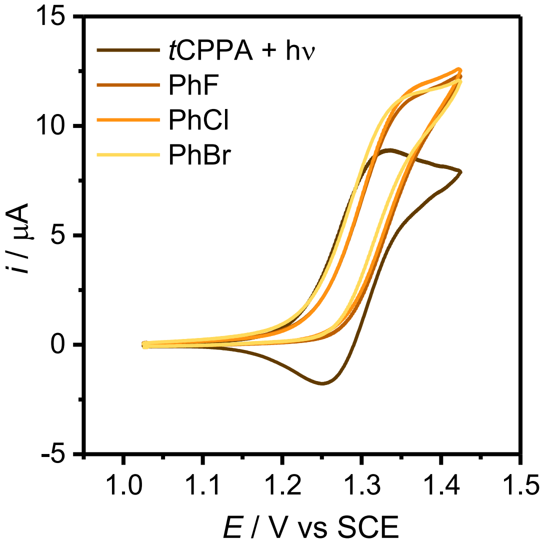

Figure 28. CV of 1mM *t*CPPA in DCM + 0.1 M *n*-Et_4NBF_4 with fluorobenzene, chlorobenzene and bromobenzene. Triazole as nucleophile, light 440 nm, scan rate 20 mVs^{-1}, $T = 20$ °C.

After conducting the experiments, the results seemed to indicate that catalysis proceeded at the same rate for all substrates, showing a consistent oxidation current despite variations in each substrate's oxidation potential. However, upon closer analysis, and supported by control experiments, it was revealed that the observed reactivity was solely due to a side reaction between the catalyst and the nucleophile. This conclusion was confirmed by a control experiment where the catalyst reacted directly with the nucleophile without the substrate present, yielding identical reactivity.

Thus, it became clear that *t*CPPA is unable to oxidize benzene derivatives. The voltammetric measurements captured only the side reaction, which appeared constant across all experiments since the conditions—same catalyst and nucleophile quantity—remained identical, demonstrating consistent reactivity with the nucleophile. Synthetically, *t*CPPA was able to react with chlorobenzene with modest yields (30-50%), although in the presence of different nucleophiles[27].

To achieve oxidation of these halogenated substrates, we subsequently selected the most oxidizing catalyst of the series, *t*BPA, and conducted CV with the same series of substrates in the absence of nucleophile. The results, shown in Figure 29, illustrate that *t*BPA successfully oxidized the substrates with variable reactivity, as evidenced by differing catalytic activity observed in the voltammetry data (the experiment was conducted in the absence of nucleophile to avoid any interference with the reactivity of the catalyst excited state, radical cation form).

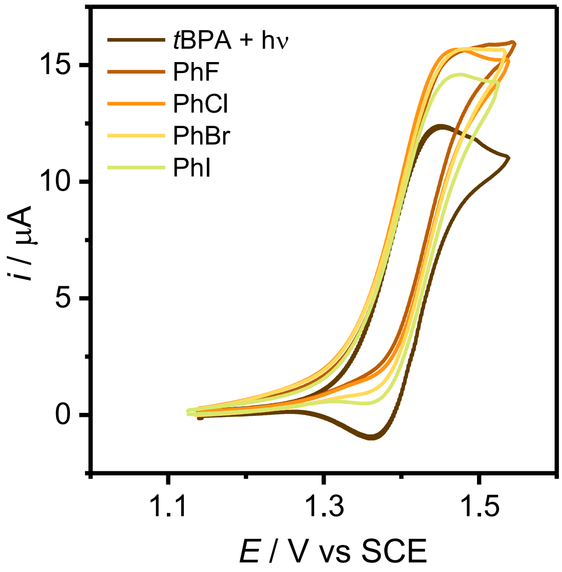

Figure 29. CV of 1 mM *t*BPA in DCM + 0.1 M *n*-Et_4NBF_4 with fluorobenzene, chlorobenzene, bromobenzene and iodobenzene. 390 nm light, scan rate 20 mVs^{-1}, $T = 20$ °C.

3.6 Investigating the potential precomplex between catalyst and substrate

After confirming the reactivity of *t*PAs as electrophotocatalysts, we focused on their potential interactions with the substrates. Recent literature hypothesizes that the reactivity of the catalysts—despite their very short lifetime on the order of a few picoseconds—is due to the formation of a ground-state precomplex. The precomplex could also explain the catalyst's selectivity among highly similar substrates. This putative precomplex could form with the catalyst in its neutral form[55], prior to oxidation, or in its radical cation state, prior to actual photoexcitation[27]. These insights motivated us to investigate the existence of such a precomplex using techniques like UV-visible spectroscopy and Electron Paramagnetic Resonance (EPR).

3.6.1 Uv-Vis

UV-visible absorption spectra of the neutral catalyst (EPC), recorded in both the presence and absence of the substrate, showed no significant spectral changes (Figure 30). This lack of alteration in the electronic density indicates an absence of notable interactions between the neutral catalyst and the substrate.

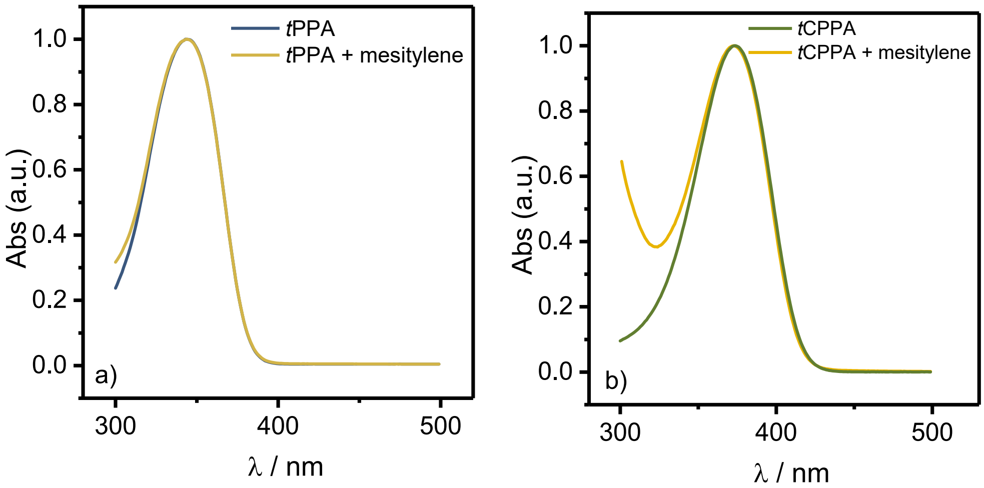

Figure 30. UV-Vis spectra of neutral species alone (dark line,) and neutral species in presence of mesitylene (light line) in DCM + 0.1 M *n*-Et_4NBF_4 for (a) *t*PPA (0.5 mM), and (b) *t*CPPA (0.5 mM), measured using a 0.1 cm quartz cuvette. Triazole 175 mM (ratio 1 : 350). The spectrum of *t*BPA is not reported because its absorption band is disturbed by the substrate's absorption, as the two bands partially overlap.

Then, the radical cations ($EPC^{\bullet+}$) were synthesized from the neutral catalysts via electrolysis in an electrochemical cell (see details in section 2.3.4). Next, UV-visible spectra of the radical cations were recorded and compared with those of the radical cations in the presence of various substrates (Figure 31). Again, no significant shifts or changes in absorption bands were observed. This absence of spectral variation suggests that no precomplex forms between the radical cation catalyst and the substrate, as any expected interaction would likely manifest as shifts or intensity changes in the absorption bands, reflecting a redistribution of the catalyst's molecular orbitals upon interaction with the substrate.

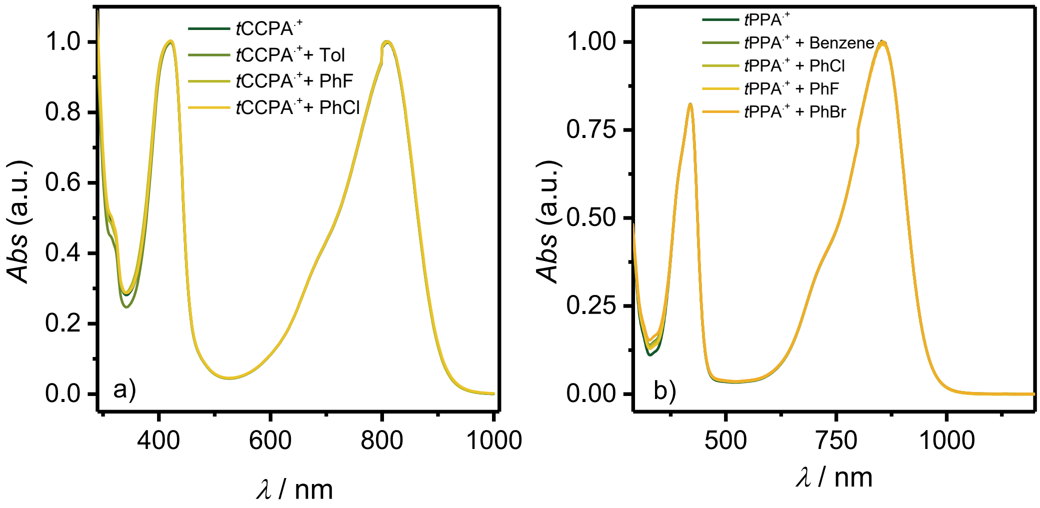

Figure 31. UV-Vis spectra of radical cation EPC$^{•+}$ alone (dark green line) and EPC$^{•+}$ in presence of different substrates (light line) in DCM + 0.1 M *n*-Et_4NBF_4 for (a) *t*PPA (0.5 mM), and (b) *t*CPPA (0.5 mM), measured using a 0.1 cm quartz cuvette. Substrate 175 mM (ratio 1 : 350).

3.6.2 EPR

EPR spectroscopy is widely recognized for its ability to provide detailed insights into the interactions that define a paramagnetic center, including cases where molecular precomplexes or other subtle interactions may alter the electronic environment of the unpaired electron. By detecting changes in electron density and analyzing the interactions between paramagnetic species and their surroundings, EPR serves as a powerful tool to investigate molecular interactions[56]. This capability is particularly valuable for identifying and characterizing precomplex formations. To further explore the potential formation of precomplexes, EPR spectra were also collected, in collaboration with Prof. L. Franco. First, the radical cation's (EPC$^{•+}$) EPR spectrum was recorded as a reference. Then, spectra were acquired for the radical cation in the presence of a large excess of several substrates. The spectra obtained are all very similar to each other (the sharp signal observed in the central region of some spectra is not significant and it is separately discussed below). The optimized spectra, recorded under ideal instrumental conditions, is shown overlaid in Figure 32.

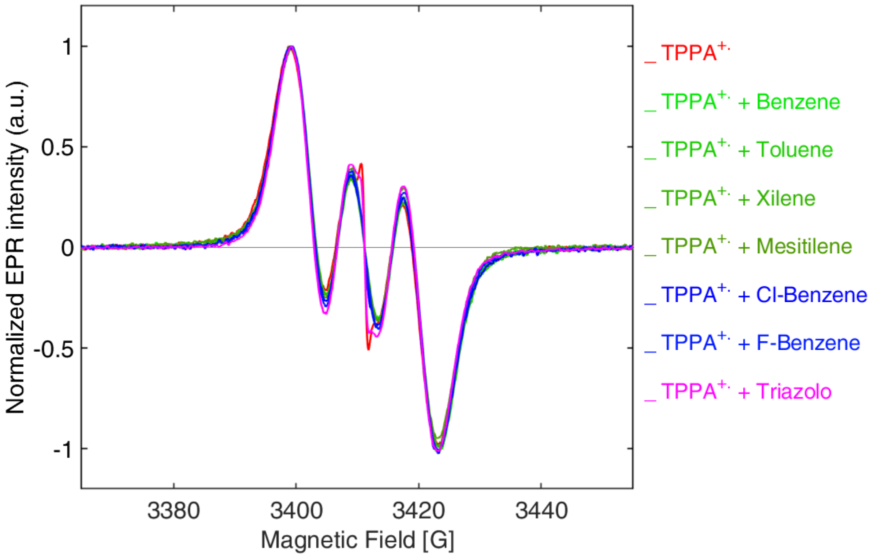

Figure 32. EPR spectra of 0.5 mM *t*PPA$^{\bullet+}$ in DCM + 0.1 M *n*-Et$_4$NBF$_4$ alone and in the presence of different 350 mM substrates. Lines are superposed to enhance differences.

In Figure 33, the same spectra are displayed with a vertical offset for clarity.

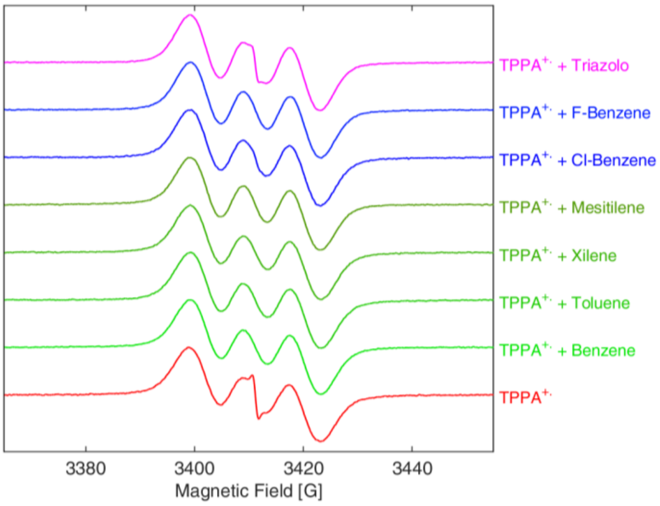

Figure 33. EPR spectra of 0.5 mM *t*PPA$^{\bullet+}$ in DCM + 0.1 M *n*-Et$_4$NBF$_4$ alone and in the presence of different 175 mM substrates. Lines are shifted for clarity.

The spectra exhibit three lines attributed to the hyperfine coupling between the unpaired electron and the nitrogen nucleus (I = 1). No hyperfine lines for hydrogen are observed, likely due to very small coupling constants that result in line splitting below the width of the nitrogen lines, causing only inhomogeneous broadening (Gaussian lines) of the three nitrogen peaks.

The spectra are accurately simulated by considering only nitrogen coupling, with an isotropic hyperfine constant a_N = 8.7 Gauss and primarily Gaussian line shapes. For example, in *t*PPA +

benzene (Figure 34), the nitrogen hyperfine constant (a_N = 8.7 Gauss) closely matches values reported in the literature for triarylamine cation radicals[57].

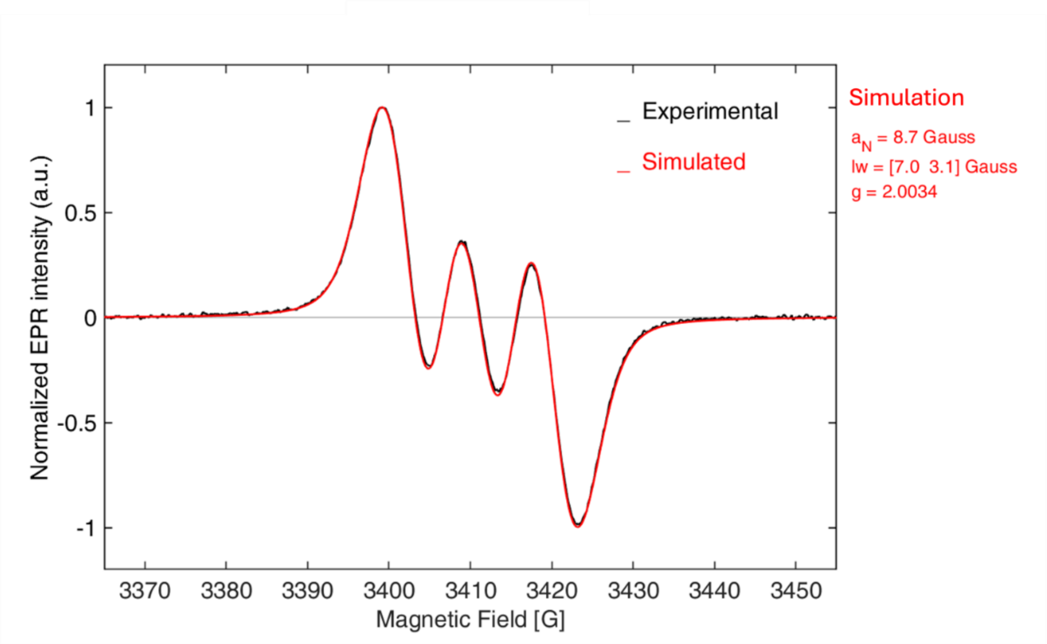

Figure 34. Experimental EPR of the radical cation *t*PPA$^{\bullet+}$ (black line) and simulated EPR spectra (red line).

The *t*PPA cation radical exhibits a slight decrease in a_N compared to other *para*-substituted (typically 9–10 Gauss), possibly due to the extended delocalization of the unpaired electron across biphenyl fragments, which reduces spin density on the nitrogen and, consequently, the coupling constant.

Across measured samples, the constant varies minimally (around 0.05 Gauss, near the experimental error margin), and line width changes are also minor, within 0.2 Gauss on an average width of 8 Gauss. These slight variations between samples might be due to random factors and do not appear to correlate with substrate characteristics or concentration.

The spectra of *t*PPA alone and *t*PPA with triazole display one or more faint central lines in the middle of the spectrum, which do not match the simulated spectrum (Figure 35).

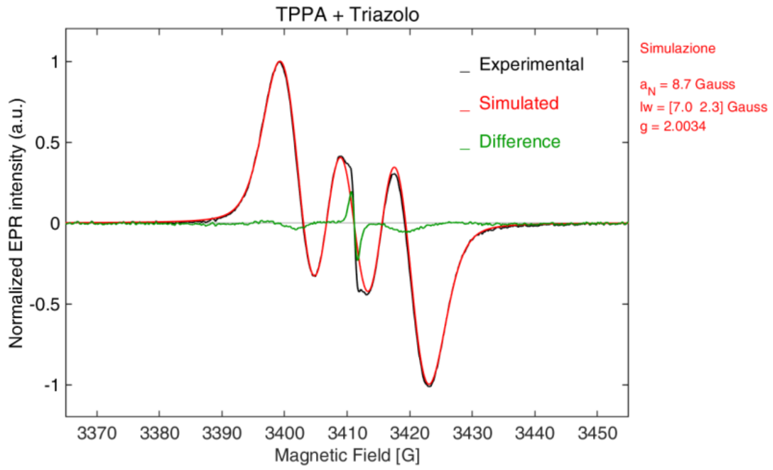

Figure 35. Experimental EPR of the radical cation *t*PPA$^{\bullet+}$ (black line), simulated EPR spectra (red line) and difference between the two spectra (green).

These central lines are weakly present in other spectra as well but do not appear to be reproducible. For instance, *t*PPA spectra taken at different times do not consistently show these lines. The following figure (Figure 36) presents all the recorded spectra, with certain samples measured at least twice for comparison.

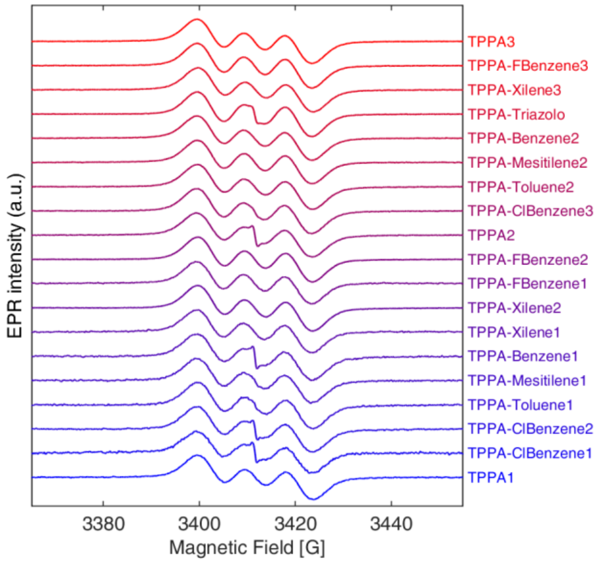

Figure 36. EPR of the radical cation *t*PPA$^{\bullet+}$ alone and in presence of different substrates.

Overall, no spectral differences suggest the formation of a complex between the cation radical and the added aromatic substrates, even though the substrates are present in large excess relative to the cation radical (0.5 mM *t*PPA and 175 mM substrates).

Overall, UV-Vis and EPR suggest that a precomplex between EPC$^{\bullet+}$ and the investigated substrates may not form. CV analysis in the dark (Figure 21) also supports the absence of any specific catalyst-substrate interaction, as they show no variation in the presence of substrate.

3.7 Quantitative analysis of the electrophotocatalytic mechanism

To deepen our quantitative analysis of the system's reactivity, we employed CV simulation software to model voltammetric behaviour of the EPC under light. This enables to extract kinetic parameters from the CV scans. For this quantitative characterization, the *t*PPA catalyst, mesitylene as the substrate, and triazole as the nucleophile were chosen.

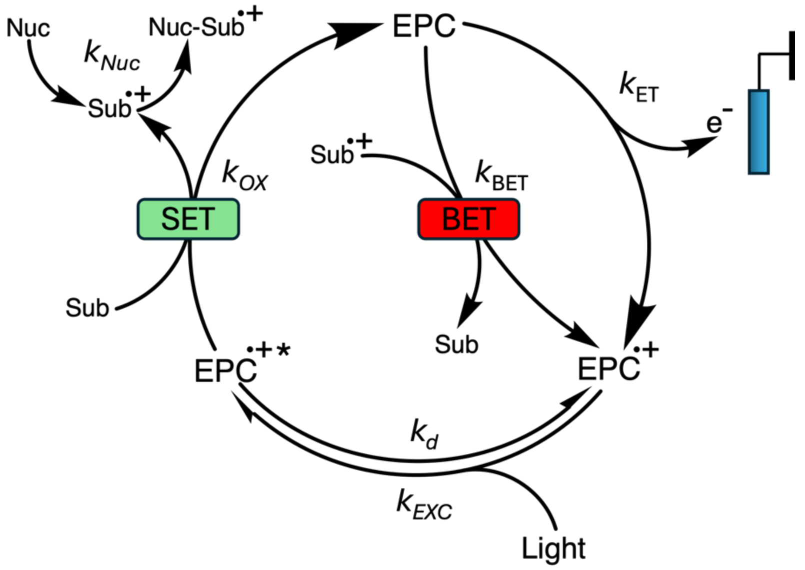

Scheme 13. Mechanism of EPC in presence of substrate, nucleophile and under light irradiation

CV simulation requires the definition of a complete electrophotocatalytic mechanism in the presence of substrate and nucleophile under irradiation, which is outlined in Scheme 13, where each reaction is accompanied by its relative rate constant. The complete list of all involved reactions is also listed in Table 6.

The mechanism selected for simulating the voltammograms is a bimolecular pathway between EPC$^{\bullet+}$ and Sub, that does not involve the formation of a precomplex. This choice was made because, although the literature suggests the formation of a precomplex, such an intermediate is elusive and labile, and no experimental evidence of its presence was observed in our data.

Starting from the neutral EPC, the radical cation is formed via electrochemical oxidation (k_{ET}). The resulting EPC$^{\bullet+}$ is excited with an observed rate coeffieicnt k_{EXC} (23). EPC$^{\bullet+}$ either decays non-radicativelly with rate constant k_{d} (24) or oxidizes the substrate with rate constnat k_{OX} (25). The generated Sub$^{\bullet+}$ can either react with the nucleofile (k_{Nuc}, (30)) or with the starting catalyst via back electron trasfner (k_{BET} (29)).

Simulation of CV requires the measuement or estimation of most rate constants pertaining to the proposed reaction mechanism. Rate constants for each reaction were derived either via Marcus theory or from the existing literature as detailed in Table 6. Only the values of k_{OX} and k_{Nuc} were unknown and thus were fitted during the CV fitting step. Experimental CVs were recorded by varying three experimental parameters: the substrate concentration (0.1-0.4 M), the nucleophile concentration (0.01-0.05 M), and the scan rate (0.02-0.2 V s^{-1}), for a total of 35 CVs recorded. This variation and large experimental dataset minimized overfitting when determining the two unknown rate constants.

Table 6. The reactions involved in the mechanism for CV simulation, along with their associated chemical-physical parameters.

Reaction	Derivation	Parameter	Value
$\mathrm{EPC} \rightarrow \mathrm{EPC}^{\bullet+} + e^-$	Experimental[a]	k_{ET} [cm s^{-1}]	0.029
		E^o [V vs SCE]	1.13
$\mathrm{EPC}^{\bullet+} + h\nu \rightarrow {}^*\mathrm{EPC}^{\bullet+}$	Experimental[b]	k_{EXC} [L mol^{-1} s^{-1}]	81
${}^*\mathrm{EPC}^{\bullet+} \rightarrow \mathrm{EPC}^{\bullet+}$	Literature[58]	k_d [s^{-1}]	$1.09 \cdot 10^{12}$
${}^*\mathrm{EPC}^{\bullet+} + \mathrm{Sub} \rightarrow \mathrm{EPC} + \mathrm{Sub}^{\bullet+}$	Fitted	k_{OX} [L mol^{-1} s^{-1}]	$1.6 \cdot 10^{10}$
$\mathrm{EPC} + \mathrm{Sub}^{\bullet+} \rightarrow \mathrm{EPC}^{\bullet+} + \mathrm{Sub}$	Calculated[c]	k_{BET} [L mol^{-1} s^{-1}]	$2.6 \cdot 10^{11}$
$\mathrm{Sub}^{\bullet+} + \mathrm{Nuc} \rightarrow \mathrm{Sub} - \mathrm{Nuc}^{\bullet+}$	Fitted	k_{Nuc} [L mol^{-1} s^{-1}]	$1.8 \cdot 10^{10}$
${}^*\mathrm{EPC}^{\bullet+} + \mathrm{Nuc} \rightarrow \mathrm{EPC} + \mathrm{Nuc}^{\bullet+}$	Experimental[d]	k_{sr} [L mol^{-1} s^{-1}]	$1.1 \cdot 10^{10}$

[a] See Appendix: Determination of the standard electron transfer rate constant. [b] See Appendix: Calculus of the photon absorbed. [c] See Appendix: Marcus theory . [d] See Appendix: Determination of *ksr.*

Figure 37 reports some examples of overlay between experimental and simulated CVs. The excellent agreement between the simulated and experimental voltammograms supports the the validity of the selected mechanism. Results indicated that $k_{\mathrm{OX}} = 1.6\times10^{10}$ M^{-1} s^{-1} and $k_{\mathrm{Nuc}} = 1.8\times10^{10}$ M^{-1} s^{-1}. The two values are extremely close and essentially match the diffusion limit for a bimolecular reaction in DCM at room temperature ($k_{\mathrm{diff}} = 8RT/3\eta = 1.7\times10^{10}$ M^{-1} s^{-1}, where η is the solvent viscosity). This suggests that substrate oxidation and subsequent nucleophile trapping are highly efficient bimolecular reactions proceeding at their maximum possible rates. No evidence of reactivity beyond the diffusion limit was observed in the simulations, eliminating the need to postulate the formation of a pre-complex to explain the reactivity.

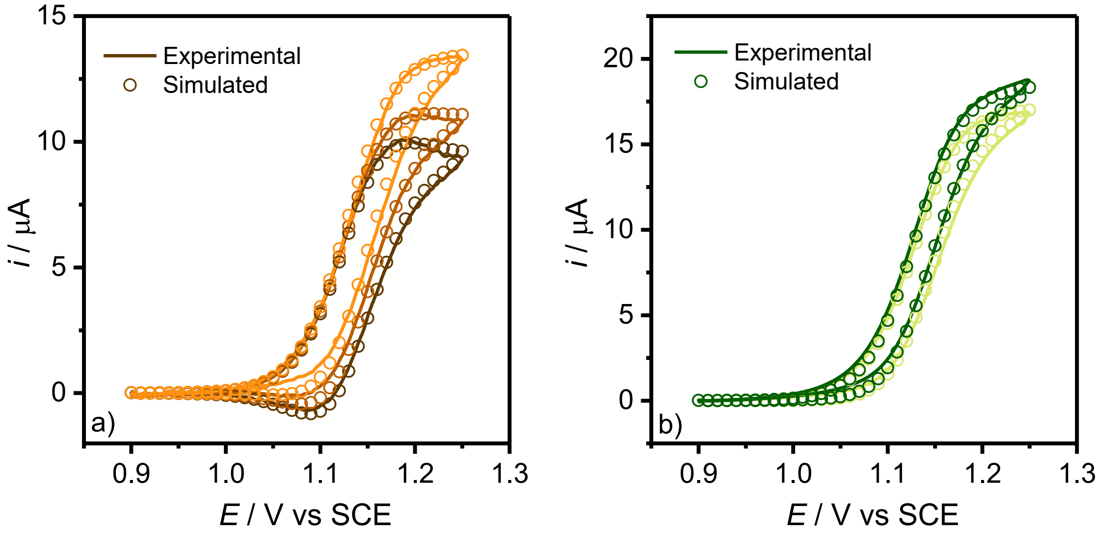

Figure 37. Experimental (line) and simulated (circles) for the CV of 1mM *t*PPA in DCM + 0.1 M *n*-Et_4NBF_4 with mesitylene and triazole. Light 427 nm, scan rate 20, 40 and 60 mVs^{-1}, $T = 20$ °C. a) Curves obtained varying the substrate concentration ($C_{Sub} = 100\text{-}200\text{-}400$ mM), scan rate 20 mVs^{-1}. b) Curves obtained varying the nucleophile concentrations ($C_{Nuc} = 10\text{-}20\text{-}30\text{-}50$ mM), only 20 and 50 mM reported for clarity, scan rate 20 mVs^{-1}.

It should be noted that the simulated CVs included an additional reaction compared to those described in Scheme 13: the unwanted side reaction between the excited-stated catalyst and the nucleophile (k_{sr}, reaction (31)). To determine the rate constant for this reaction, an experiment was conducted using only the catalyst and nucleophile as reagents (See Determination of ksr in the Appendix). This side reaction had minimal impact for the *t*PPA-triazole combination at the selected, but might be much more relevant for other catalyst/nucleophile pairing.

3.7.1 Quantifying reaction efficiency

Reaction quantum yield

Given the extremely low lifetime of $^{*}t\mathrm{PPA}^{\bullet+}$ (ca. 1 ps), the natural question is how it can have time to react with the substrate? The question can be answered by evaluating the quantum efficiency of the substrate oxidation reaction, also termed the reaction quantum yield (φ). A photoexcited catalyst can either oxidize the substrate (k_{OX}), as described by Equation (25), or relax non-radiatively ($k_d = 1/\tau$) to return to its ground state (Equation (24)). These two reactions compete by depleting the excited-state catalyst. To quantify this competition, the reaction quantum efficiency φ was defined, which is expressed in Equation (32).

$$\varphi = \frac{v_{\mathrm{ox}}}{\mathrm{v_d} + v_{\mathrm{ox}}} = \frac{k_{ox}[\mathrm{Sub}]}{k_{\mathrm{d}} + k_{\mathrm{ox}}[\mathrm{Sub}]} \tag{32}$$

Here, v indicates the rate of the corresponding reaction. Under the employed experimental conditions, which mimic the synthesis conditions used by Barham et al.[27], $\varphi = 3\times10^{-3}$ is calculated for the reaction between $^{*}t\mathrm{PPA}^{\bullet+}$ and the Mesitylene substrate ($C_{\mathrm{Sub}} = 0.350$ mM, with the other rate constant obtained from Table 6). The efficiency is low, but nonzero: essentially, out of 1000 $^{*}t\mathrm{PPA}^{\bullet+}$ formed, only 3 survive long enough to react with the substrate. This low efficiency is in agreement with the long reaction times (24-72 h) required for these transformations.

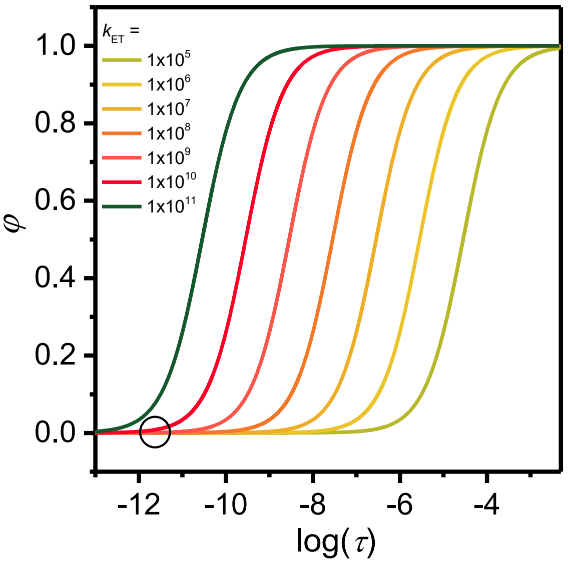

Figure 38. φ parameter vs the logarithm of the lifetime of the excited radical cation. Various curves obtained by changing the electron transfer rate constant from $k_{\mathrm{ET}} = 1 \cdot 10^{3}$ M^{-1} s^{-1} to to $k_{\mathrm{ET}} = 1 \cdot 10^{11}$ M^{-1} s^{-1}. $C_{\mathrm{Sub}} = 350$ mM.

Figure 38 plots the values of φ as function of the catalyst excited state lifetime. The graph shows a variety of efficiency curves, parametric in the value of k_{ET}. The black circle in the figure indicates the value of φ for the $^{*}t\mathrm{PPA}^{\bullet+}$-mesitylene system. Higher values of k_{ET} and longer excited-state lifetime improve reaction efficiency. Enhancing the catalyst's efficiency could involve structural modifications to extend its excited-state lifetime.

Effect of light penetration

Figure 39 illustrates light penetration in a system containing a light-absorbing substance, such as the EPC$^{\bullet+}$ used in this study. It is directly calculated using the Lamber-Beer equation (33):

$$T\ (\%) = 10^{-\varepsilon l c} \quad (33)$$

Where l is the path length and c the dye concentration. This representation is particularly valuable as it provides a quick estimation of how deeply light can penetrate the solution.

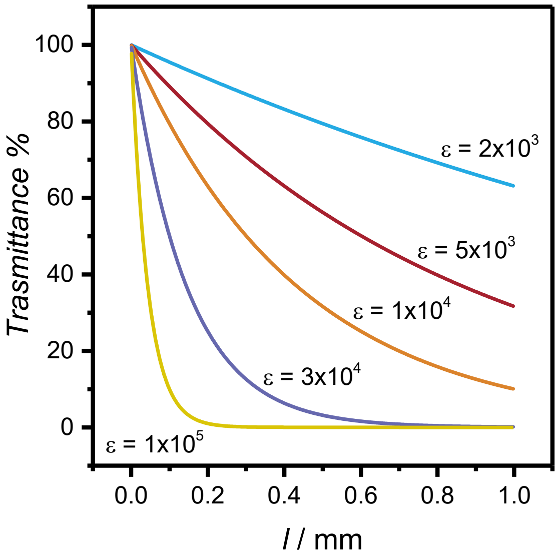

Figure 39. Representation of the light penetration depth through a solution. The parametric curves are obtained by varying ε from $2 \cdot 10^3$ to $1 \cdot 10^5$ mol L^{-1} cm^{-1}. The curve representative of our system is the one with an ε value of approximately $3 \cdot 10^4$ mol L^{-1} cm^{-1}, as the catalysts studied exhibit this characteristic absorbance.

In the context of organic synthesis, where the solution contains a bulk concentration of the light-absorbing species, even a moderate molar extinction coefficient (e.g. ~ 30,000 $M^{-1}cm^{-1}$) can lead to significant attenuation of light intensity within just a few millimeters from the light source. This rapid decay reduces the irradiance reaching the reaction mixture, potentially impairing reaction efficiency. To mitigate this issue, higher-powered lamps may be required, or the solution thickness can be minimized using techniques such as microfluidic reactors.

In voltammetry, where the light-absorbing species is generated only near the electrode surface, light intensity attenuation through the bulk of the solution is generally not a concern. However, exceptions occur with substances exhibiting extremely high molar extinction coefficients, such as chromophores.

3.8 Wavelength effect

As reported in the literature and confirmed by our UV-Vis experiments, the radical cation derived from the neutral EPC catalyst after oxidation exhibits two prominent absorption bands. The low-energy band, associated with the $D_0 \rightarrow D_1$ transition lies in the visible or IR region. The higher-energy band, associated with the $D_0 \rightarrow D_2$ transition, typically appears in the UV or far-visible region. According to previous studies, the D_1 excited state is supposed to be inactive for the type of substrate oxidations under investigation[27]. Instead, the D_2 excited state is photochemically active, indicating that the catalyst exhibits anti-Kasha behavior, that is photoreactivity from a higher order excited-state.

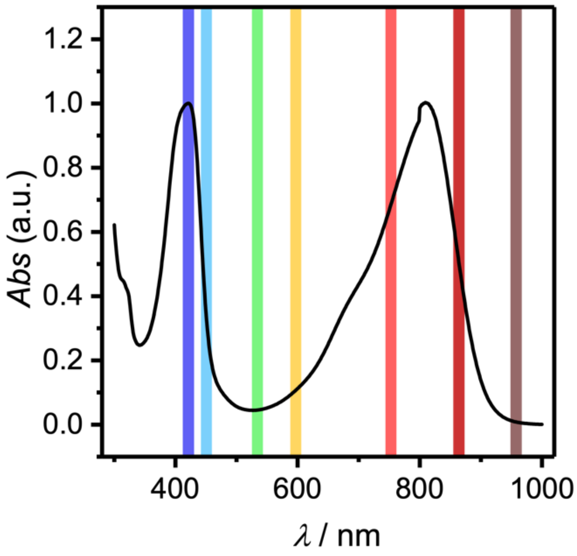

Figure 40. UV-Vis spectra of 0.5 mM *t*PPA$^{\bullet+}$ in DCM + 0.1 M *n*-Et$_4$NBF$_4$, measured using a 0.1 cm quartz cuvette. The lines represent the emission band of the lamp used to excite *t*PPA$^{\bullet+}$ to **t*PPA$^{\bullet+}$.

To investigate the reactivity of the system, we conducted a CV experiment using *t*PPA and mesitylene, adjusting only the excitation wavelength for each trial. The utilized irradiation wavelengths are illustrated in Figure 40, overlayed with the absorption spectrum of *t*PPA$^{\bullet+}$. All lamps had comparable intensities in the 30-45 W range. The reactivity of the *t*PPA$^{\bullet+}$/mesitylene system can be evaluated by observing the increase in anodic peak current before ($i_{p,0}$) and after (i_p) addition of the substrate, as seen for example in Figure 26 under irradiation with 427 nm blue light. The recorded values of $i_p/i_{p,0}$, proportional to the photoreactivity, are plotted in Figure 41 (a).

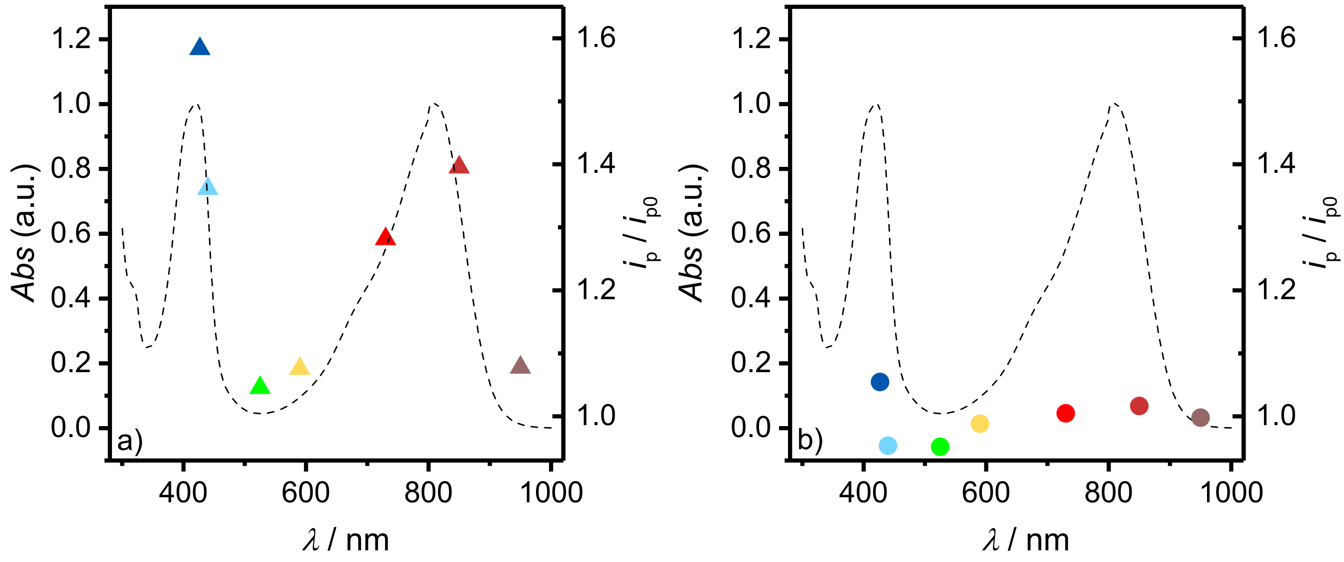

Figure 41. UV-Vis spectra of 0.5 mM *t*PPA$^{\bullet+}$ in DCM + 0.1 M *n*-Et$_4$NBF$_4$, measured using a 0.1 cm quartz cuvette. (a) emission band of the lamp used to excite *t*PPA$^{\bullet+}$ to $^*t$PPA$^{\bullet+}$. (a) The triangles represent the i_p/i_{p0} where i_p is the catalytic current measured in presence of substrate, nucleophile and light, while i_{p0} is the current measured in presence only of the catalyst under light irradiation. (b) The circles represent the i_p/i_{p0} where i_p is the catalytic current measured in presence of the catalyst, nucleophile and light, while i_{p0} is the current measured in presence only of the catalyst under light irradiation.

The voltammetry results indicate that the wavelength-dependent photoreactivity of the catalyst closely aligns with its absorption spectrum. The current enhancement is negligible at wavelengths where the catalyst does not absorb light (525, 590, and 950 nm). However, minimal activity is observed at 525 nm (Figure 41 (a)), likely due to the broad emission spectrum of the lamp, which emits some photons with sufficient energy to excite the catalyst. Interestingly, excitation at wavelengths within the second absorption band (730 and 850 nm) also induces noticeable reactivity, which appears to be approximately similar to that observed irradiating in the blue (427 and 440 nm).

To investigate potential side reactions with the nucleophile alone, we conducted an experiment in which only the nucleophile and catalyst were present, without the substrate, across varied light sources. This allowed us to directly evaluate the catalyst-nucleophile reactivity. The current increase i_p/i_{p0} was much smaller in the presence of nucleophile alone, than in the presence of both nucleophile and substrate (Figure 41 (b)). This suggests that reactivity observed is primarily due to the reaction of $^*t$PPA$^{\bullet+}$ with the substrate, with minimal contribution from direct reaction between $^*t$PPA$^{\bullet+}$ and the nucleophile.

These data do not support anti-Kasha behavior, as the observed photoreactivity is very similar when irradiating both bands. This suggests traditional photoreactivity in accordance with Kasha's rule: once D$_2$ is formed via photoexcitation with blue light, the excited states quickly relax to D$_1$ via internal conversion. Subsequently, photoreactivity occurs from D_1. If the catalyst is directly excited to D_1 with red light, similar reactivity is observed.

It should be noted that both D_1 and D_2 have extremely short lifetimes of 7 ps and 1 ps, respectively. Mixed reactivity from both D_1 and D_2 excited states is also possible.

4. Conclusions and future perspectives

This thesis has explored the mechanisms underpinning electrochemically mediated photoredox catalysis (e-PRC), with a focus on triarylamines (*t*PAs) as potent electrophotocatalysts. A comprehensive characterization of the catalysts' electrochemical and photophysical properties was achieved by integrating experimental data with simulation approaches. The findings highlight the ability of *t*PAs to act as superoxidants under mild conditions (moderate oxidation potentials and visible light irradiation), showcasing their versatility in facilitating C−N bond formation and related oxidative transformations. Cyclic voltammetry and UV-Vis spectroscopy provided insights into the reactivity and stability of radical cation species, while EPR spectroscopy allowed a deeper understanding of molecular interactions and the elusive pre-complexes proposed in the literature.

The main findings can be summarized as follows:

I. The electrochemical properties of three selected catalysts were elucidated, including the diffusion coefficient, oxidation potential, and heterogeneous electron transfer constant, in the absence of light. In the dark, the reduction potential increased in the order, *t*PPA < *t*CPPA < *t*BPA, making the latter the strongest electro-oxidant in the dark. Under illumination the same trend was observed, although strongly enhanced by the formation of the respective excited states, which reached standard reduction potentials exceeding 4 V vs SCE.

II. Oxidation and excitation were combined in cyclic voltammetry (CV) to evaluate the effect of light on the system. This approach enabled the assessment of how light influences the electrochemical processes, affecting mass transfer and slightly increasing the diffusion coefficients.

III. The back electron transfer (BET) issue, i.e. the reaction between EPC and $\mathrm{Sub}^{\bullet+}$, was identified and addressed by introducing a nucleophile, which helped make the whole catalytic cycle irreversible and thus amenable to CV investigation under light irradiation.

IV. After confirming the absence of reactivity in the dark, the study progressed by testing the reactivity of the catalysts in the presence of various substrates in CV. Current enhancement was observed with the *t*PPA system with several benzene derivatives in the order mesitylene > *p*-xylene > toluene > benzene. Direct observation of the reaction between *t*CPPA system and halobenzenes was prevented by direct oxidation of the nucleophile, while *t*BPA, being a stronger oxidant, successfully enabled the reaction.

V. The hypothesis of a precomplex, which was proposed to justify the observed reactivity despite the short lifetime of the catalyst, was investigated experimentally. UV-Vis, EPR, and CV techniques were employed to search for evidence of this precomplex. However, despite extensive experimental efforts, no conclusive evidence for its existence was found.

VI. Simulation software was utilized to quantify key rate constants associated with the reaction mechanisms, employing a bimolecular mechanism to further analyze the system (i.e. bimolecular reaction between $^*\mathrm{EPC}^{\bullet+}$ and the substrate. The optimal correspondence between the experimental and simulated data confirms the validity of this approach, supporting a bimolecular reactivity.

VII. As the final step, the effect of wavelength on the reactivity of the system was tested. The results suggest that both the D_1 excited state (formed by absorbing in the Vis-NIR) and the D_2 excited state (formed by absorbing in the UV) of $t\mathrm{PPA}^{\bullet+}$ are active for photooxidations. This final finding can have profound implications and may also prompt a reconsideration of some of the physical-chemicals parameters determined in this work (i.e. E^* and k_{SET} for the catalysts).

Future perspectives

The inherent versatility of triarylamines (*t*PAs) allows for tuning their properties based on specific needs, providing a flexible and adaptable system. Additionally, exploring different nucleophiles, critical to the reaction system, could offer valuable insights and new strategies for enhancing catalytic performance, further advancing the potential applications of these systems.

Preliminary findings on the impact of different wavelengths highlight the promising photoreactivity of *t*PAs, particularly within their low-energy absorption band, unlocking potential for efficient organic synthesis under near-infrared (NIR) irradiation. This approach could enable the selective oxidation of challenging substrates like toluene and xylene under mild conditions with infrared light. Such a strategy promotes photocatalysis under exceptionally mild conditions, functional group tolerance, and potential applications to biologically relevant systems.

5. Appendix and Control experiments

Determination of the working electrode active surface area

Prior to beginning characterization, the active area of the glassy carbon (GC) electrode used as the working electrode in CV experiments under irradiation was determined via cyclic voltammetry (CV). The ferrocene/ferrocenium redox couple (Fc/Fc$^+$) exhibits a reversible single electron transfer (Equation (34)) in a solution of DCM with 0.1 M *n*-Et$_4$NPF$_6$, with a previously reported diffusion coefficient of $(1.67 \cdot 10^{-5}\ cm^2 s^{-1})$ at $25\ °C^{59}$.

$$Fc^+ + e^- \rightarrow Fc \tag{34}$$

$$A = \frac{\partial i_{pa}/\partial v^{1/2}}{0.4463 nFcD^{1/2}} \cdot \left(\frac{RT}{nF}\right)^{1/2} \tag{35}$$

Using the Randles-Ševčik equation (10), which relates the anodic current to the potential scan rate, the active surface area of the working electrode, A, can be determined by varying the scan rate while maintaining constant concentration and temperature. A is calculated from the linear regression ($\partial i_{pa}/\partial v^{1/2}$) of i_{pa} versus $v^{1/2}$, as shown in equation (35).

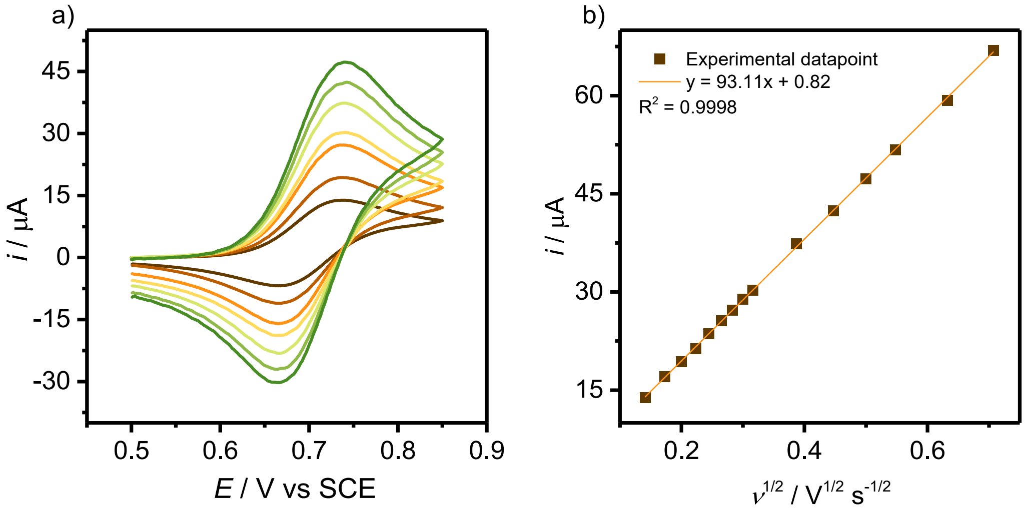

Figure 42. a) CV of 1 mM Ferrocene in DCM + 0.1 M *n*-Et$_4$NBF$_4$ on a GC electrode (A = 7.46 ± 0.05 mm^2), temperature T = 25 °C. Scan rate from 0.02 V s^{-1} to 0.250 V s^{-1}. b) linear fit of i_{pa} vs $v^{1/2}$.

CVs were recorded at different scan rates ranging from 0.02 V s^{-1} to 1 V s^{-1} (Not all were reported for clarity, Figure 42). The active area of the GC RDE tip was determined to be $A = 7.46 \pm 0.05\ mm^2$. This result is, as expected, slightly larger than the geometric surface area ($7.07\ mm^2$), and this is attributed to the surface roughness.

Calculus of the photon absorbed

The photoexcitation rate constant k_{EXC} was estimated based on the approach of Costentin et al.[18], involving the molar extinction coefficient (ε) of EPC$^{\bullet+}$ and the lamp's irradiance (I). Since the irradiation source used here is not monochromatic, the value of εI was obtained by integrating the product of these terms across the relevant wavelengths, effectively capturing the overlap area between the two variables, as graphically shown in Figure 43.

$$k_{EXC} = \int \varepsilon(\lambda)I(\lambda)d\lambda \tag{36}$$

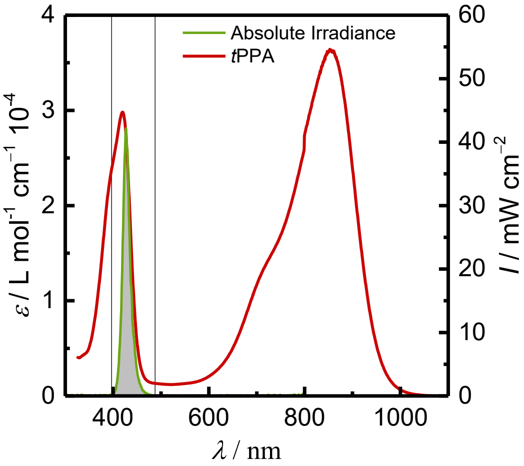

Figure 43. Overlay between the absorption spectra of *t*PPA and the emission spectra of the Kessil 427 nm lamp. The grey area represents the overlap between the two curves. The absorption spectra was recorded in DCM + 0.1 M *n*-Et_4NBF_4.

For the catalyst *t*PPA and the lamp with the maximum wavelength at 247 nm, k_{EXC} is calculated to be 81 s^{-1}.

Marcus theory calculations

Table 7. Example of calculation of k_{BET} for the *t*PPA and mesitylene$^{\bullet+}$ couple.

Parameter	Value
Substrate radius (r_{A})	$2.2 \cdot 10^{-10}$ m
Catalyst radius (r_{D})	$5.7 \cdot 10^{-10}$ m
Static dielectric constant (D_{s})	8.9
Optical dielectric constant (D_{op})	2
Reorganization energy (λ_{Out})	102449 J mol^{-1}
Frequency of collision (Z)	$2.99 \cdot 10^{-11}$ s^{-1}
Excited state potential (E^{*})	3.89 V vs SCE
Substrate potential (E)	2.07 V vs SCE
Activation free energy ($\Delta G^{\ddagger}$)	344 J mol^{-1}
Rate constant (k)	$1.5 \cdot 10^{9}$ s^{-1} M^{-1}

Radius of molecules were calculated using Equation (37), Reorganization energy using Equation (38), optical[60] and static[61] dielectric constant from literature, frequency of collision using Equation (39), activation free energy $\Delta G^{\ddagger}$ using Equation (40), oxidation potential of substrates from literature[62,63] and electron transfer rate constant using Equation (41) and.

$$D = \frac{k_{\mathrm{B}}T}{6\pi\eta r} \tag{37}$$

$$\lambda_{\mathrm{out}} = \frac{(\Delta \mathrm{e})^2}{4\pi\varepsilon_0}\left[\frac{1}{2r_{\mathrm{D}}} + \frac{1}{2r_{\mathrm{A}}} - \frac{1}{r_{\mathrm{DA}}}\right]\left[\frac{1}{\varepsilon_{\mathrm{op}}} - \frac{1}{\varepsilon_{\mathrm{s}}}\right] \tag{38}$$

$$Z = d_{AB}^2\sqrt{\frac{8k_BT}{\mu}} \tag{39}$$

$$\Delta G^{\ddagger} = \frac{(\lambda_0 + \Delta G^0)^2}{4\lambda_0} \tag{40}$$

$$k = Ze^{-\frac{\Delta G^{\ddagger}}{RT}} \tag{41}$$

3.7.1 Control experiments

Reactivity between the catalyst and the nucleophile

The addition of the nucleophile to the reaction system, introduced to suppress the back electron transfer effect, added a layer of complexity. This modification required an evaluation of the reactivity between the catalyst and the nucleophile, as the initial system only involved the desired reaction between the catalyst and the substrate. The introduction of the nucleophile created the possibility of an additional competing reaction between the catalyst and the nucleophile, necessitating its thorough assessment.

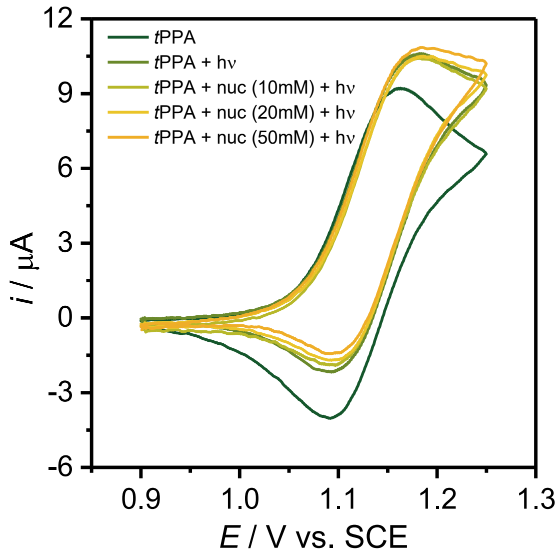

Figure 44. CV of 1mM *t*PPA in DCM + 0.1 M *n*-Et_4NBF_4 with 10, 20 and 50 mM triazole as nucleophile. Light 427 nm, scan rate 20 mVs^{-1}, $T = 20$ °C.

To investigate this, a series of experiments were conducted to evaluate the reactivity under various conditions. Specifically, all three catalysts were tested in the presence of the nucleophile both with and without light irradiation. The results, illustrated in the figures, show that in the absence of light, there is no observable reactivity between the catalyst and the nucleophile. However, under light irradiation, the photoexcited catalyst can oxidize the nucleophile, leading to a measurable but relatively minor reactivity. This is especially visible in the decrease reversibility of the CV with increasing nucleophile concentrations.

Although this reactivity is significantly lower than that observed between the catalyst and the substrate, it is accounted for in all simulations and considered in the overall analysis of system trends.

Determination of k_{sr}

The rate constant for the side reaction (k_{sr}) between the excited-state catalyst $^{*}t\mathrm{PPA}^{\bullet+}$ and the nucleophile triazole (Equation (31)) was determined using simulation software. An experiment was conducted with only the catalyst and nucleophile present, ensuring that any increase in current could be attributed solely to the interaction between these two species. The experimental data were then fitted using the simulation software, yielding the rate constant for this reaction.

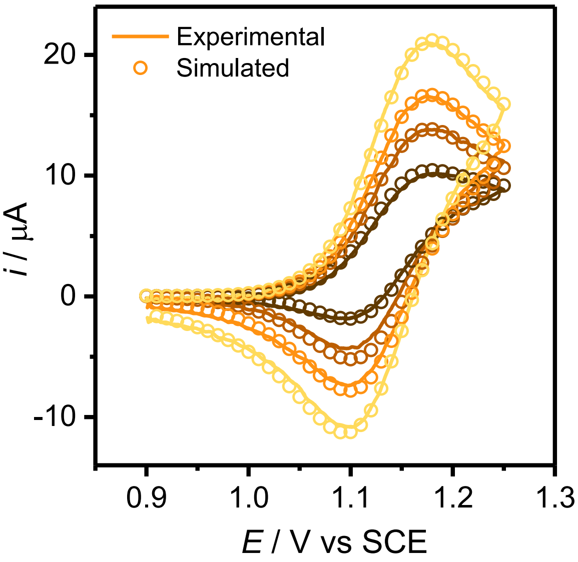

Figure 45. Experimental (line) and simulated (circles) for the CV of 1mM *t*PPA in DCM + 0.1 M *n*-Et_4NBF_4 with triazole as nucleophile. Light 427 nm, scan rate 20, 40, 60 and 100 mVs^{-1}, $T = 20$ °C.

The results, shown in Figure 45, demonstrate an excellent agreement between the experimental and simulated curves. This agreement supports the hypothesis of a bimolecular reaction mechanism between the excited-state catalyst and the nucleophile. The close match between the experimental and simulated data confirms the validity of the model and the calculated rate constant.

5.1 Spectra

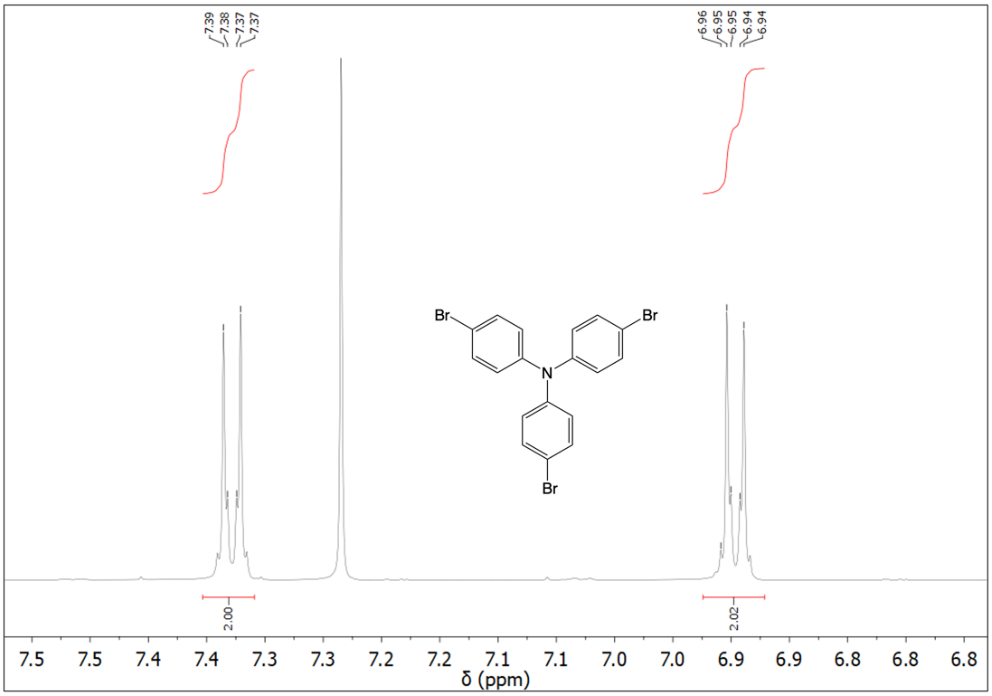

Figure 46. ^{1}H NMR (600 MHz, $CDCl_3$) of tris(*p*-bromophenyl)amine (*t*BPA).

^{1}H NMR (600 MHz, $CDCl_3$) δ 7.38 (d, J=8.83, 2 H, Ar-H), 6.94 (d, J = 8.83, 2 H, Ar-H)

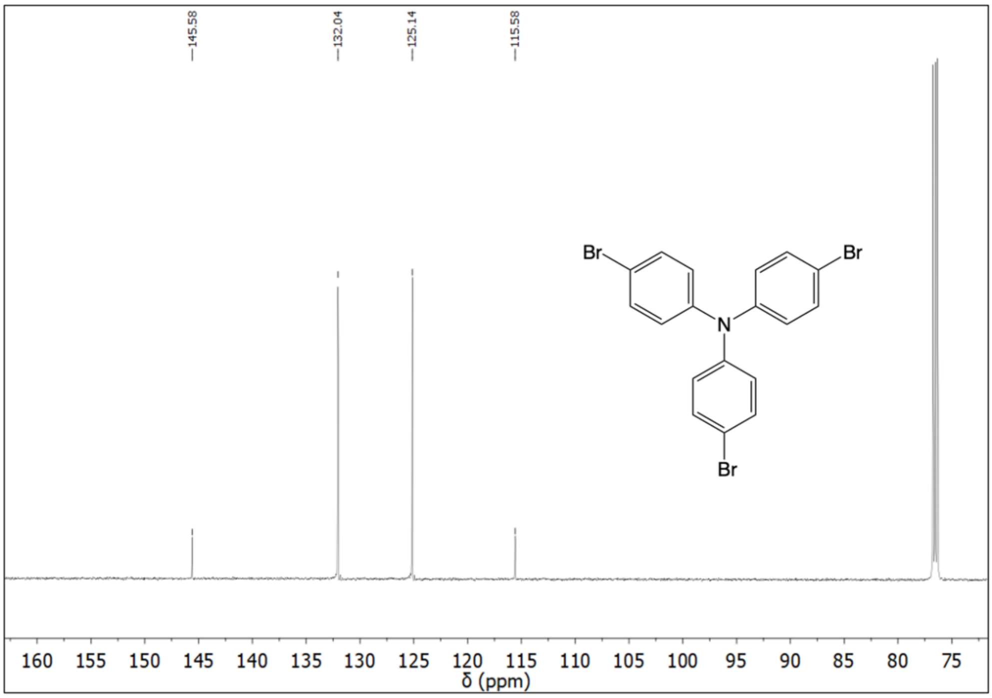

Figure 47. ^{13}C NMR (400 MHz, CDCL$_3$) of tris(*p*-bromophenyl)amine (*t*BPA).

^{13}C NMR (600 MHz, CDCl3) δ 145.6, 132.1, 125.2, 115.6

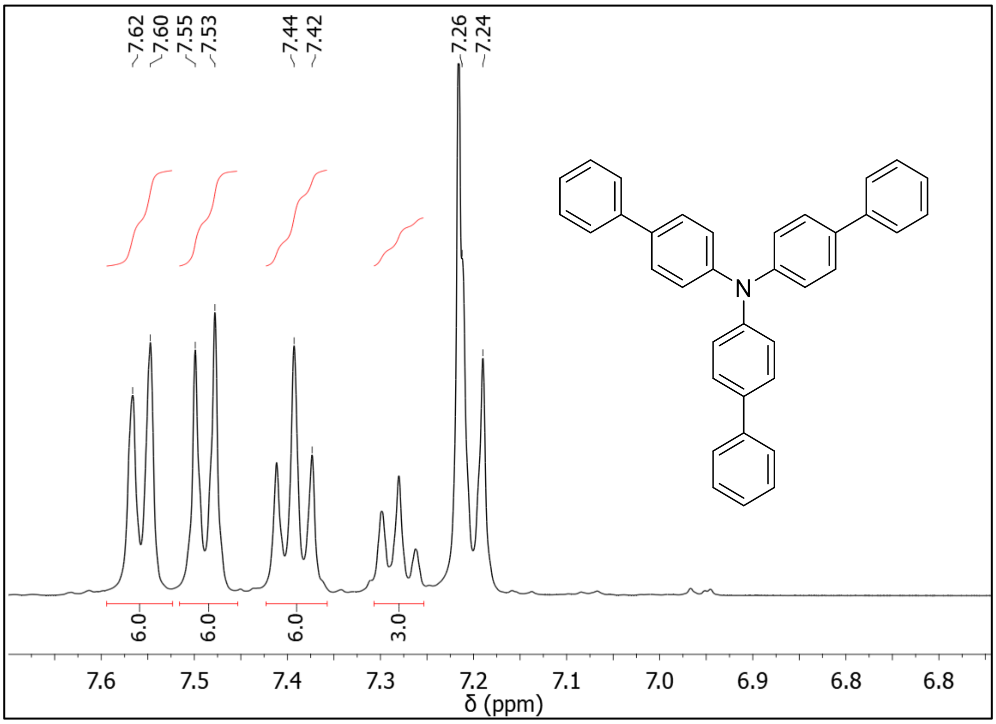

Figure 48. ^{1}H NMR (300 MHz, $CDCl_3$) of tri([1,1'-biphenyl]-4-yl)amine (*t*BPA).

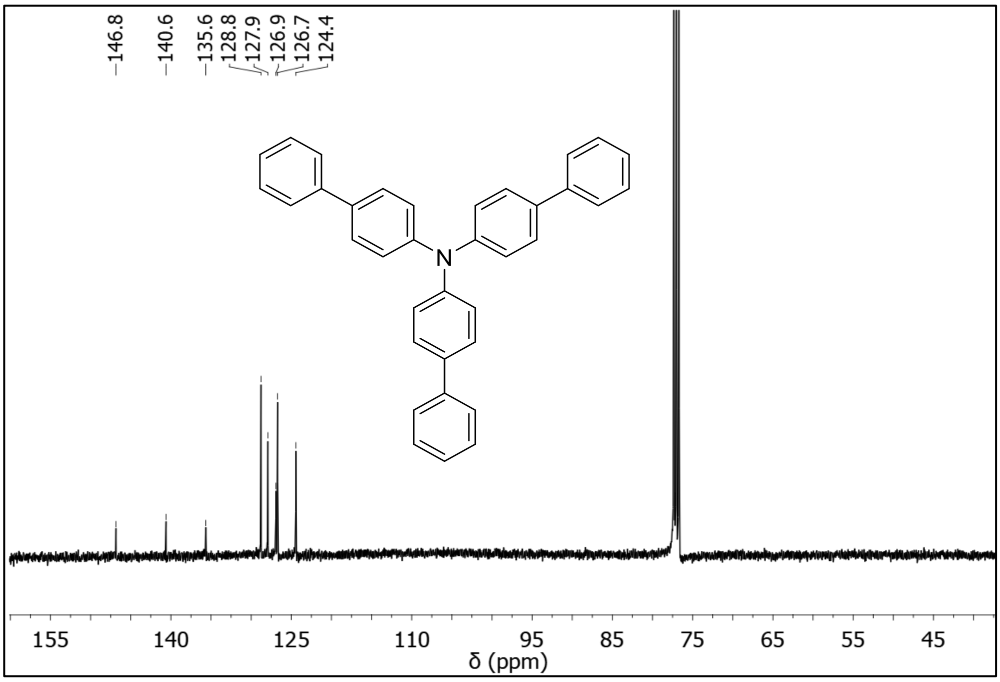

Figure 49. ^{13}C NMR (400 MHz, $CDCL_3$) of tri([1,1'-biphenyl]-4-yl)amine (*t*BPA).

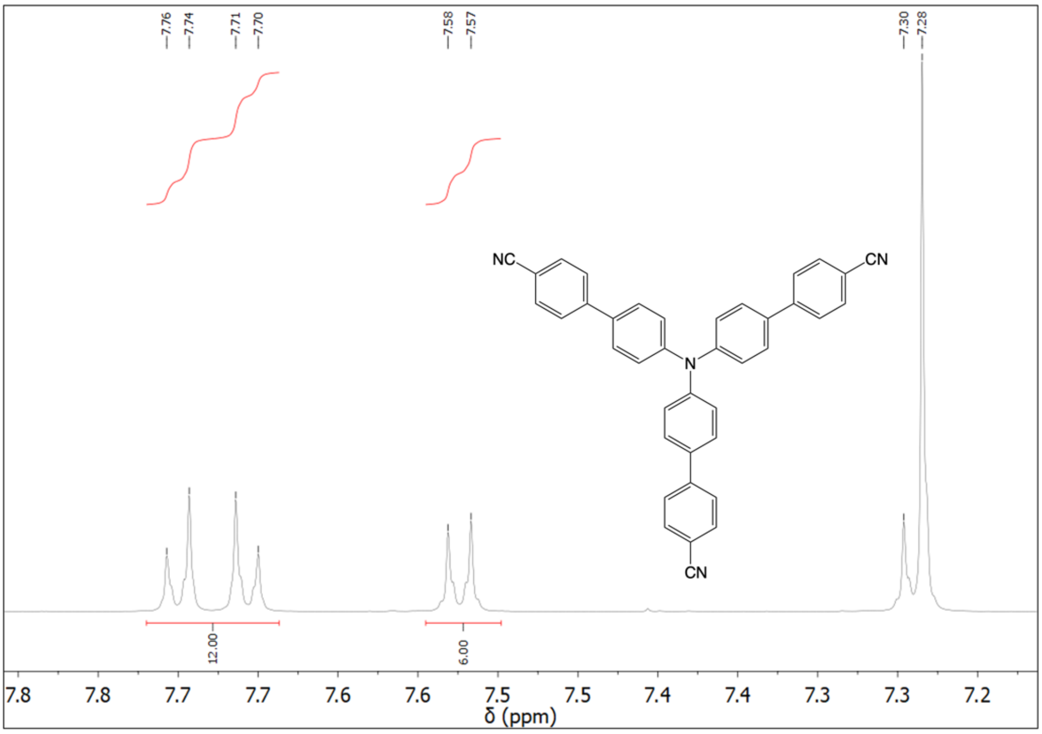

Figure 50. ^{1}H NMR (600 MHz, CDCl$_3$) of 4',4''',4'''''-nitrilotris(([1,1'-biphenyl]-4-carbonitrile)) (*t*CPPA).

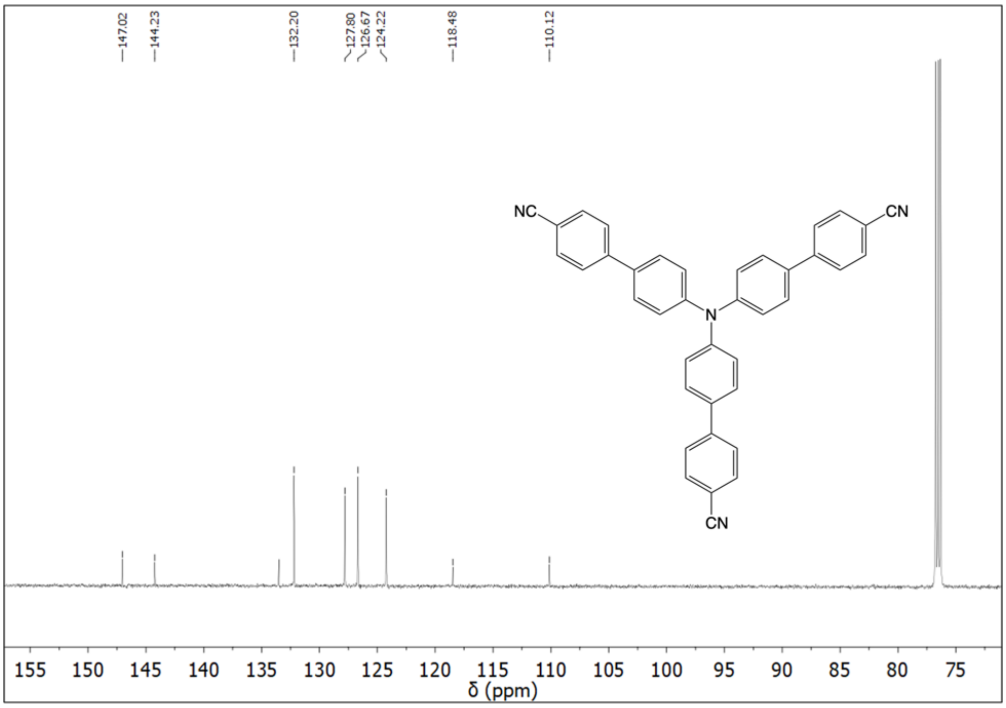

Figure 51. ^{13}C NMR (600 MHz, CDCL$_3$) of 4',4''',4'''''-nitrilotris(([1,1'-biphenyl]-4-carbonitrile)) (*t*CPPA).

Glossary of acronyms

BET	Back Electron Transfer
CE	Counter Electrode
CV	Cyclic Voltammetry
DET	Dissociative Electro Transfer
DMF	*N*,*N*-Dimethylformamide
EC	Electrocatalyst
E_{pa}	Anodic peak potential
E_{pc}	Cathodic peak potential
e-PRC	Electrochemically Activated Photoredox Catalysis
ET	Electron Transfer
GC	Glassy Carbon
IC	Internal Conversion
i_{pa}	Anodic peak current intensity
iPEC	Interface Photo-Electrochemistry
ISC	Intersystem Crossing
ISET	Inner Sphere Electron Transfer
NMR	Nuclear Magnetic Resonance
Nuc	Nucleophile
OSET	Outer Sphere Electron Transfer
PC	Photocatalyst
PET	Photoinduced Electron Transfer
PRC	Photoredox Catalysis
RDE	Rotating Disk Electrode
RE	Reference Electrode
SCE	Saturated calomel electrode
SET	Single Electron Transfer

Sub	Substrate
TBATFB	Tetrabuthyl ammonium tetrafluoroborate
TEATFB	Tetraethyl ammonium tetrafluoroborate
UV-Vis	Ultraviolet - Visible
WE	Working Electrode

6. Bibliography

(1) Leech, M. C.; Lam, K. Electrosynthesis Using Carboxylic Acid Derivatives: New Tricks for Old Reactions. *Acc. Chem. Res.* **2020**, *53* (1), 121–134. https://doi.org/10.1021/acs.accounts.9b00586.

(2) Tay, N. E. S.; Lehnherr, D.; Rovis, T. Photons or Electrons? A Critical Comparison of Electrochemistry and Photoredox Catalysis for Organic Synthesis. *Chem. Rev.* **2022**, *122* (2), 2487–2649. https://doi.org/10.1021/acs.chemrev.1c00384.

(3) Zhu, C.; Ang, N. W. J.; Meyer, T. H.; Qiu, Y.; Ackermann, L. Organic Electrochemistry: Molecular Syntheses with Potential. *ACS Cent. Sci.* **2021**, *7* (3), 415–431. https://doi.org/10.1021/acscentsci.0c01532.

(4) Wiebe, A.; Gieshoff, T.; Möhle, S.; Rodrigo, E.; Zirbes, M.; Waldvogel, S. R. Electrifying Organic Synthesis. *Angew. Chem. Int. Ed.* **2018**, *57* (20), 5594–5619. https://doi.org/10.1002/anie.201711060.

(5) Tay, N. E. S.; Lehnherr, D.; Rovis, T. Photons or Electrons? A Critical Comparison of Electrochemistry and Photoredox Catalysis for Organic Synthesis. *Chem. Rev.* **2022**, *122* (2), 2487–2649. https://doi.org/10.1021/acs.chemrev.1c00384.

(6) Wu, S.; Kaur, J.; Karl, T. A.; Tian, X.; Barham, J. P. Synthetic Molecular Photoelectrochemistry: New Frontiers in Synthetic Applications, Mechanistic Insights and Scalability. *Angew. Chem. Int. Ed.* **2022**, *61* (12), e202107811. https://doi.org/10.1002/anie.202107811.

(7) Barham, J. P.; König, B. Synthetic Photoelectrochemistry. *Angew. Chem. Int. Ed.* **2020**, *59* (29), 11732–11747. https://doi.org/10.1002/anie.201913767.

(8) Grimaud, L.; Lakhdar, S.; Vitale, M. R. Electrophotocatalysis: Taking the Best from the Two Worlds. *Curr. Opin. Electrochem.* **2023**, *40*, 101307. https://doi.org/10.1016/j.coelec.2023.101307.

(9) Qian, L.; Shi, M. Contemporary Photoelectrochemical Strategies and Reactions in Organic Synthesis. *Chem. Commun.* **2023**, *59* (24), 3487–3506. https://doi.org/10.1039/D3CC00437F.

(10) Hedstrand, D. M.; Kruizinga, W. H.; Kellogg, R. M. LIGHT INDUCED AND DYE ACCELERATED REDUCTIONS OF PHENACYL ONIUM SALTS BY 1,4-DIHYDROPYRIDINES.

(11) Ischay, M. A.; Anzovino, M. E.; Du, J.; Yoon, T. P. Efficient Visible Light Photocatalysis of [2+2] Enone Cycloadditions.

(12) Narayanam, J. M. R.; Tucker, J. W.; Stephenson, C. R. J. Electron-Transfer Photoredox Catalysis: Development of a Tin-Free Reductive Dehalogenation Reaction.

(13) Nicewicz, D. A.; MacMillan, D. W. C. Merging Photoredox Catalysis with Organocatalysis: The Direct Asymmetric Alkylation of Aldehydes. *Science* **2008**, *322* (5898), 77–80. https://doi.org/10.1126/science.1161976.

(14) Prier, C. K.; Rankic, D. A.; MacMillan, D. W. C. Visible Light Photoredox Catalysis with Transition Metal Complexes: Applications in Organic Synthesis. *Chem. Rev.* **2013**, *113* (7), 5322–5363. https://doi.org/10.1021/cr300503r.

(15) Shaw, M. H.; Twilton, J.; MacMillan, D. W. C. Photoredox Catalysis in Organic Chemistry. *J. Org. Chem.* **2016**, *81* (16), 6898–6926. https://doi.org/10.1021/acs.joc.6b01449.

(16) Kotani, H.; Ohkubo, K.; Fukuzumi, S. Photocatalytic Oxygenation of Anthracenes and Olefins with Dioxygen via Selective Radical Coupling Using 9-Mesityl-10-Methylacridinium Ion as an Effective Electron-Transfer Photocatalyst. *J. Am. Chem. Soc.* **2004**, *126* (49), 15999–16006. https://doi.org/10.1021/ja048353b.

(17) Romero, N. A.; Nicewicz, D. A. Organic Photoredox Catalysis. *Chem. Rev.* **2016**, *116* (17), 10075–10166. https://doi.org/10.1021/acs.chemrev.6b00057.

(18) Costentin, C.; Fortage, J.; Collomb, M.-N. Electrophotocatalysis: Cyclic Voltammetry as an Analytical Tool. *J. Phys. Chem. Lett.* **2020**, *11* (15), 6097–6104. https://doi.org/10.1021/acs.jpclett.0c01662.

(19) Wang, F.; Stahl, S. S. Merging Photochemistry with Electrochemistry: Functional-Group Tolerant Electrochemical Amination of C(Sp^3)−H Bonds. *Angew. Chem. Int. Ed.* **2019**, *58* (19), 6385–6390. https://doi.org/10.1002/anie.201813960.

(20) Fujishima, A.; Honda, K. Electrochemical Photolysis of Water at a Semiconductor Electrode. *Nature* **1972**, *238* (5358), 37–38. https://doi.org/10.1038/238037a0.

(21) Huang, H.; Steiniger, K. A.; Lambert, T. H. Electrophotocatalysis: Combining Light and Electricity to Catalyze Reactions. *J. Am. Chem. Soc.* **2022**, *144* (28), 12567–12583. https://doi.org/10.1021/jacs.2c01914.

(22) Shen, T.; Lambert, T. H. C–H Amination via Electrophotocatalytic Ritter-Type Reaction. *J. Am. Chem. Soc.* **2021**, *143* (23), 8597–8602. https://doi.org/10.1021/jacs.1c03718.

(23) Huang, H.; Strater, Z. M.; Lambert, T. H. Electrophotocatalytic C–H Functionalization of Ethers with High Regioselectivity. *J. Am. Chem. Soc.* **2020**, *142* (4), 1698–1703. https://doi.org/10.1021/jacs.9b11472.

(24) Shen, T.; Lambert, T. H. Electrophotocatalytic Diamination of Vicinal C–H Bonds. *Science* **2021**, *371* (6529), 620–626. https://doi.org/10.1126/science.abf2798.

(25) Moutet, J.-C.; Reverdy, G. Photochemistry of Cation Radicals in Solution : Photoinduced Electron-Transfer Reactions between Alcohols and the N,N,N',N'-Tetraphenyl -p-Phenylenediamine Cation Radical.

(26) Cowper, N. G. W.; Chernowsky, C. P.; Williams, O. P.; Wickens, Z. K. Potent Reductants via Electron-Primed Photoredox Catalysis: Unlocking Aryl Chlorides for Radical Coupling. *J. Am. Chem. Soc.* **2020**, *142* (5), 2093–2099. https://doi.org/10.1021/jacs.9b12328.

(27) Wu, S.; Žurauskas, J.; Domański, M.; Hitzfeld, P. S.; Butera, V.; Scott, D. J.; Rehbein, J.; Kumar, A.; Thyrhaug, E.; Hauer, J.; Barham, J. P. Hole-Mediated Photoredox Catalysis: Tris(*p* -Substituted)Biarylaminium Radical Cations as Tunable, Precomplexing and Potent Photooxidants. *Org. Chem. Front.* **2021**, *8* (6), 1132–1142. https://doi.org/10.1039/D0QO01609H.

(28) Shukla, S. S.; Rusling, J. F. Photoelectrocatalytic Reduction of 4-Chlorobiphenyl Using Anion Radicals and Visible Light. *J. Phys. Chem.* **1985**, *89* (15), 3353–3358. https://doi.org/10.1021/j100261a039.

(29) Zeman, C. J.; Kim, S.; Zhang, F.; Schanze, K. S. Direct Observation of the Reduction of Aryl Halides by a Photoexcited Perylene Diimide Radical Anion. *J. Am. Chem. Soc.* **2020**, *142* (5), 2204–2207. https://doi.org/10.1021/jacs.9b13027.

(30) Ghosh, I.; Ghosh, T.; Bardagi, J. I.; König, B. Reduction of Aryl Halides by Consecutive Visible Light-Induced Electron Transfer Processes. *Science* **2014**, *346* (6210), 725–728. https://doi.org/10.1126/science.1258232.

(31) Chen, Y.-J.; Deng, W.-H.; Guo, J.-D.; Ci, R.-N.; Zhou, C.; Chen, B.; Li, X.-B.; Guo, X.-N.; Liao, R.-Z.; Tung, C.-H.; Wu, L.-Z. Transition-Metal-Free, Site-Selective C–F Arylation of Polyfluoroarenes via Electrophotocatalysis. *J. Am. Chem. Soc.* **2022**, *144* (37), 17261–17268. https://doi.org/10.1021/jacs.2c08068.

(32) Kim, H.; Kim, H.; Lambert, T. H.; Lin, S. Reductive Electrophotocatalysis: Merging Electricity and Light To Achieve Extreme Reduction Potentials. *J. Am. Chem. Soc.* **2020**, *142* (5), 2087–2092. https://doi.org/10.1021/jacs.9b10678.

(33) Tian, X.; Karl, T. A.; Reiter, S.; Yakubov, S.; De Vivie-Riedle, R.; König, B.; Barham, J. P. Electro-mediated PhotoRedox Catalysis for Selective C(Sp^3)–O Cleavages of Phosphinated Alcohols to Carbanions. *Angew. Chem. Int. Ed.* **2021**, *60* (38), 20817–20825. https://doi.org/10.1002/anie.202105895.

(34) Caby, S.; Bouchet, L. M.; Argüello, J. E.; Rossi, R. A.; Bardagi, J. I. Excitation of Radical Anions of Naphthalene Diimides in Consecutive- and Electro-Photocatalysis**. *ChemCatChem* **2021**, *13* (13), 3001–3009. https://doi.org/10.1002/cctc.202100359.

(35) Walter, R. I. Triarylaminium Salt Free Radicals[1]. *J. Am. Chem. Soc.* **1955**, *77* (22), 5999–6002. https://doi.org/10.1021/ja01627a061.

(36) Tan, Z.; He, X.; Xu, K.; Zeng, C. Electrophotocatalytic C−H Functionalization of N-Heteroarenes with Unactivated Alkanes under External Oxidant-Free Conditions. *ChemSusChem* **2022**, *15* (6), e202102360. https://doi.org/10.1002/cssc.202102360.

(37) Ning, Z.; Tian, H. Triarylamine: A Promising Core Unit for Efficient Photovoltaic Materials. *Chem. Commun.* **2009**, No. 37, 5483. https://doi.org/10.1039/b908802d.

(38) Bonesi, S. M.; Protti, S.; Albini, A. Photochemical Co-Oxidation of Sulfides and Phosphines with Tris(*p* -Bromophenyl)Amine. A Mechanistic Study. *J. Org. Chem.* **2018**, *83* (15), 8104–8113. https://doi.org/10.1021/acs.joc.8b00913.

(39) Vasiļevska, A.; Slanina, T. Structure–Property–Function Relationships of Stabilized and Persistent *C* - and *N* -Based Triaryl Radicals. *Chem. Commun.* **2024**, *60* (3), 252–264. https://doi.org/10.1039/D3CC05706B.

(40) Jeong, D. Y.; Lee, D. S.; Lee, H. L.; Nah, S.; Lee, J. Y.; Cho, E. J.; You, Y. Evidence and Governing Factors of the Radical-Ion Photoredox Catalysis. *ACS Catal.* **2022**, *12* (10), 6047–6059. https://doi.org/10.1021/acscatal.2c00763.

(41) Sen, P. P.; Saha, N.; Raha Roy, S. Investigating the Potency of a Phenalenyl-Based Photocatalyst under the Photoelectrochemical Condition for Intramolecular C–S Bond Formation. *ACS Catal.* **2024**, *14* (2), 907–920. https://doi.org/10.1021/acscatal.3c05500.

(42) Mandigma, M. J. P.; Kaur, J.; Barham, J. P. Organophotocatalytic Mechanisms: Simplicity or Naïvety? Diverting Reactive Pathways by Modifications of Catalyst Structure, Redox States and Substrate Preassemblies. *ChemCatChem* **2023**, *15* (11), e202201542. https://doi.org/10.1002/cctc.202201542.

(43) Piechota, E. J.; Meyer, G. J. Introduction to Electron Transfer: Theoretical Foundations and Pedagogical Examples. *J. Chem. Educ.* **2019**, *96* (11), 2450–2466. https://doi.org/10.1021/acs.jchemed.9b00489.

(44) Atkins - Physical Chemistry 8e.

(45) Hsu, C.-P. Reorganization Energies and Spectral Densities for Electron Transfer Problems in Charge Transport Materials. *Phys. Chem. Chem. Phys.* **2020**, *22* (38), 21630–21641. https://doi.org/10.1039/D0CP02994G.

(46) Bao, D.; Millare, B.; Xia, W.; Steyer, B. G.; Gerasimenko, A. A.; Ferreira, A.; Contreras, A.; Vullev, V. I. Electrochemical Oxidation of Ferrocene: A Strong Dependence on the Concentration of the Supporting Electrolyte for Nonpolar Solvents. *J. Phys. Chem. A* **2009**, *113* (7), 1259–1267. https://doi.org/10.1021/jp809105f.

(47) Kissinger, P. T.; Heineman, W. R. Cyclic Voltammetry.

(48) Bard, A. J.; Faulkner, L. R. *Electrochemical Methods: Fundamentals and Applications*, 2. edition.; Wiley: New York Weinheim, 2001.

(49) Nicholson, R. S. Theory and Application of Cyclic Voltammetry for Measurement of Electrode Reaction Kinetics. *Anal. Chem.* **1965**, *37* (11), 1351–1355. https://doi.org/10.1021/ac60230a016.

(50) Buzzetti, L.; Crisenza, G. E. M.; Melchiorre, P. Mechanistic Studies in Photocatalysis. *Angew. Chem. Int. Ed.* **2019**, *58* (12), 3730–3747. https://doi.org/10.1002/anie.201809984.

(51) Kim, D.; Teets, T. S. Strategies for Accessing Photosensitizers with Extreme Redox Potentials. *Chem. Phys. Rev.* **2022**, *3* (2), 021302. https://doi.org/10.1063/5.0084554.

(52) Gumy, J.-C.; Vauthey, E. Investigation of the Excited-State Dynamics of Radical Ions in the Condensed Phase Using the Picosecond Transient Grating Technique. *J. Phys. Chem. A* **1997**, *101* (46), 8575–8580. https://doi.org/10.1021/jp972066v.

(53) Gosztola, D.; Niemczyk, M. P.; Svec, W.; Lukas, A. S.; Wasielewski, M. R. Excited Doublet States of Electrochemically Generated Aromatic Imide and Diimide Radical Anions. *J. Phys. Chem. A* **2000**, *104* (28), 6545–6551. https://doi.org/10.1021/jp000706f.

(54) Fujitsuka, M.; Majima, T. Reaction Dynamics of Excited Radical Ions Revealed by Femtosecond Laser Flash Photolysis. *J. Photochem. Photobiol. C Photochem. Rev.* **2018**, *35*, 25–37. https://doi.org/10.1016/j.jphotochemrev.2017.12.003.

(55) Wylie, L.; Barham, J. P.; Kirchner, B. Solvent Dependency of Catalyst-Substrate Aggregation Through π - π Stacking in Photoredox Catalysis. *ChemPhysChem* **2023**, *24* (20), e202300470. https://doi.org/10.1002/cphc.202300470.

(56) Roessler, M. M.; Salvadori, E. Principles and Applications of EPR Spectroscopy in the Chemical Sciences. *Chem. Soc. Rev.* **2018**, *47* (8), 2534–2553. https://doi.org/10.1039/C6CS00565A.

(57) Seo, E. T.; Nelson, R. F.; Fritsch, J. M.; Marcoux, L. S.; Leedy, D. W.; Adams, R. N. Anodic Oxidation Pathways of Aromatic Amines. Electrochemical and Electron Paramagnetic Resonance Studies. *J. Am. Chem. Soc.* **1966**, *88* (15), 3498–3503. https://doi.org/10.1021/ja00967a006.

(58) Kumar, A.; Malevich, P.; Mewes, L.; Wu, S.; Barham, J. P.; Hauer, J. Transient Absorption Spectroscopy Based on Uncompressed Hollow Core Fiber White Light Proves Pre-Association between a Radical Ion Photocatalyst and Substrate. *J. Chem. Phys.* **2023**, *158* (14), 144201. https://doi.org/10.1063/5.0142225.

(59) Acevedo, I. L.; Katz, M. Viscosities and Thermodynamics of Viscous Flow of Some Binary Mixtures at Different Temperatures. *J. Solut. Chem.* **1990**, *19* (10), 1041–1052. https://doi.org/10.1007/BF00650507.

(60) Nabi, A.; Md Zain, S. B.; Jesudason, C. G. Densities, Ultrasonic Speeds, Refractive Indices, and COSMO Analysis for Binary Mixtures of Dichloromethane with Acetone and Dimethylsulfoxide at T = (298.15, 303.15, and 308.15) K. *Chem. Eng. Commun.* **2018**, *205* (4), 479–491. https://doi.org/10.1080/00986445.2017.1403908.

(61) Liu, Z.; Timmermann, J.; Reuter, K.; Scheurer, C. Benchmarks and Dielectric Constants for Reparametrized OPLS and Polarizable Force Field Models of Chlorinated Hydrocarbons. *J. Phys. Chem. B* **2018**, *122* (2), 770–779. https://doi.org/10.1021/acs.jpcb.7b06709.

(62) Roth, H.; Romero, N.; Nicewicz, D. Experimental and Calculated Electrochemical Potentials of Common Organic Molecules for Applications to Single-Electron Redox Chemistry. *Synlett* **2015**, *27* (05), 714–723. https://doi.org/10.1055/s-0035-1561297.

(63) Merkel, P. B.; Luo, P.; Dinnocenzo, J. P.; Farid, S. Accurate Oxidation Potentials of Benzene and Biphenyl Derivatives via Electron-Transfer Equilibria and Transient Kinetics. *J. Org. Chem.* **2009**, *74* (15), 5163–5173. https://doi.org/10.1021/jo9011267.